universität wien

DISSERTATION

Ultracold Neutron Converters

angestrebter akademischer Grad

Doktorin der Naturwissenschaften (Dr. rer. nat.)

Verfasserin: Małgorzata Kasprzak
Matrikel-Nummer: 0448516
Dissertationsgebiet: Physik
Betreuer: Univ.-Prof. Dr. Eberhard Widmann

Wien, am 20. Oktober 2008

Abstract

The aim of the work described in this thesis was to investigate the properties of the ultracold neutron (UCN) converter materials deuterium D_2, oxygen O_2 and heavy methane CD_4 (with emphasis on D_2) in the temperature range between 8 K and room temperature. Those investigations are part of the research and development project made in connection with the new high intensity ultracold neutron source based on solid D_2 (sD_2) as UCN converter and being built at Paul Scherrer Institute (PSI), Villigen, Switzerland. The development of high intensity UCN sources is important for improving the accuracy of experiments investigating fundamental properties of the neutron, e.g. the search for the electric dipole moment. Presently there are several projects to build new UCN sources in order to provide the desired increase in intensity. The essential issue is the efficient use of the UCN converter. At the UCN source at PSI, due to the use of sD_2 as UCN converter, the UCN density will be increased by about two orders of magnitude compared to the strongest source currently available (at Institut Laue-Langevin (ILL)).

The UCN converter here is to be understood as a medium which reduces the velocity of cold neutrons (CN, velocity of about 600 m/s) to the velocity of UCN (velocity of about 6 m/s). Its performance depends on the interaction of CN and UCN with the converter material. We can distinguish three aspects: (i) the transmission of CN through the material, (ii) the efficiency of the conversion of CN to UCN (so-called UCN production) and (iii) the UCN transmission through the material. The first two issues are covered in this work, the last topic has been investigated, for sD_2, in our previous experiments [1].

The experimental research has been done at the FUNSPIN beamline of the Swiss Spallation Neutron Source (SINQ) at PSI. We have measured the production of UCN from a CN beam in D_2 [2], O_2 and CD_4 and the CN transmission through all three materials [3]. In order to understand the underlying processes of the UCN production in gaseous and solid D_2 the CN energy dependent UCN production was measured [4]. The polarization of UCN produced from polarized CN in sD_2 and various methods of crystal preparation have been tested. The obtained results have been interpreted in terms of the neutron scattering theory.

Contents

List of Figures

List of Tables

Chapter 1

Introduction

The main topic of this thesis concerns the theoretical and experimental aspects of UCN production made in connection with the high intensity UCN source being built at PSI. The PSI UCN source is a spallation neutron source and involves using sD_2 to slow neutrons into the energy range of about 100 neV. Before going into the specific details of the source performance, we give a short overview of the motivation for building such a source, namely the world of particle physics.

Physics describes reality in terms of quantum field theory which is based on the quantum mechanics that was invented in 1925-26; detailed information about quantum field theory can be found in references [5, 6]. One of the most fascinating ideas of this theory is the equivalence of conservation laws and symmetry properties of the system. The mathematical formulation and justification of this property is made in the Noether's theorem [7]. Here, symmetry is understood to mean those transformations of the system that do not change the results of possible experiments. The transformations can be continuous, like spatial translation, or discrete, like the spatial inversion of coordinates (change of a right-handed coordinate system into a left-handed one or vice versa, the parity operation (P)). However, some quantities are not conserved under particular transformations, thus telling us that the symmetry is broken; for example in electromagnetic and strong interactions, P is conserved, in the weak interaction this symmetry is maximally violated [8, 9].

For many years particle physicists have been interested in testing conservation laws especially those that might show that quantum theory is not fundamental [6]. The underlying theory might not be a theory of fields or particles, but something quite different, e.g. strings. From this point of view, quantum field theory is an 'effective field theory', i.e. some low energy approximation to a more fundamental theory. One of the interesting phenomena being investigated is the search for the violation of time reversal invariance; this will be discussed in more details in the next section.

1.1 The CPT Theorem and Time Reversal Symmetry Violation

There are three discrete transformations of fundamental importance in the quantum field theory: the P operation mentioned in the previous section, the charge conjugation operation (C) and time reversal operation (T). The C operation changes a particle to its antiparticle and T inverts the time coordinate. The CPT theorem, which was formulated by J. Schwinger and B. Zumino and proved by G. Lüders [10] and W. Pauli [11], shows that all interactions are invariant under the combination of all three operations. One consequence of the CPT theorem is that the masses and the lifetimes of particles and antiparticles are exactly equal.

In the Big Bang scenario, which is the broadly accepted theory for the origin and evolution of our Universe, matter and antimatter are made in equal quantities because the forces which are responsible for their production are symmetric with respect to matter and antimatter [12]. Creation and anihilation of particles and antiparticles in the hot primordial Universe are equally probable. However, below a temperature of T $\sim$ 1 GeV the creation of particle-antiparticle is energetically blocked while the anihilation goes on. If all forces were symmetric with respect to matter and antimatter, in the Universe we would now have very little matter and antimatter left along with the photons that were created during the anihilation process. These photons, a relic of the earliest phase of the Universe, were first detected in 1956 by Penzias and Wilson as the cosmic microwave background radiation[1] and their spectrum has a form of the blackbody radiation at a temperature of 2.7K [2].

The Standard Model expectation for the ratio of the matter (baryons) to photon densities is of the order [13]:

$$\eta_{matter} = n_B/n_\gamma \equiv \eta_{antimatter} \sim 10^{-18} \tag{1.1}$$

The observations [14], however, show that the value of the baryon to photon ratio is:

$$\eta = n_B/n_\gamma = 6.1 \times 10^{-10} \tag{1.2}$$

This results for η makes sense only if this parameter is not a measure of n_B/n_γ, but rather is a measure of some primordial asymmetry [15]:

$$\eta \equiv \frac{n_{matter} - n_{antimatter}}{n_\gamma}|_{primordial} \tag{1.3}$$

The question is can one explain the origin of this primordial matter - antimatter asymmetry from the currently known laws of physics?

A possible explanation of this discrepancy was given in 1967 by Sakharov [16]; the baryon asymmetry can be the effect of:

- the non-conservation of the baryon number,

[1] Nobel Prize in Physics for 1978.
[2] Nobel Prize in Physics for 2006.

- C and CP violation,
- the lack of thermal equilibrium during the expansion of the universe.

CP violation was observed in 1964 in neutral K decays by Cronin and Fitch [17] and confirmed in 2001 in B mesons decays by the BELLE and BaBar collaborations [18, 19] however the size of CP violation is not sufficient to explain the matter - antimatter asymmetry.

CPT violation could also explain the matter-antimatter asymmetry (if, for example, the lifetimes of particle and its antiparticle were different); however all tests of particle-antiparticle symmetry properties indicate that all the interactions are invariant under this combination. Examples of direct, precision test of CPT invariance using antimatter include measurement of the electron/positron [20] and the proton/antiproton [21] mass ratios and g-factors. Also high-precision experiments with muons [22] represent a promising approach as well as the spectroscopic comparison of hydrogen and antihydrogen [23]; the CPT theorem requires that hydrogen and antihydrogen have the same spectrum. Perhaps, similar tests could be done with antiprotonic helium [24].

The CPT theorem implies violation of the time reversal invariance T if CP invariance doesn't hold. Nevertheless it is important to demonstrate T violation directly, without invoking the CPT theorem. Such a test has been done by the CPLEAR collaboration at CERN and the direct violation of T symmetry in the neutral kaon decays have been reported [25] (the validity of this results is being discussed [26, 27, 28]). There is still a need of more independent measurements investigating the nature of the T operation.

T operation differs from the other discrete transformations C and P, both from the conceptual and mathematical point of view. T operation implies 'running the movie backwards'; it inverts the direction of the flow of time ($t \rightarrow -t$) while keeping the spatial coordinate fixed i.e. all particles follow their trajectories in the opposite direction and the roles of the initial and final configurations are interchanged. To fulfill this condition, T transformation is represented by the antilinear antiunitary operator [5]. One of the ways to find out that T invariance is violated is the observation of the intrinsic electric dipole moment (EDM) of fundamental particles of spin $\frac{1}{2}$. EDM $\sim qr$ is an assymetry in the charge distribution, created by the separation of the charges q and $-q$ by a distance r and its orientation must be completely specified by the orientation of the particle spin. T operation acting on the particle with spin (which is an axial vector specifying a direction of rotation) and non-zero EDM, changes the spin direction but leaves EDM unchanged. Thus if T is a good symmetry, particles with spin and EDM would produce degenerate states with EDM aligned either parallel or anti-parallel to the spin i.e. we could tell the difference between a movie running forwards and backwards. In the following section a short explanation of the neutron EDM experimental technique is given.

1.2 EDM and Ultracold Neutrons

The electroweak Standard Model preditions [29] for the size of the neutron EDM are in the range $10^{-33} \leq \mathrm{d}_n \leq 10^{-31}$ e$\cdot$ cm [3] which is well below the present experimental sensitivity;

[3] where e = - 1.6×10^{-19} C

the current experimental limit is $d_n \leq 2.9 \times 10^{-26}$ e$\cdot$ cm (90% C.L.)[30]. The theoretical values given above are calculated assuming CP violation is only in the electroweak sector and due to a single complex phase δ in the CKM matrix. Taking into consideration the CP violating term θ_{QCD} in the QCD sector, the predicted 'electroweak' value of the neutron EDM can rise depending on the value of θ_{QCD}, according to $d_n \approx 10^{-16}\theta_{QCD}$ e$\cdot$cm [12]. Supersymmetric Models give rise to a weak CP violation of the θ_{QCD} type, d_n is of order $10^{-22}\phi$ e$\cdot$ cm with ϕ being the possible CP violating phase [31].

The experimental technique used to measure the EDM of a neutron is based on the detection of the Stark splitting induced by an electric field which is applied alternately parallel and anti-parallel to a small applied magnetic field. Any difference in the neutron's Larmor precession frequencies between measurements with the electric field parallel and anti-parallel to the magnetic field indicates the presence of an EDM: more detailed information about the experimental technique can be found, for example, in [32, 33]. The first neutron EDM experiment was carried out by Smith, Purcell and Ramsey [34, 35] with a beam of neutrons and gave $d_n = (-0.1 \pm 2.4) \times 10^{-20}$ e$\cdot$ cm. The main limitation in this experiment came from the motional magnetic field $\sim \mathbf{v} \times \mathbf{E}$ generated by the neutron moving through the field $\mathbf{E}$. This effect can be reduced by using neutrons which would have an average velocity $\mathbf{v}$ close to zero. Those neutrons with very low velocities are refered to as UCN. The measurement of the neutron EDM is the main experiment planned at the PSI UCN source. It has the goal to increase the sensitivity by about two orders of magnitude and be able to measure an EDM of: 10^{-28} e$\cdot$ cm $\leq d_n \leq 10^{-26}$ e$\cdot$ cm.

UCN, the neutrons with energies of about 100 neV, can be stored in UCN storage bottles with lifetimes comparable to the free neutron lifetime ($\tau_n = 885.7 \pm 0.8$ s [36]). The fact that one can store and observe UCN for such long periods makes them an excellent tool to study not only the electric dipole moment, but also other fundamental properties of the neutron e.g. the lifetime. Other fields where UCN can make useful new contributions are: the neutron mirror-neutron oscillations [37], surface physics [33] and the observation of quantum states in the Earth's gravitational field [38, 39]. The accuracy of such experiments with the present UCN sources is limited by statistics. Next generation experiments which aim to improve these sensitivities depend on the development of higher intensity UCN sources.

Chapter 2

PSI Ultracold Neutron Source and Solid Deuterium

Currently the only UCN source operated in regular user facility mode is located at Institut Laue-Langevi (ILL), Grenoble, France; UCN densities of about 50 UCN per cm^3 are available [40]. The experiments mentioned in the previous chapter would benefit greatly from an increase in UCN density. Presently there are several projects to build new UCN sources in order to realise this desired increase in intensity. At PSI we are setting up a high intensity UCN source with the aim to increase the available flux and densities by two orders of magnitude. Other efforts are under way at Los Alamos National Laboratory, ILL, RCNP Osaka, Technical University München, North Carolina State University and Mainz University. In fact the UCN source at the pulsed reactor TRIGA Mainz is already in operation [41].

One of the ways to increase the UCN intensity is to use an appropriate material as UCN converter, i.e. a medium that converts CN into UCN by inelastic scattering; the converter must have specific properties such as energy levels and excitations that enable the downscattering to take place. This mechanism differs from a typical scheme of neutron moderation used in the CN sources, i. e. the neutrons do not reach thermal equilibrium with the moderator material (more detailed discussion concerning moderators follows in the next chapter). This method of UCN production, superthermal UCN production, was first proposed by Golub and Pendlebury [42] and is used in the PSI UCN source as well as in the other new UCN sources.

2.1 Overview of the PSI UCN Source

In the PSI UCN source (see Figure 2.1) fast neutrons of average energy of about 2 MeV are produced by the spallation reaction of protons of energy 590 MeV hitting a lead target [43]. The proton beam with an intensity of about 2 mA is delivered from the ring cyclotron with a low duty cycle ($\sim$ 1 %), i.e. with 4 to 8 s beam on every 400 - 800 s. An overview of the PSI accelerator facilities is given in Figure 2.2. The full proton beam from the PSI ring cyclotron is sent into the UCN beam line by the kicker magnet placed in the extraction

channel of the ring [44]. The proton beam in the UCN beam line can be guided onto the spallation target or be directed to the beam dump by the second bending magnet (see Figure 2.3 and Figure 2.4). The protons generate neutrons on the target consisting of lead filled in zircaloy tubes. The spallation neutrons (about 10 n per p) are first moderated in a 3.3 m^3 tank of heavy water at room temperature and then further cooled and downscattered into the UCN energy range in 30 dm^3 of sD_2 at low temperature ($\sim$ 5K). This moderator assembly is shown in Figure 2.5. The neutrons exit sD_2 and gain energy because of the material optical potential (for sD_2 at 5K it is 105 neV) and then are further transported vertically 1.1 m upwards loosing energy due to gravity and reach the storage volume where the neutrons with energies below 250 neV can be trapped and guided to the experiments (see Figure 2.6). The sD_2 converter and the UCN storage tank are separated from each other using a valve (see Figure 2.7) to reduce neutron loss during storage. During the proton pulse, the valve to the storage volume is open and the UCN from the sD_2 converter fill the storage vessel. After the proton pulse is over, the shutter closes and UCN are transported to the experiments. The UCN operating scheme is shown in Figure 2.8. The storage volume has a size of about 80 x 80 x 240 cm^3 and serves as intermediate UCN storage between the proton beam pulses, thus allowing for quasi continuous availability of the UCN from the source. Storage of UCN relies on the possibility to totally reflect these neutrons under all angles of incidence from suitable materials. Over past few years we were investigating different materials in order to minimize the neutron losses in the UCN storage volume and thus improve the source performance. Our research lead to the choice of the most promising materials for the storage volume of the UCN source at PSI namely diamond-like carbon (DLC) coated materials.

2.2 Solid Deuterium Moderator

The sD_2 converter is the heart of the UCN source. The sD_2 will be kept in a vessel manufactured from AlMg4.5 (lower part) and AlMg3 (upper part) and will be cooled down to 6K using supercritical He. The scheme of the sD_2 container is shown in Figure 2.9. The vessel will be placed at the bottom of the vertical neutron guide, and for safety reasons, it needs to hold several atmospheres of overpressure and also be vacuum tight. Moreover the upper surface needs to be thin enough to allow the UCN to escape. Several tests have been done to optimize the shape and material of the upper part of the sD_2 vessel; the final shape is shown in Figure 2.10. The crystal of ortho-D_2 can be frozen either from the liquid or the gas phase in the vessel. During the proton pulse, a temperature increase to about 8-10K is expected. Our research showed that the UCN transmission through the carefully prepared D_2 crystals does not deteriorate[1] due to the thermal cycling between 5 and 10K.

This thesis is a part of the detailed R&D program that covers not only the engineering aspects of preparing and handling of sD_2, but also especially the relevant physics involved. One of the results of our research, the UCN production cross section [2], allows us to calculate the expected density of UCN in the source. With the 2 mA proton beam onto the Pb target, a cold neutron flux of about 2 x 10^{13} $cm^{-2}s^{-1}$ in the relevant region of sD_2 will produce 2.2 x 10^5 $cm^{-3}s^{-1}$ UCN according to the measured UCN production rate $R_{solid,8K}$

$= (1.11 \pm 0.23) \times 10^{-8}$ cm^{-1} (see chapter 6). The lifetime of the UCN in the sD_2 converter depends on the temperature[45]. During the proton beam pulse of 4s (8s), the temperature of the UCN producing region of sD_2 is calculated to rise from 6 to 8K (10K). Thus, conservatively assuming a 4 s long proton pulse and a constant lifetime of about 30 ms for UCN in sD_2 (at the end of the 4 s pulse) one calculates a density of about 6000 cm^{-3} in the sD_2 converter.

Proton pulses exceeding 8 s are not foreseen because of the heat load on the moderator; a practical limit on the proton pulse length of 8 s has been implemented by the layout of the power supply of the kicker magnet in the proton beam line [44]. The optimum (potentially shorter) pulse length will be determined experimentally by analyzing the source performance with the boundary condition of an overall 1% duty cycle (a limit imposed by radiation protection consideration). It is not expected that the sD_2 converter performance will deteriorate under irradiation besides the increase in thermal upscattering due to increased temperature. The ortho-D_2 concentration will be affected only slightly but will have a tendency to improved [46, 47, 48].

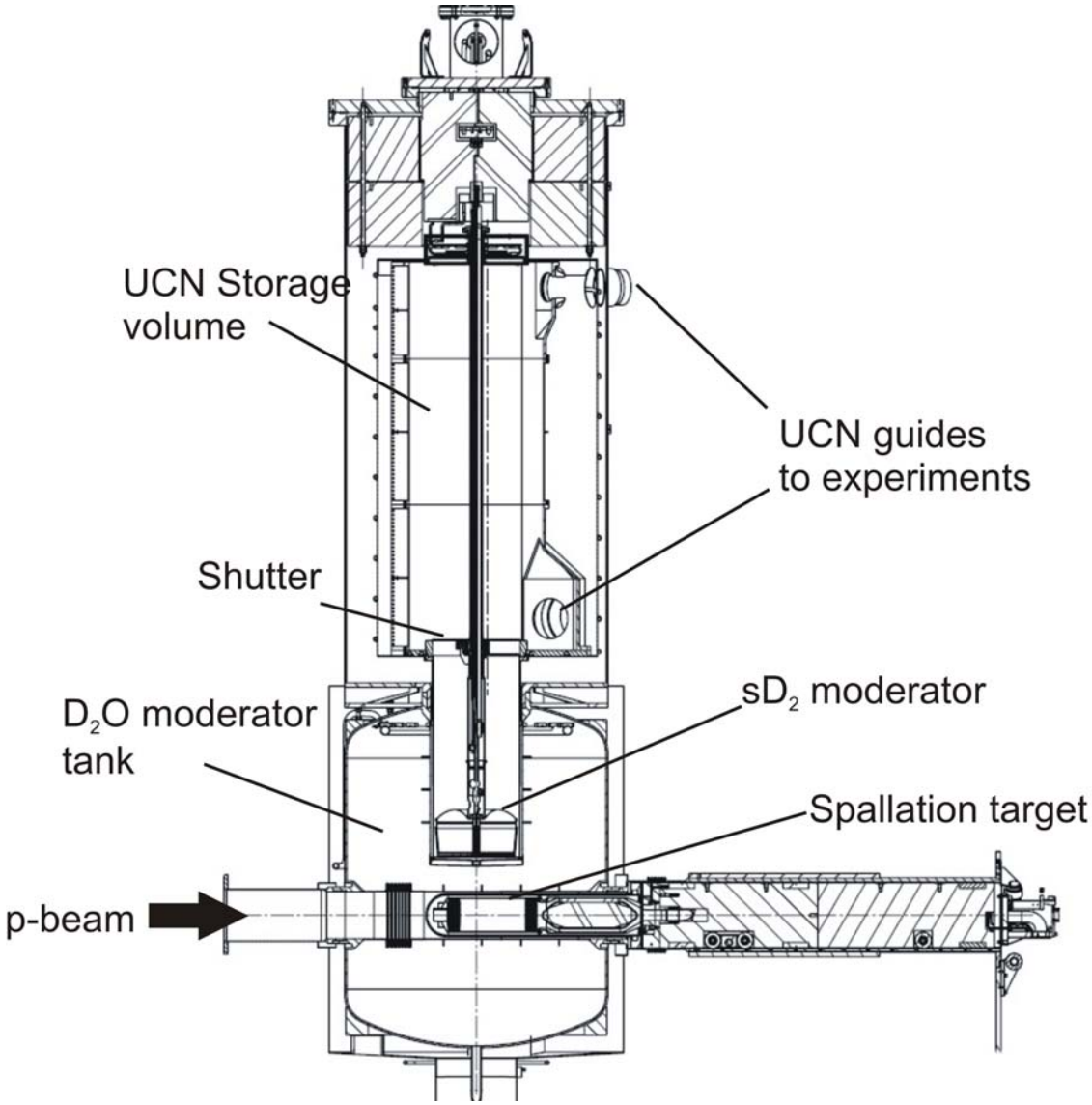

Figure 2.1: Layout of the UCN source at PSI. The proton beam hits the spallation target from the left. Spallation neutrons will be thermalized in the ambient temperature D_2O moderator, further cooled and downscattered into the UCN regime in the cold sD_2 moderator. Through a vertical neutron guide, the UCN reach the storage volume where they can be trapped and distributed to the experiments.

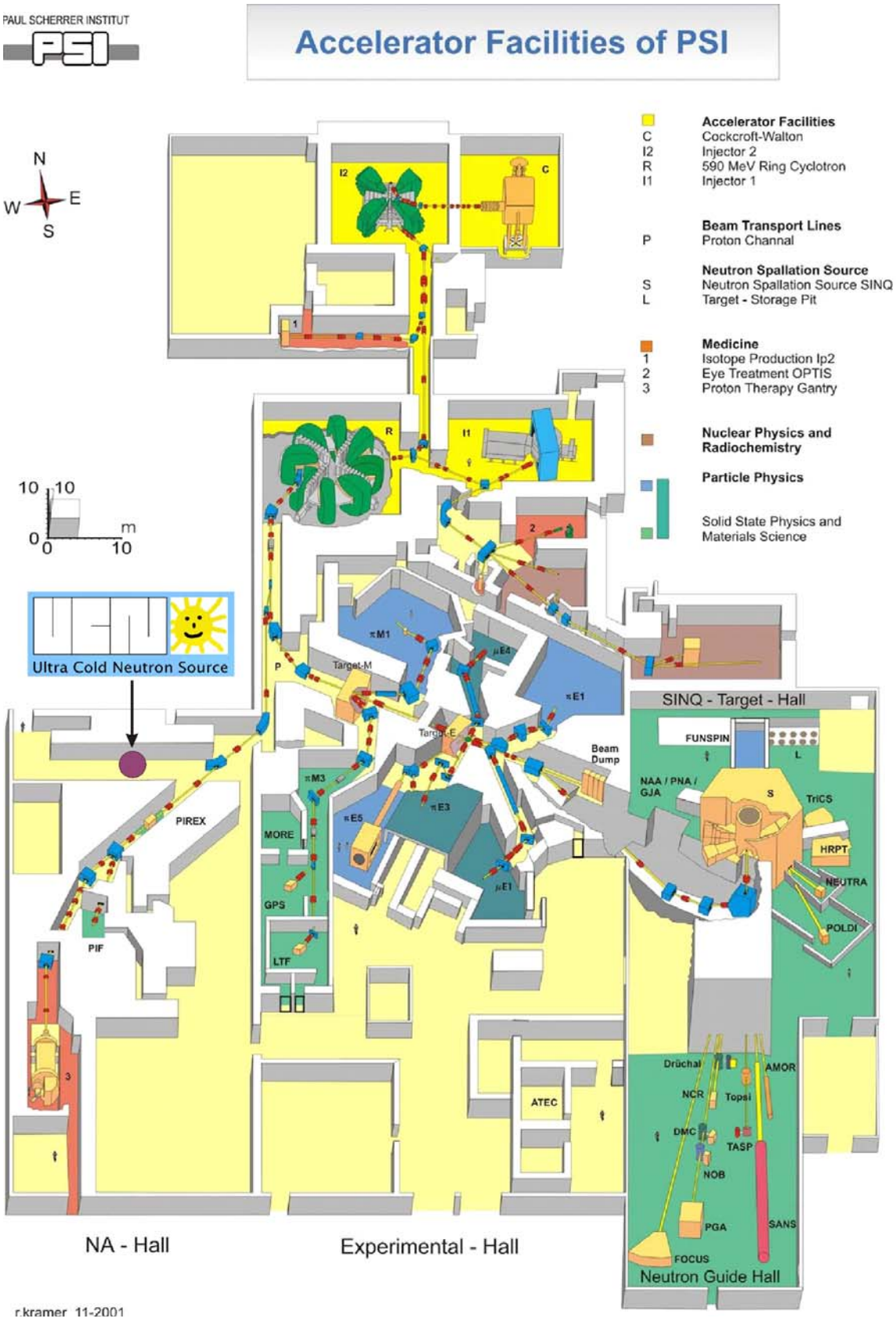

Figure 2.2: Layout of the PSI proton accelerator and the site of the UCN source.

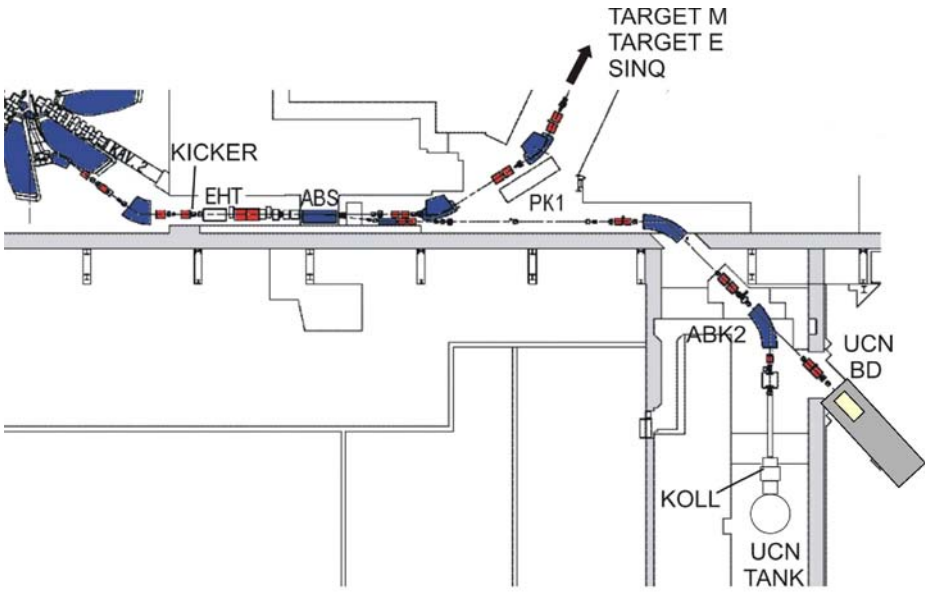

Figure 2.3: Scheme of the UCN proton beam line.

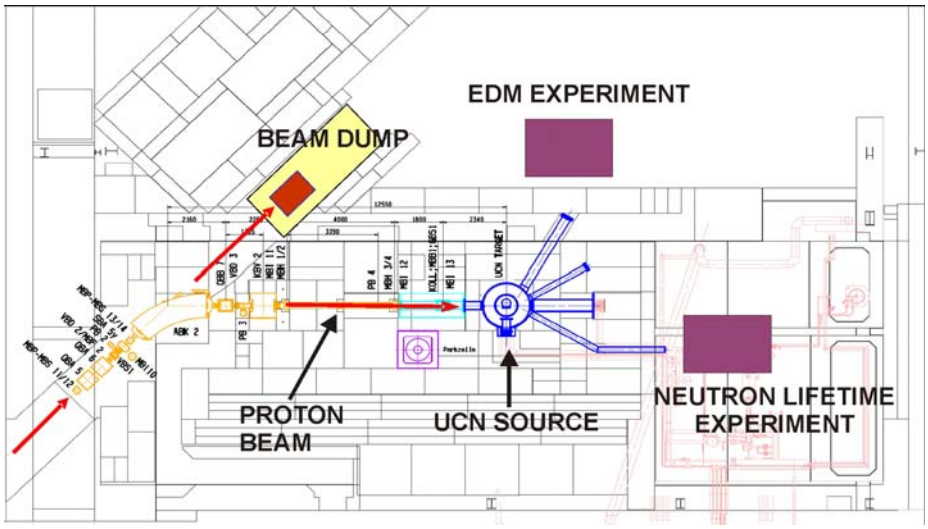

Figure 2.4: Layout of the proton line, UCN source and the UCN experiments.

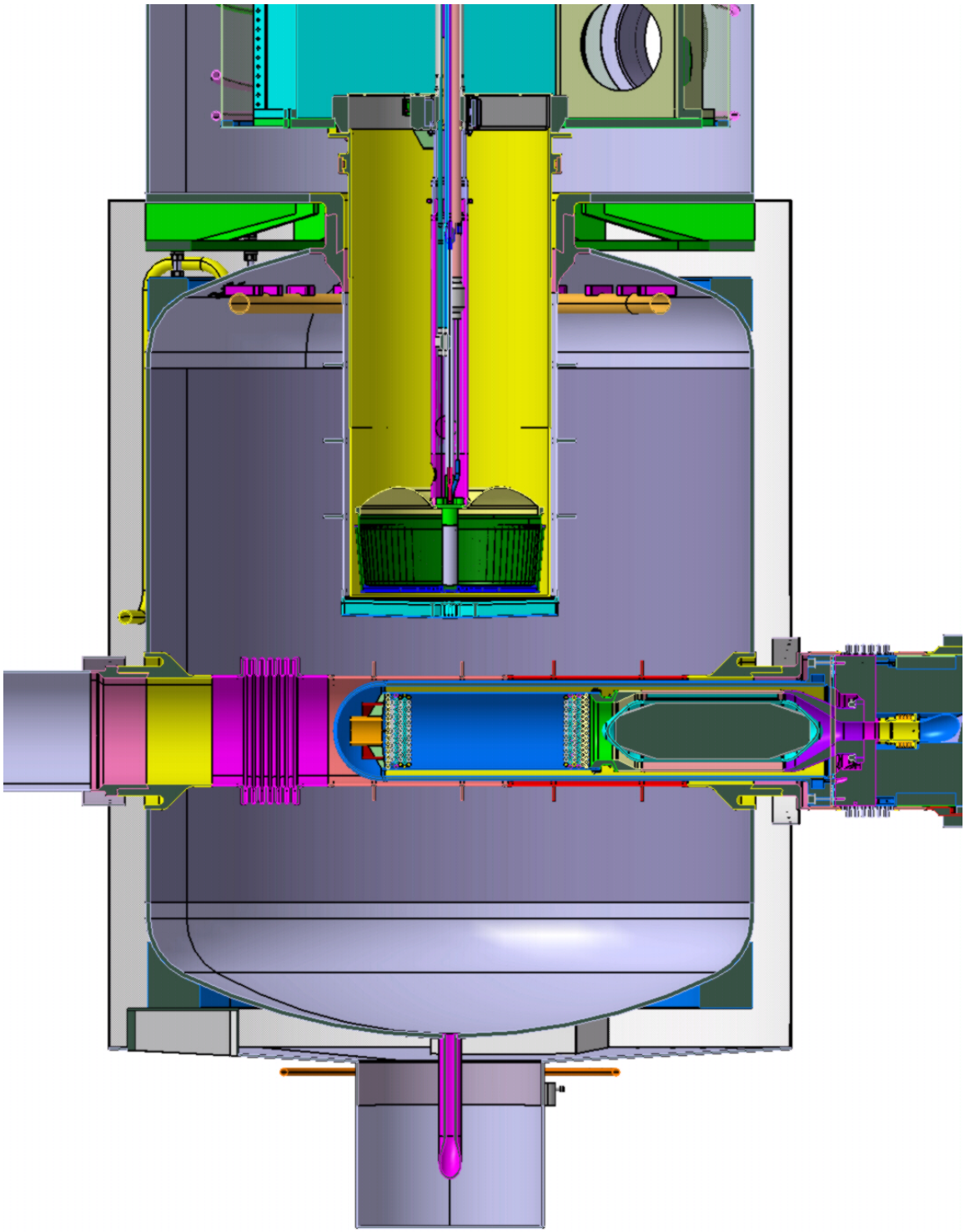

Figure 2.5: Drawing of the D_2O moderator tank (grey). One can see the proton beam pipe (horizontal pipe coloured in pink and blue) and the vertical neutron guide (yellow). The D_2O tank, made of aluminium alloy, has a diameter of 1.6 m and volume of about 3330 liters. Heavy water will be used to moderate the spallation neutrons and also to cool the spallation target. The sD_2 tank (coloured in green) is inserted into the system through the vertical guide.

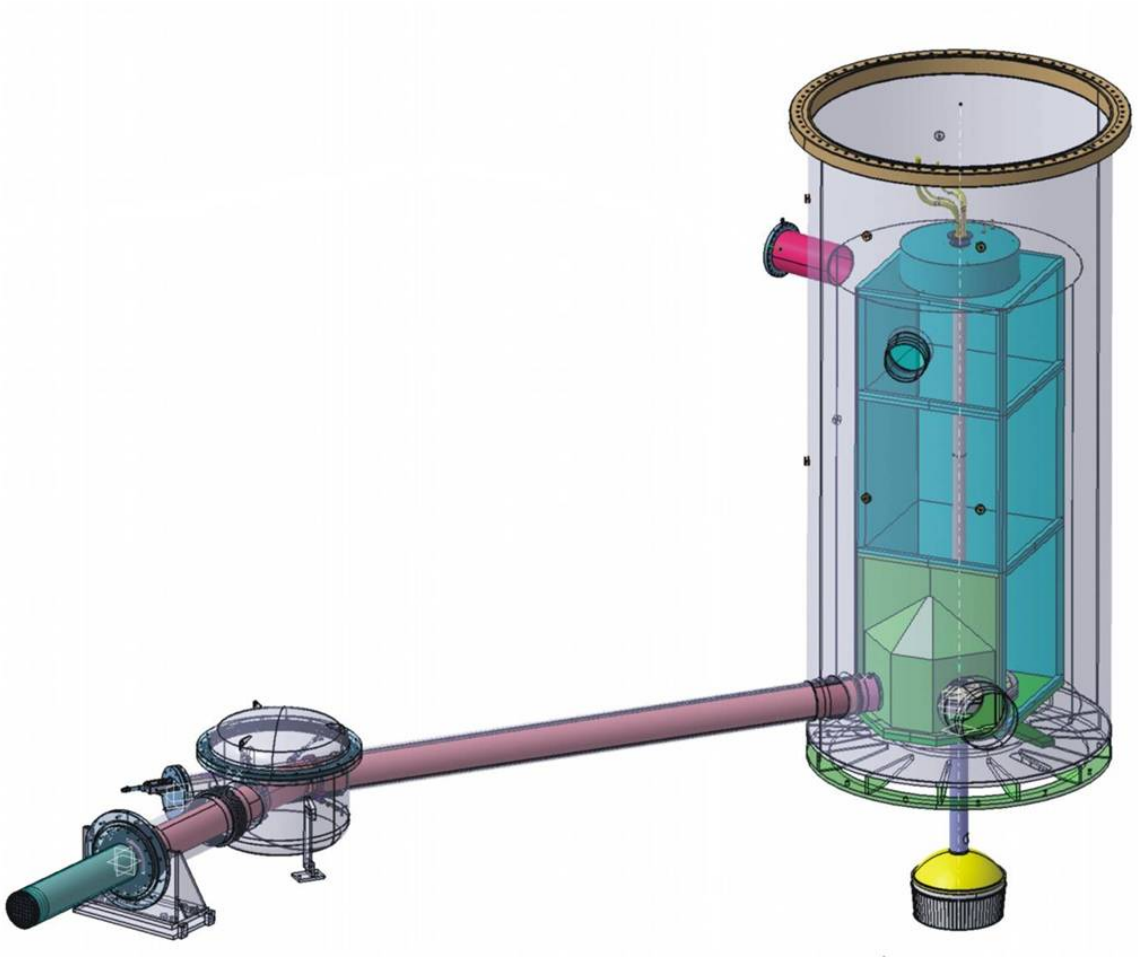

Figure 2.6: A model of the UCN storage tank together with one of the UCN guides, through which the UCN are transported to the experiment.

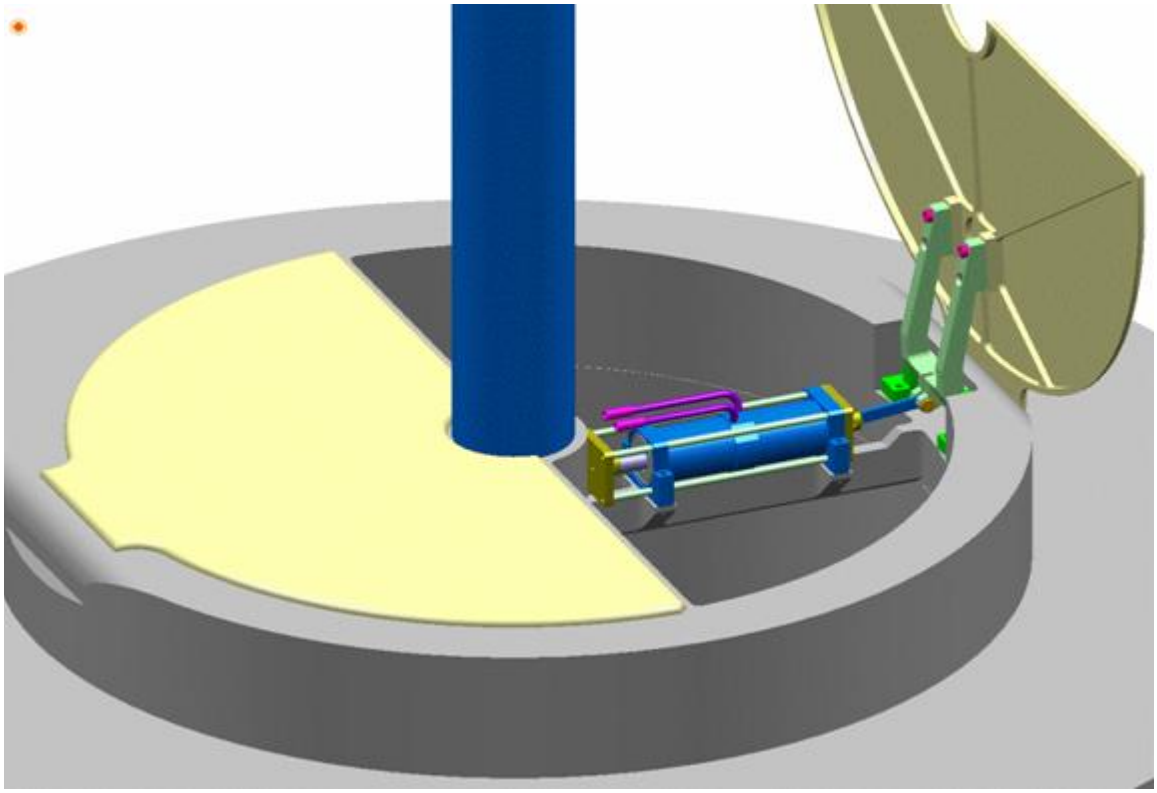

Figure 2.7: Drawing of the UCN shutter placed between the sD_2 converter and the UCN storage volume (at the end of the vertical neutron guide (see Figure 2.5)).

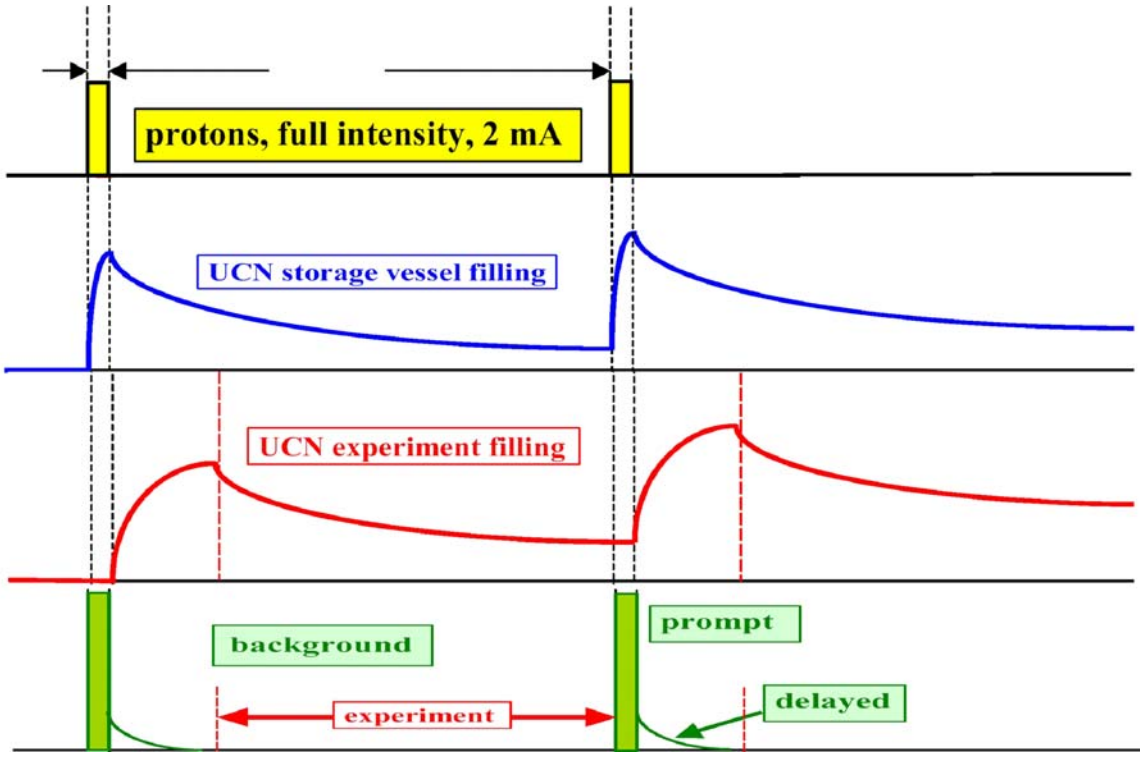

Figure 2.8: PSI UCN source operating scheme using a 1% duty cycle. UCN intensities in the storage tank and in the experiment and expected background are plotted in arbitrary units over time (figure by J. Sromicki).

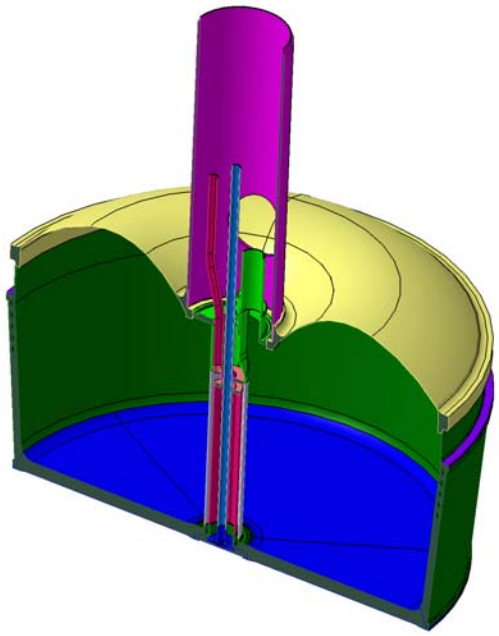

Figure 2.9: A cut through the sD_2 container.

Figure 2.10: The toroidal shaped sD_2 converter lid made from AlMg3.

Chapter 3

The Moderation of Neutrons

Detailed knowledge about the properties of the converter material is important for optimal UCN source performance. The main efforts are directed towards investigations of superfluid helium [51, 52, 53, 54, 55, 56, 57] and sD_2 [58, 59, 60, 61, 62, 63, 64, 65, 45, 66, 2, 1]. Alternative candidate materials with the appropriate characteristics have been proposed; solid heavy methane CD_4 [67] and solid oxygen O_2 [69, 70, 71] are currently under study.

The essential issue is an efficient use of the UCN moderator. The moderation of neutrons is based on their interactions with a scattering medium and the scattering process is characterized by the differential scattering cross section. This is determined by studying the conservation of energy and momentum in the center-of-mass of incident neutron and struck nucleus, molecule or material, and expressing them in the laboratory system reference frame. The scattering processes may be classified by separating them between (i) elastic and inelastic interactions depending on the way how the energy is interchanged in the collision, and (ii) coherent and incoherent depending on the interference effects. During elastic collisions in the center-of-mass system, the kinetic energy and momentum of a neutron are conserved, while during the inelastic collisions, the scatterer undergoes a change of quantum state in the interaction causing the change of neutron energy. In case of fast neutrons with energies greater then 1 eV, the target atoms can be considered free and at rest before collision and the scattering process can often be considered in terms of elastic scattering. At smaller neutron energies, the thermal motion of the scattering atoms becomes noticeable; collisions in which the neutron gains energy become possible, and the probability for collisions with an energy loss becomes smaller (see Figure 3.2). Furthermore, a low energy neutron interacting with a molecule may be scattered coherently from different nuclei or excite various vibrational, rotational, or translational modes of a molecule; and in interactions with a crystal, it may undergo Bragg scattering or excite vibrational modes (phonons) of the crystal. In order to understand the full picture of the moderation process, it is important to investigate all possible channels of energy exchange between the neutron and the struck atom.

In this chapter the moderation process will be described by means of elastic scattering and a simple model describing the neutron moderation is proposed. The detailed treatment of the neutron scattering including various aspects of the interaction between the neutron

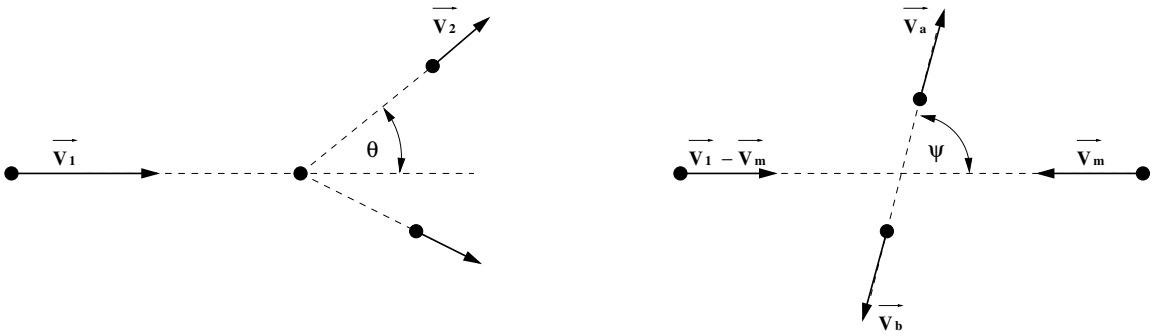

Figure 3.1: Kinematics in the laboratory (L) system (left) and center of mass (CM) system (right).

and the struck atom is discussed with relation to the experimental results in the chapter 5.

3.1 Elastic Scattering and Moderation

For sufficiently high neutron energies, the moderation dynamics can be treated by means of elastic scattering between the neutron of mass 1 and energy E_0, and a free atomic nucleus of mass A that is initially at rest. In this type of scattering, the total energy is conserved and the energy lost by a neutron is transferred to the recoiling particle. Such a moderation process takes place (i) in the heavy water moderator of the PSI UCN source, where the fast neutrons ($\sim$ 2 MeV) are downscattered to thermal neutrons ($\sim$ 25 meV) and (ii) in the solid deuterium moderator in which, neglecting the UCN production, the thermal neutrons are moderated to cold neutrons ($\sim$ 2 meV).

The energy E of a neutron after the elastic collision in the laboratory system (L) is given by:

$$E = E_0 \frac{A^2 + 2A\cos\psi + 1}{(A+1)^2} \tag{3.1}$$

where ψ is the scattering angle in the center of mass system (CM) (see Fig. 3.1). The scattering angle in the laboratory system is given by:

$$\cos\theta = \frac{A\cos\psi + 1}{\sqrt{A^2 + 2A\cos\psi + 1}} \tag{3.2}$$

It is useful to introduce the parameter α, which depends only on the mass of the struck nucleus and is equal:

$$\alpha = \left(\frac{A-1}{A+1}\right)^2 \tag{3.3}$$

Then the equation 3.1 becomes:

$$\frac{E}{E_0} = \frac{1}{2}[(1+\alpha) + (1-\alpha)\cos\psi)] \tag{3.4}$$

In view of equation 3.4 it is evident that the energy of an elastically scattered neutron always lies between αE_0 and E_0. A neutron can loose all its energy in a single collision when $\alpha = 0$, i.e. with hydrogen, while for collisions with all other nuclei, it can lose at most only a fraction of its original energy. For example, for heavy water (D_2O), the moderator material that will be used in the UCN source at PSI, $\alpha(D_2O) \simeq 0.8$ and $\alpha(D) \simeq 0.1$. At high energies ($\geq$ 100 eV), the neutron does not see the heavy water molecule and its velocity is reduced by the interactions with the deuterium atom ; at lower energies, the reduction in velocity (so-called slowing down of a neutron) by interacting with the molecule becomes relevant. Therefore, neutrons can lose 20 % or 90 % of their energy in a single elastic collision with a heavy water molecule or a deuterium atom, respectively. The second important constant is the average logarithmic energy loss ξ which helps to estimate the average number n of collisions necessary to moderate a neutron with an initial energy E_0 to the energy E. A moderator slows down neutrons the better the larger ξ is:

$$\xi = \ln E_0 - \overline{\ln E} = 1 + \frac{\alpha}{1-\alpha} \ln \alpha \tag{3.5}$$

For hydrogen ξ is equal 1 and for large A can be quite well approximated by:

$$\xi \simeq \frac{2}{A + \frac{2}{3}} \tag{3.6}$$

The average number n of collisions is calculated with the following formula:

$$n = \frac{\ln(E_0/E)}{\xi} \tag{3.7}$$

For heavy water molecule $\xi(D_2O) \simeq 0.09$ and for deuterium atom $\xi(D) \simeq 0.75$. The number of collisions necessary to moderate neutrons of 2 MeV to 25 meV in heavy water can be estimated by dividing the energy range into two regions: (i) neutron energies between 2 MeV and 100 eV, slowing down on deuterium atoms, $n \simeq 13$ and (ii) neutron energies between 100 eV and 25 meV, slowing down on heavy water molecules, $n \simeq 92$. Further slowing down of neutrons of 25 meV to 2 meV happens in solid D_2 and requires about $n \simeq 4$ single collisions.

While considering the moderator material one needs to take into account how often the neutrons will collide with the atoms of the moderator and also what is the probability for a neutron to be captured by the nucleus. Those two processes are described by the scattering Σ_s and absorption Σ_a cross section, respectively. Combining the parameter ξ with the macroscopic scattering and absorption cross section leads to the quantity called moderating ratio $\xi\Sigma_s/\Sigma_a$, which is the best measure of the moderating properties of the material.

In the infinite, non-absorbing medium neutrons come into an equilibrium with the thermal motion of the scattering atoms and the neutron flux has a Maxwell distribution of energies $\Phi(E) \sim E \exp(-E/k_BT)$ where T is the temperature of the moderator and $k_B = 8.6 \times 10^{-5} eV/K$ is the Boltzmann constant. The differential scattering cross section $\sigma_s(E_0 \rightarrow E)$ in a state of true thermodynamic equilibrium follows the principle of detailed

balance known from the statistical physics:

$$E_0 \exp\left(-\frac{E_0}{k_B T}\right)\sigma_s(E_0 \rightarrow E) = E \exp\left(-\frac{E}{k_B T}\right)\sigma_s(E \rightarrow E_0) \tag{3.8}$$

which says that in equilibrium, as many neutrons make transitions from the energy E to the energy E_0 as make transitions from the energy E_0 to the energy E.

The differential scattering cross section $\sigma_s(E_0 \rightarrow E)$ for an ideal, monoatomic gas consisting of atoms of mass $M \approx Am_n$ and energy independent scattering cross section σ_{sf} can be calculated with the help of the laws of elastic collisions derived above. Following [50] the scattering cross section for processes in which a neutron of velocity[1] v_0 is scattered into the velocity interval $(v,\, v + dv)$ is:

$$\sigma_s(v_0 \rightarrow\ v)dv = \frac{1}{2v_0}\int_0^{\infty} dV \int_{-1}^{+1} v_{rel}\ d\mu\ \sigma_{sf}\ P(V)\ f(v \rightarrow\ v_0)dv \tag{3.9}$$

where $\mu = \cos\theta$ is the cosine of the scattering angle in the laboratory system, V is the velocity of gas atoms which obeys the Maxwell-Boltzmann velocity distribution:

$$P(V)dV = \left(\frac{4}{\sqrt{\pi}}\right)\left(\frac{M}{2k_B T}\right)^{\frac{3}{2}} V^2 \exp -\frac{MV^2}{2k_B T}dV \tag{3.10}$$

The neutron velocity in the laboratory system after the collision is given by:

$$v = \sqrt{v_m^2 + \left(\frac{A}{A+1}\right)^2 v_{rel}^2 + 2v_m \frac{A}{A+1} v_{rel}\cos\psi} \tag{3.11}$$

where v_m is the velocity of the neutron in the neutron - gas atom center-of-mass system:

$$v_m = \frac{\sqrt{v_0^2 + A^2V^2 + 2Av_0V\mu}}{A+1} \tag{3.12}$$

and v_{rel} is the relative velocity in the laboratory system:

$$v_{rel} = \sqrt{v_0^2 + V^2 - 2v_0 V cos\psi} \tag{3.13}$$

here ψ is the scattering angle in the center-of-mass system. The probability $f(v_0 \rightarrow v)$ that the neutron falls into the velocity interval $(v,\, v + dv)$ after the collision is given by:

$$f(v_0 \rightarrow v) = \begin{cases} 0 & v < v_{min} \\ \dfrac{2v}{v_{max}^2 - v_{min}^2} & v_{min} < v < v_{max} \\ 0 & v > v_{max} \end{cases}$$

[1] In the laboratory system

By setting $\eta = \frac{A+1}{2\sqrt{A}}$, $\rho = \frac{A-1}{2\sqrt{A}}$ and carrying out the integration over v, $\sigma_s(E_0 \to E)$ becomes:

$$\sigma_s(E_0 \to E) = \frac{\eta^2}{2}\frac{\sigma_{sf}}{E_0}\exp\left(E_0/k_BT\right)\left\{\exp\left(E/k_BT\right)\mathrm{erf}\left[\eta\sqrt{\frac{E_0}{k_BT}} - \rho\sqrt{\frac{E}{k_BT}}\right] + \right.$$
$$+\exp\left(-E_0/k_BT\right)\mathrm{erf}\left[\eta\sqrt{\frac{E}{k_BT}} - \rho\sqrt{\frac{E_0}{k_BT}}\right] - \left|\exp\left(-E/k_BT\right)\mathrm{erf}\left[\eta\sqrt{\frac{E_0}{k_BT}} + \rho\sqrt{\frac{E}{k_BT}}\right] + \right.$$
$$\left.\left. - \exp\left(-E_0/k_BT\right)\mathrm{erf}\left[\eta\sqrt{\frac{E}{k_BT}} + \rho\sqrt{\frac{E_0}{k_BT}}\right]\right|\right\} \tag{3.14}$$

The formula 3.14 can be now applied for solid deuterium moderator (A = 2, T = 8K). In Figure 3.2, $\sigma_s(E_0 \to E)E_0(1-\alpha)/\sigma_{sf}$ is plotted as a function of E/E_0 for two cases : for thermal neutrons with the average energy of about 25 meV (E_0 = 36 k_BT) and for cold neutrons with the average energy 2 meV (E_0 = 3 k_BT). By looking at the plots, one can see that at lower neutrons energies i.e. for cold neutrons, collisions in which neutrons gain energy become possible. This simple model shows the influence of the thermal motion of moderator atoms on the neutron scattering but it doesn't take into account neither the 'internal' degrees of freedom of the scatterer nor the bindings between the scattering atoms which become important at smaller neutron energies.

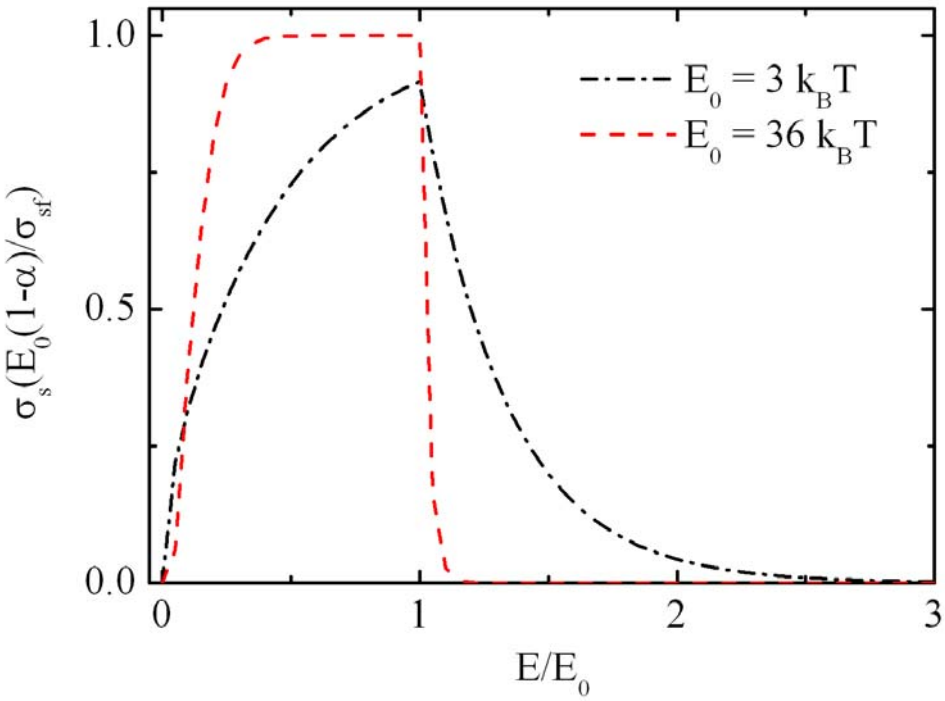

Figure 3.2: The differential scattering cross section of a gas of D_2 molecules, simplified model of scattering of thermal (red, dashed curve) and cold (black, dotted curve) neutrons on a hypothetic gas of D_2 molecules at T = 8 K, taking into account only the thermal motion of the molecules.

Chapter 4

Experiment

Our investigations of UCN production started in the summer 2004 at the Swiss Spallation Neutron Source (SINQ) at PSI, using the polarized CN beamline for fundamental physics (FUNSPIN). Two experiments based on the same concept of measuring UCN produced from the CN beam were performed.

The first experiment took 10 days of beam time during which we successfully measured the absolute UCN production cross sections in gaseous, liquid and solid D_2 [2] and the temperature dependence of the UCN production in sD_2. Additionally the polarization of UCN produced from polarized CN in sD_2 was measured (see appendix A) .

The second experiment was conducted in autumn 2005 at the same beamline. During 5 weeks of beam time we have measured the production of UCN from the CN beam in D_2, O_2 and CD_4 as well as the CN transmission through all three materials [3]. Moreover, in order to understand underlying processes of the UCN production in gaseous and solid D_2 the CN energy dependent UCN production was measured [4].

4.1 Setup

The idea of the experiment is simple; cold neutrons arrive via a "flight tube" (1 in Figure 4.1) to the target cell (2), the CN and UCN leaving the cell are measured by a detector system. The target cell is mounted on a cryostat and can be filled with D_2, O_2 or CD_4, as appropriate, in the temperature range between 8K and room temperature. The CN interact with the material in the cell and some of them get downscattered to UCN energies. Both, the CN and UCN enter the guide system following the target cell and after roughly 0.6 m UCN are separated from CN by a mirror (3) which is usually a silicon wafer coated with UCN reflecting material with high Fermi potential V_F[1] (see Figure 4.4). UCN are reflected upwards by this mirror and after 1 m are again reflected by a second mirror (4) into a horizontal guide section. This section consists of a storage tube (6) and two UCN shutters: the entrance shutter (5) and the exit shutter (7).The UCN that passed the storage tube are later detected by the ^{3}He UCN detector (8). The assembly of items 5-8 is rotated by

[1]The Fermi potential is a coherent strong interaction potential describing the interaction of neutrons at material surface, see [76]

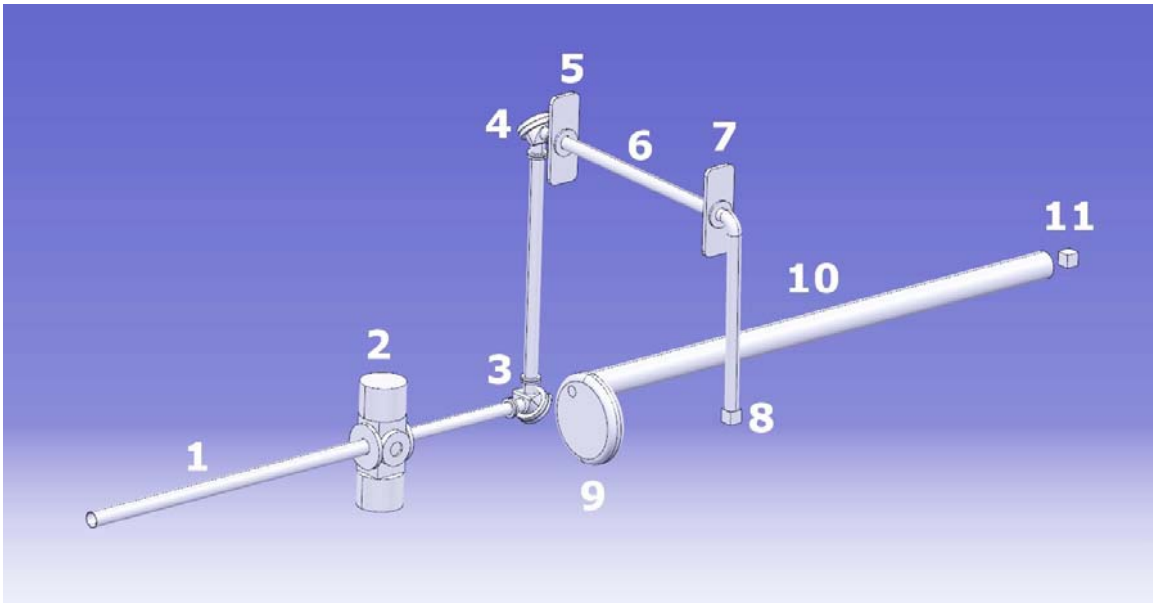

Figure 4.1: A 3D view of the experimental setup.1-CN "flight tube", 2- cryostat with the target cell, 3 & 4-UCN reflecting mirrors, 5-entrance UCN shutter, 6-storage tube, 7-exit UCN shutter, 8-UCN detector, 9-CN chopper, 10-CN TOF tube, 11-CN detector. For the CN transmission and UCN production measurements we have used the full CN beam. For the CN energy dependent UCN production measurements, a velocity selector was mounted upstream of the cryostat.

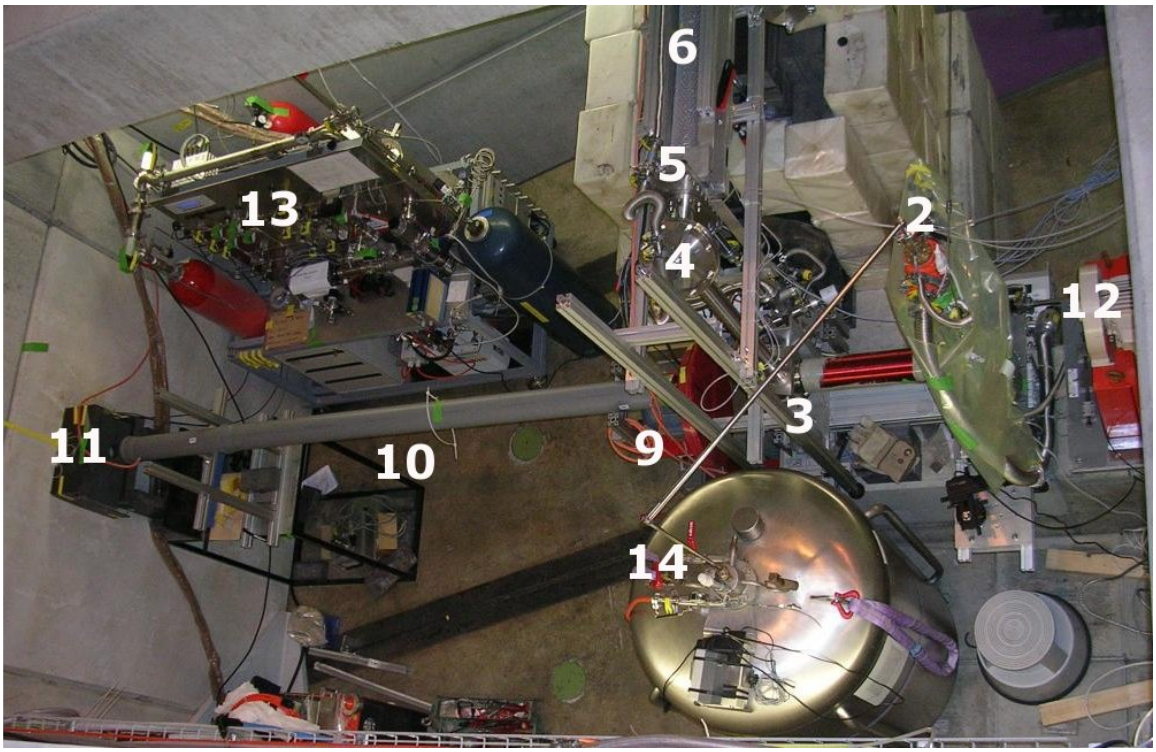

Figure 4.2: A photograph of the experimental setup. Top view. The numbers which describe the parts of the setup are the same as above, in Figure 4.1, additionally: 12-velocity selector mounted in front of the cryostat (see also Figure 4.5), 13-gas system (see also Figures 4.8 and 4.9), 14-He dewar connected via transfer line to the cryostat.

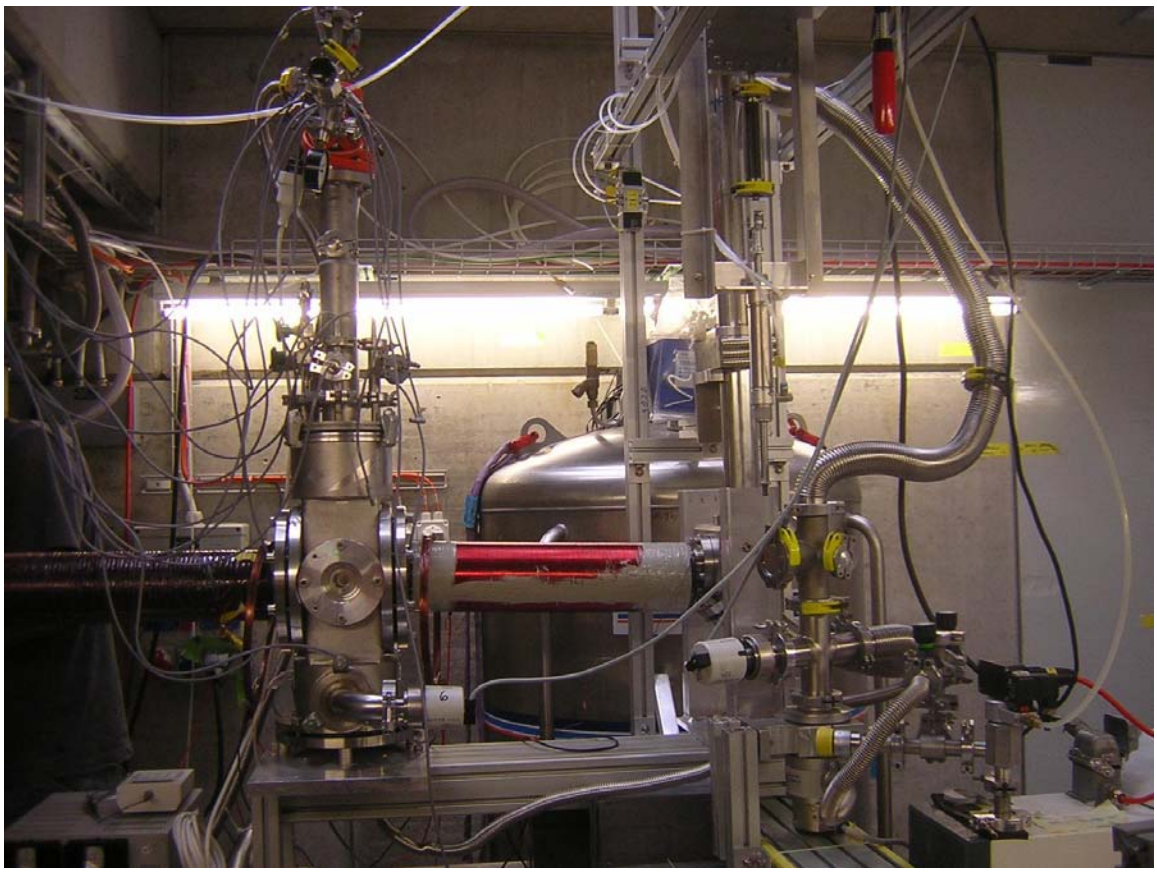

Figure 4.3: A photograph of part of the experimental setup, side view. The cold neutron beam from the SINQ source comes from the left and is collimated (40 mm) over a length of about 1.5 m before hitting the target cell, which sits behind a 38 mm aperture. The cell with the UCN converter under investigation is mounted on the cryostat and allows it to be cooled down to 8 K. The Helmholtz coils around the cryostat, the CN coil and coil surrounding the neutron guide generate the magnetic field of about 10 Gauss strength for guiding the neutron spin (see Appendix A)

Figure 4.4: The UCN reflecting mirror, the Fe coated sillicon wafer mounted on the Al support.

90 degrees around the vertical guide so that the UCN detector is moved out of the CN beam axis. The CN are transmitted through the lower mirror (3) and then pass through a chopper (9), enter the time of flight tube (10), and are detected in the CN detector (11).

Below, some parts of the experimental setup are described.

4.1.1 CN Beam without Velocity Selector

CN enter the experiment through a 40 mm long, 42 mm diameter Pb collimator, clad with a 1 mm thick layer of ^{6}LiF polymer, and a pneumatically driven rotating shutter. After the shutter, the neutrons enter a vacuum flight tube through a 100 μm Zr window. The final collimation of the CN beam is set up with two elements: (i) a 42 mm aperture Cd-Pb sandwich in front of the cryostat and (ii) a 38 mm aperture Cd element which defines the final beam spot and is mounted on the 80 K thermal shield of the target cell.

4.1.2 Velocity Selector

The mechanical velocity selector [72, 73] is mounted between the exit of the neutron channel at FUNSPIN and the cryostat (see Figure 4.5). It consists of a horizontal rotating cylindrical drum, driven by an electrical motor and made of a series of Gd_2O_3[2] coated blades placed

[2]Gadolinium has a high absorption cross section of 49700 barn at 2200 m/s.

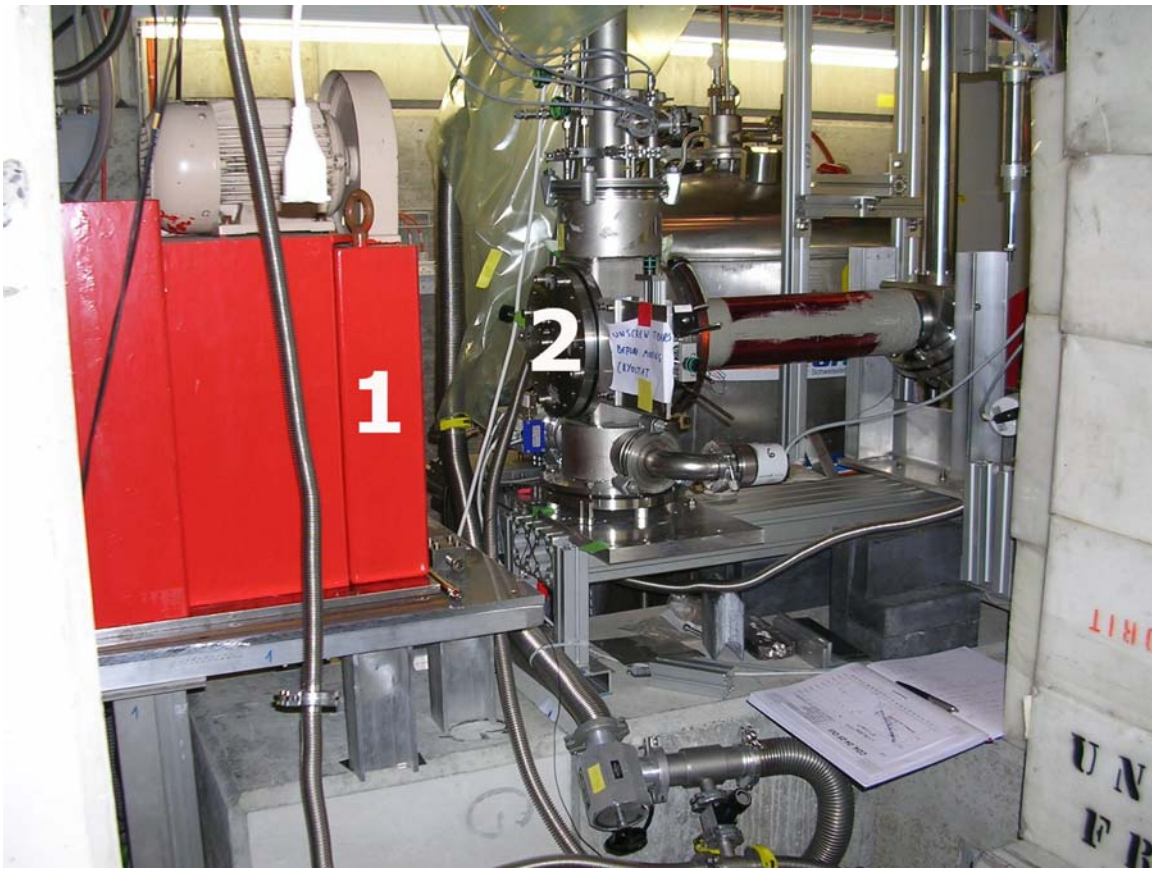

Figure 4.5: The picture shows velocity selector (1) mounted in front of the cryostat (2)

in the steel housing which is mounted on the rotating table. The blades form narrow slits through which the neutrons pass [72]. The rotating table allows to tilt the axis of rotation relative to the neutron beam. By changing the tilt angle of the velocity selector and its rotation frequencies, different parts of the velocity spectra of the CN beam can be chosen covering the full spectrum. Depending on the specific settings of the VS (i.e. rotation frequency and tilt angle), velocity resolutions of about 20% were achieved, measured with neutron TOF (1 - 5% resolution). The corresponding energy spectra for the selected bins are displayed in Figure B.1 in Appendix B.

4.1.3 The Target Cell

The target cell (see Figure 4.6) is made from an aluminum alloy AlMgSi1 and has four windows: two optical windows and two windows for neutrons. The optical windows, made from sapphire, serve for optical investigation of the crystal and for Raman spectroscopy (see section 4.1.4). The neutron windows, made from AlMg3, are 0.15 mm thick and have 40 mm diameter. The entrance window of the target cell is Ni coated on the inside for UCN reflection. The distance between the entrance and exit window is 40 mm. The cell is

mounted on a helium flow cryostat [3] (see Figure 4.7) and connected to the gas system (see Figure 4.9, Figure 4.8 and [74]) with a total volume of about 80 dm^3. Following the cell, a short section of 45 mm inner diameter UCN guide (Ni-coated Al) starts 0.5 mm after the neutron exit window, and ends 0.5 mm in front of a 16 μm Al foil separating the cryostat and external UCN guide vacuum.

4.1.4 The Raman Spectroscopy

The system which is used for Raman spectroscopy consists of three main parts: the argon-ion-laser, the Raman head, and the Raman spectrometer. A detailed description of the setup and method of the data analysis can be found in [74]. Raman spectroscopy is used to investigate the ratio c_0 of ortho-D_2 to para-D_2 as well as the crystal structure. Hydrogen contaminations in form of HD or H_2 can also be measured. Figure 4.10 shows spectrum of rotational excitations for liquid ortho-deuterium with $c_0 = (98.7 \pm 0.2)\%$. The ortho-D_2 concentration c_0 is calculated from the intensity ratio of the Raman lines for the J = 0 → 2 and J = 1 → 3 rotational transitions (lines $S_0(0)$ and $S_0(1)$ respectively) taking into account the proper transition matrix elements[4].

$$c_0 = \frac{5/3 I_{\text{para}}}{I_{\text{ortho}} + 5/3 I_{\text{para}}} \tag{4.1}$$

where I_{para} and I_{ortho} are the integrals over the fitted para and ortho lines, respectively. Figure 4.11 shows the Raman signal for solid ortho-deuterium at temperature of 18 K. The $S_0(0)$ line is split into a triplet which is a signature of the hcp structure of the crystal [75]. The hcp symmetry of deuterium crystal makes the J = 2 level form three energy bands belonging to m = ± 1 (α) m = ± 2 (β) and m = 0 (γ). Change of the S_0 line shape with crystal temperature is shown in Figure 5.5 With the same setup for Raman spectroscopy it is also possible to study the C-D stretch vibrations in the CD_4 crystals. The Raman spectra of solid CD_4 are shown in the Figure 5.10

4.1.5 UCN Detection System

The UCN detection system starts with the reflecting mirror, placed at the end of the first UCN guide[5], approximately 0.6 m after the target cell. During the first experiment we have used Fe coated Si wafer (see below), and during the second experiment we have used Ni coated Si wafer, and later, DLC coated Al-foil. The reason for using different mirrors was because of the measurements of UCN polarization (see below and appendix A). The Fermi potential of the mirrors has been measured by means of cold neutron reflectometry which measures the Fermi potential by observing the critical reflection angle for a sample surface

[3] The cryostat is designed to obtain temperatures down to 8 K in the target cell

[4] To describe the rotational transitions induced by the photons, one has to change from the product basis of the single angular momenta to the common basis of the total angular momenta. This basis change is given by the Clebsch-Gordan coefficients $\sqrt{5/3}$ and 1.

[5] All the UCN guide system has a 56 mm inner diameter and is made from stainless steel chemically coated with Ni; the nickel layers made by this process contain several percent of phosphorus and are nonmagnetic.

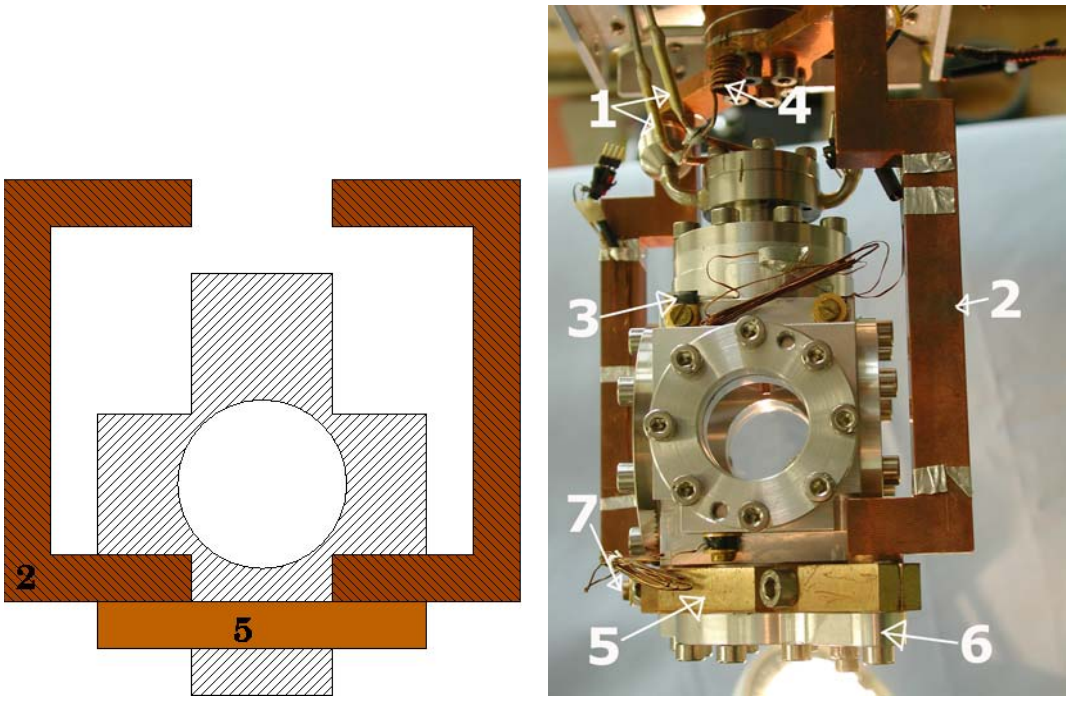

Figure 4.6: A photograph of the target cell mounted on the cryostat and a schema of the cell with a copper support. Numbers denote the following parts: 1 - the capillaries, through which D_2, O_2 and CD_4 were transported to the cell; the cell has two capillaries, the shorter one, used during freezing from the liquid phase, and the longer one (the end of this one is visible inside the cell) used during freezing from the gas phase; 2 - the copper rod connecting the cell to the bottom of the He flow cryostat; 3 - the temperature sensor; 4 - the copper wire connecting the cold finger with the capillary; 5 - the copper clamp holding the cell; 6 - the bottom of the cell; 7 - the heater.

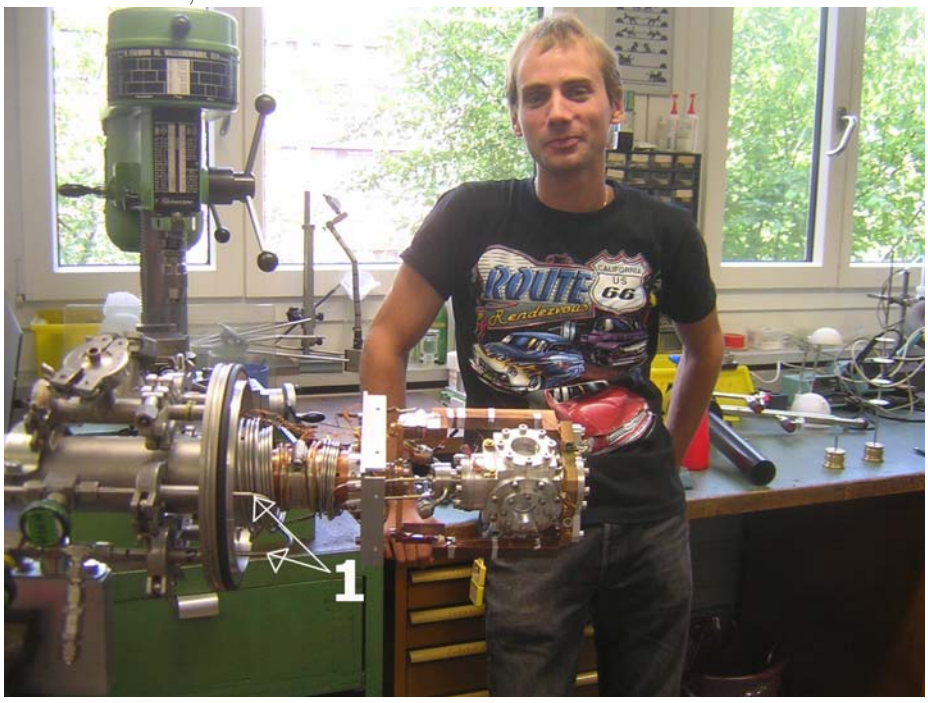

Figure 4.7: A photograph of the cryostat with target cell mounted. The capillaries (1) are wrapped around the cryostat.

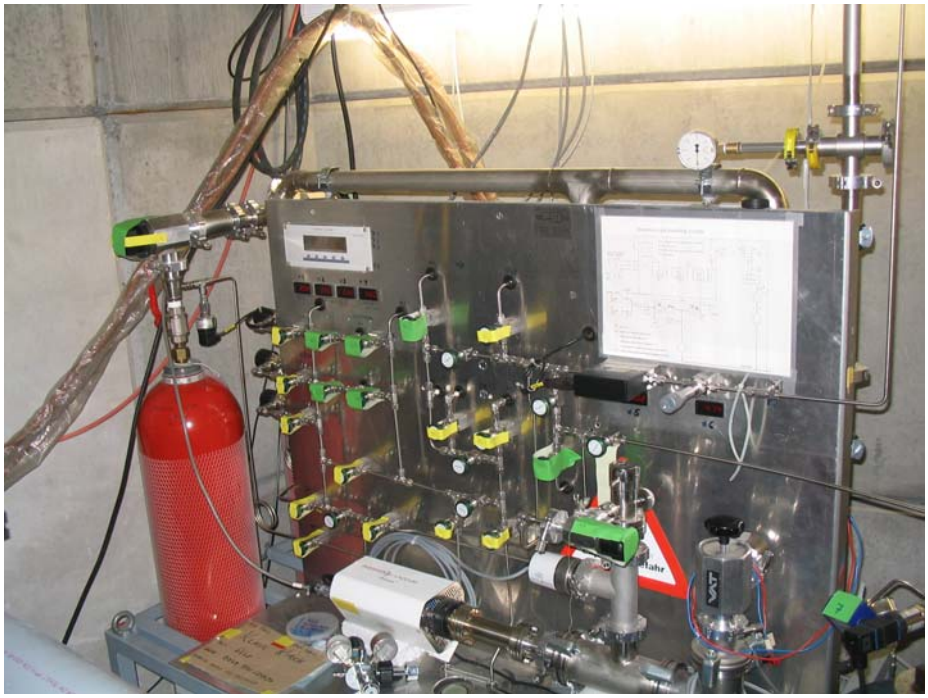

Figure 4.8: Front view of the gas system of the UCN production experiment.

Figure 4.9: Rear view of the gas system. In the middle one can see the ortho/para converter.

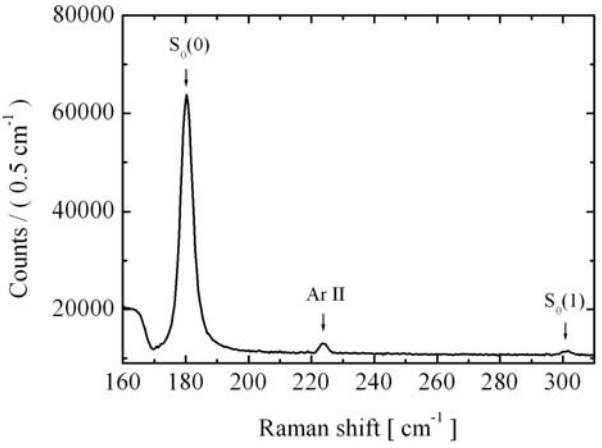

Figure 4.10: A Raman spectrum of liquid ortho-D_2 ((98.7 ± 0.2)%). The Ar II (493.3 nm) line, seen in the figure, is produced by the laser.

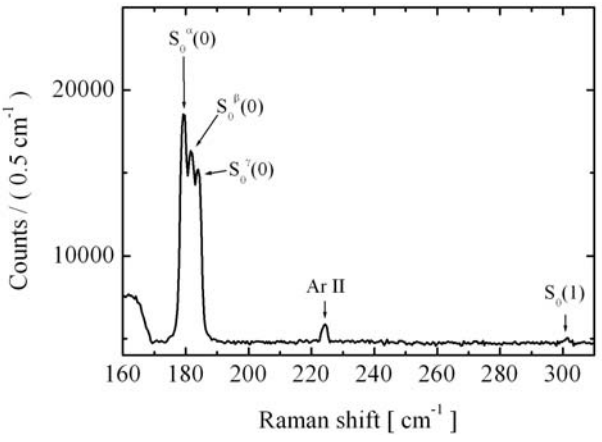

Figure 4.11: A Raman spectrum of solid ortho-deuterium at 18K.

[76].

The next part of the UCN detection system is the vertical UCN guide which ends with the second UCN mirror (Ni coated Si wafer) after approximately 1 m. The UCN lose 100 neV of its energy on the way up due to gravity. Afterwards the UCN enter a storage bottle made of Be-coated quartz[6] which can store neutrons up to about 250 neV. The bottle is equipped with two pneumatically driven shutters so that it can be opened and closed at either end (see Figure 4.12). The shutters consist of a 15 mm thick sliding plastic sheet between stainless steel plates. In the open position, a 15 mm long piece of UCN guide tube is moved into the neutron path, in the closed position, the shutter is the lid of the neutron bottle and the inner side is covered with (i) 100 μm PET foil coated with DLC (shutter on the entrance side of the storage bottle), (ii) 100 μm Al foil coated with DLC (exit shutter). The second shutter, on the exit side, connects via a bend and another 80 cm long guide to the UCN detector. The detector is a gas counter[7] with 18 hPa ^{3}He and 10 hPa CO_2 in about 1100 hPa Ar; it is well shielded with a layer of Cd close to the detector and the final UCN guide, layers of borated plastic, and more then 0.5 m paraffin blocks.

Fe Magnetic Mirror and Fe-Analyser

During both UCN production experiments, the conservation of the neutron polarization was investigated (see appendix A). The polarization of UCN in the first experiment was analyzed using a magnetized mirror (10 cm diameter Si wafer with 110 nm Fe sputtered onto it). An arrangement of permanent magnets and a return yoke on the back of the mirror allowed it to be fully magnetized in its central region with some imperfections at the edges. The Fe-analyser was designed to investigate the polarization of UCN during the second UCN production experiment in 2005. It consists of Fe-coated Si-waver (200 nm of Fe layer sputtered on 105 μm Si-waver) mounted inside the vertical UCN guide, 300 mm from the lower mirror and 505 mm from the upper mirror. The magnetic field needed to fully magnetize the iron was created by permanent magnets with the field strength around 200 Gauss. Both configurations (magnetized mirror and Fe-analyser) were checked using the polarization option of the neutron reflectometer AMOR at SINQ [77].

4.1.6 CN Detection System

Cold neutrons to reach the TOF system first pass through the mirror and a 10 mm hole in the ^{6}LiF beam dump (see Figures 4.14, 4.15, 4.16), 100 μm Al vacuum window (see 1 in Figure 4.17) and a one-disc-one-slit chopper placed 220 mm futher downstream. The chopper is operated in air at the rotation frequency of 25 Hz with about 1/300 open to close ratio. The CN packets created by the chopper subsequently pass through the He flushed flight tube of 2640 mm length with 16 μm Al entrance and exit windows and are detected in a 'thin' CN detector (the same as used in [78]). 'Thin' refers to a small amount of ^{3}He in the counting gas which should result in a $1/v$ dependence of the detector efficiency on CN velocity v. The $1/v$ dependence for detector efficiency is discussed in the appendix B. The

[6]The Be-coated tube was obtained from the Petersburg Nuclear Physics Institute, Gatchina, Russia.
[7]The UCN detector was obtained from the Joint Institute for Nuclear Research, Dubna, Russia.

Figure 4.12: Building the Al support for the storage bottle and connecting the shutters.

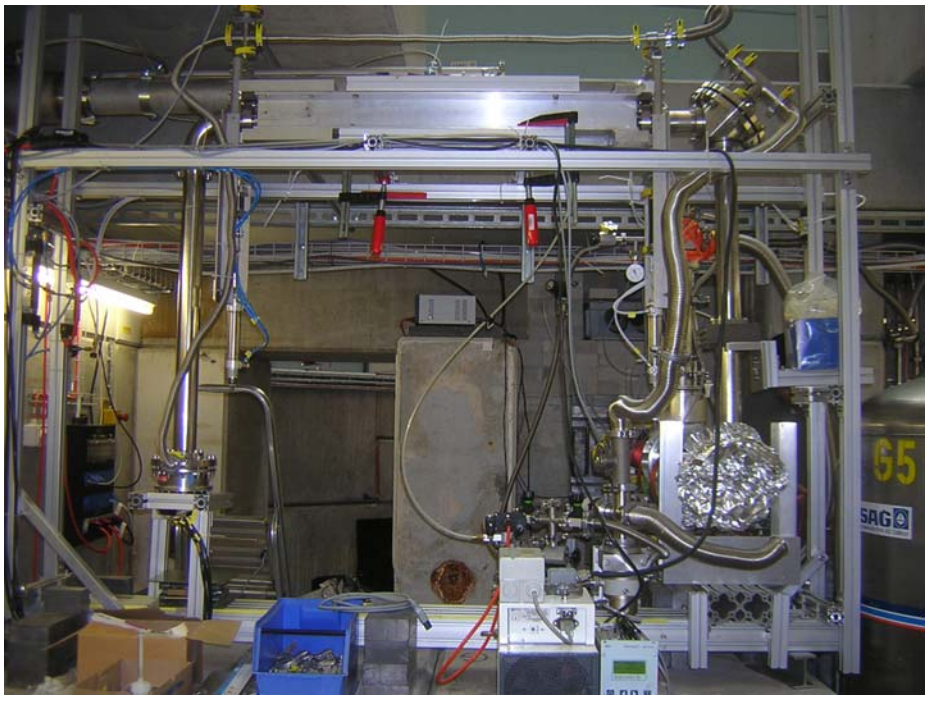

Figure 4.13: The Storage bottle mounted in the UCN detection system.

TOF system was used to monitor the CN beam intensity and spectrum. It also allowed measurements of the energy dependent CN attenuation for various target conditions from which one can calculate total scattering cross sections (see section 4.3.2).

4.2 Preparation of the Samples - Freezing Methods

The cell is designed in such a way that the crystals can be frozen from the liquid or gaseous phase. A high-resolution digital camera mounted close to one of the optical windows monitors the process of growing crystals. The gases D_2, O_2 and CD_4 are kept in storage containers, connected to the gas system. The tubing of the gas system is made from stainless steel (4 mm ID) in most parts and uses standard stainless steel Swagelok connectors and bellow valves (Figure 4.8, Figure 4.9). The gas passes via the gas system to the cryostat and is subsequently liquefied or solidified in the target cell. The crystals of deuterium and oxygen were frozen both from the liquid and gaseous phase, solid heavy methane was frozen only from the liquid phase.

4.2.1 Freezing from Liquid

In case of deuterium the process of freezing is carried out at a temperature close to the triple point (18.7 K) and takes usually about 12 h. The crystal obtained under these conditions is fully transparent and clear (see Figure 4.21). A detailed description of the freezing process can be found in [79]. Solid oxygen crystals are frozen to the γ phase at a temperature of 54K during 8 hours resulting in transparent crystals. The crystals of CD_4 are prepared at 90 K.

4.2.2 Freezing from Gas

The procedure of freezing solid deuterium from the gas phase takes usually about 20 hours and is shown in the Figure 4.18. The D_2 crystals grown under those condition are rather opaque (see Figure 4.19 and Figure 4.21), however, the annealing procedure, i.e. keeping the crystal at one stable temperature for about 12 hours, can improve the crystal transparency. Figure 4.20 shows the annealing process of a crystal.

In case of oxygen we have tested two methods of freezing the crystals directly from gas phase. One technique is to grow the crystal to the α-phase of solid oxygen[8]. The temperature of the cell has to be kept below 20K while the temperature of the capillary (see Figure 4.6), in order to keep oxygen in the gas phase, must be above 90K. The freezing process takes approximately 24 hours. The resulting crystal was opaque and milky. After the crystal was ready we have gradually increased the temperature. The second crystal was frozen to the γ-phase of solid oxygen. The temperature of the capillary has been kept above 90K and the temperature of the cell around 54K.

[8]However, it is not evident that we actually manage to freeze the crystal directly to the α-phase because the vapour pressure was much bigger than one expects from solid O_2 at 20K. It is possible that during this freezing process the crystal goes through the liquid or one of the high temperature phases.

Figure 4.14: The beam dump made of ^{6}LiF with aproximatelly 10 mm hole and an Al flange used for mounting the beam dump.

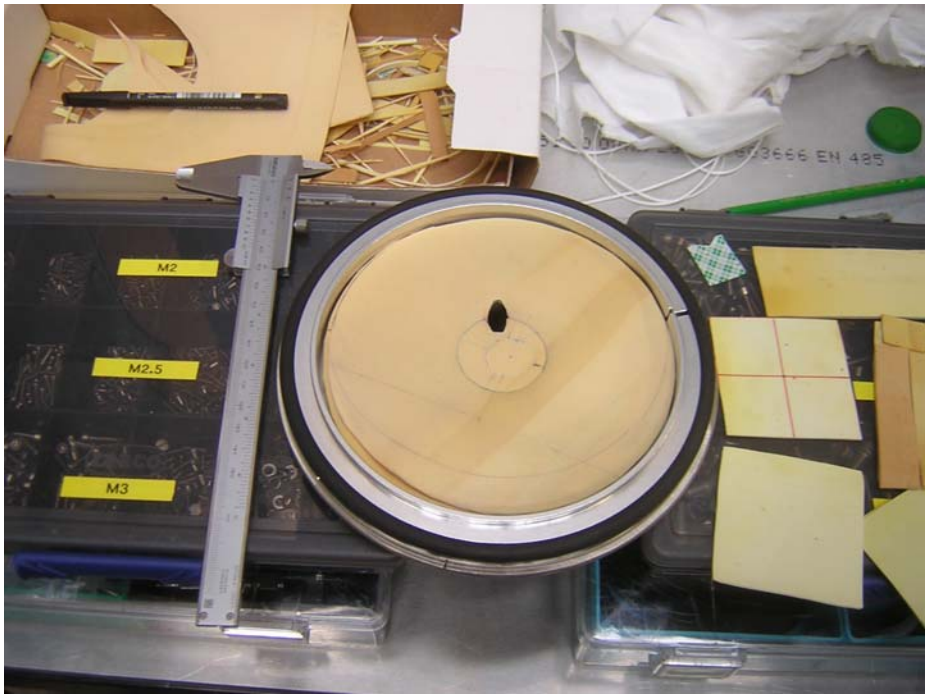

Figure 4.15: The ^{6}LiF beam dump mounted on the flange.

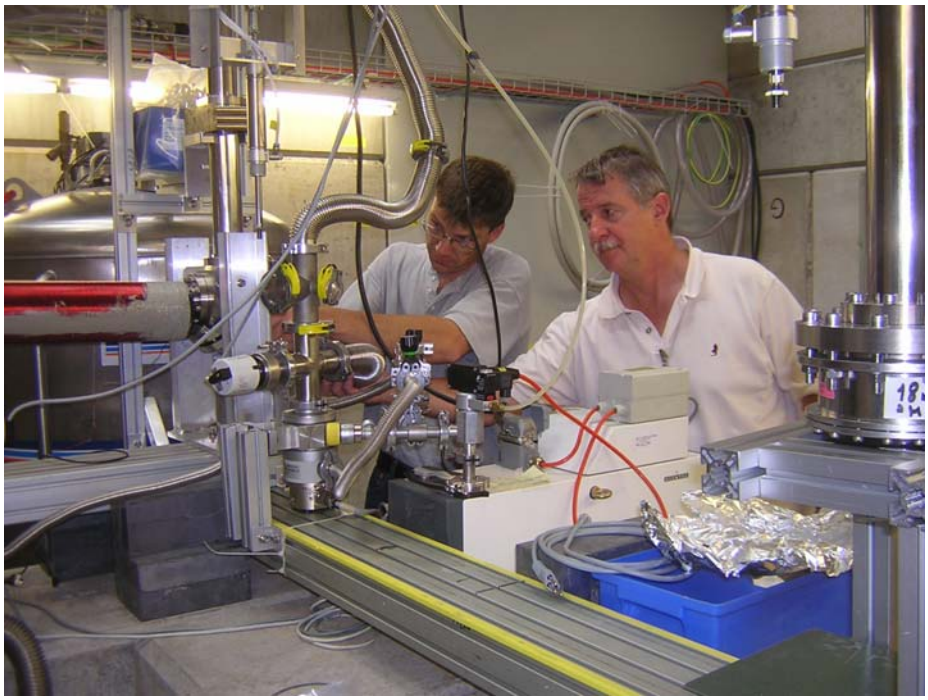

Figure 4.16: Mounting of the beam dump behind the lower UCN reflecting mirror.

Figure 4.17: The mounted flange with the beam dump and an Al vacuum window through which CN pass to enter the TOF system (1) and the UCN detector placed on the Al support (2).

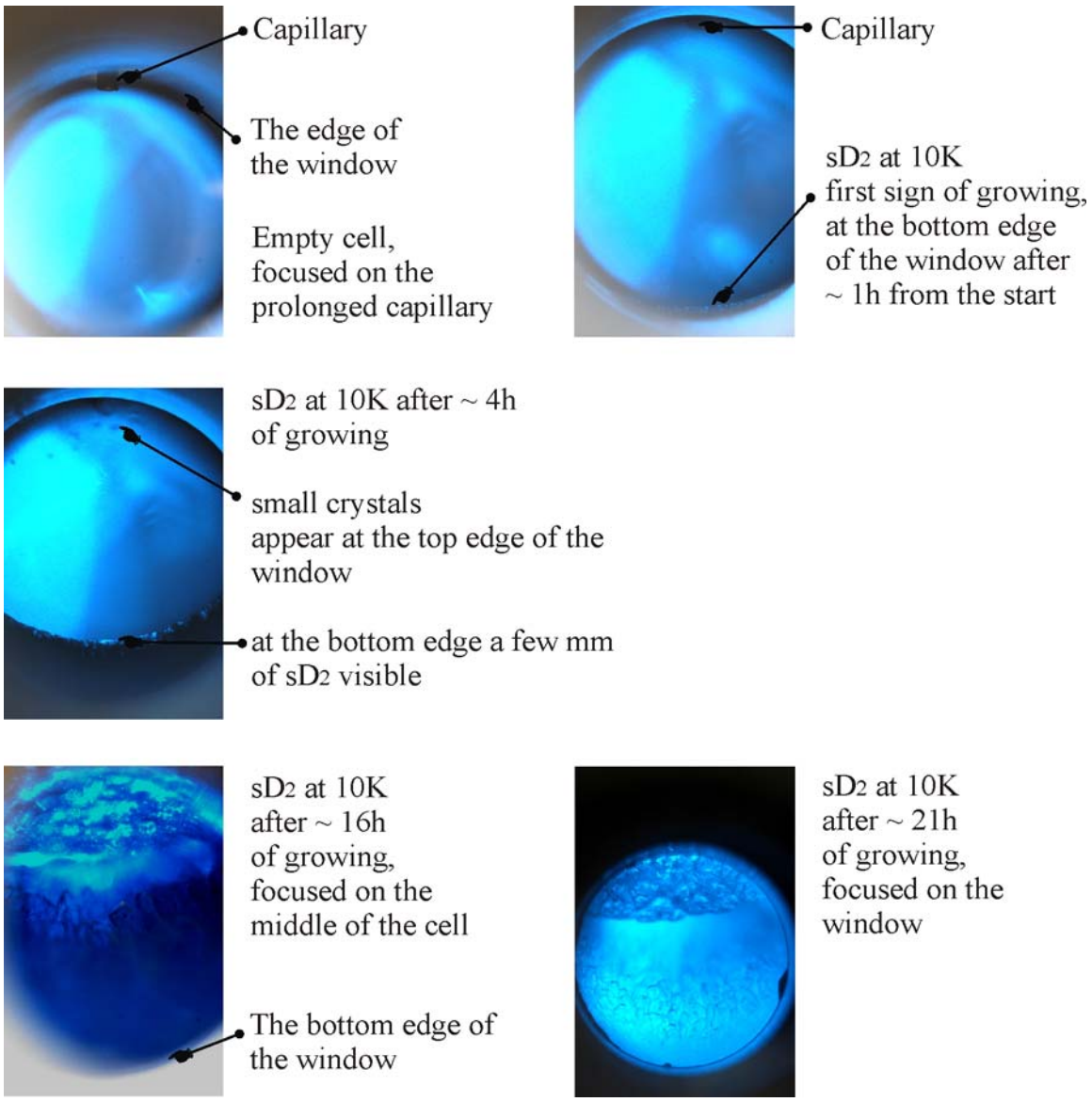

Figure 4.18: The process of growing the crystal from the gas phase is shown and described.

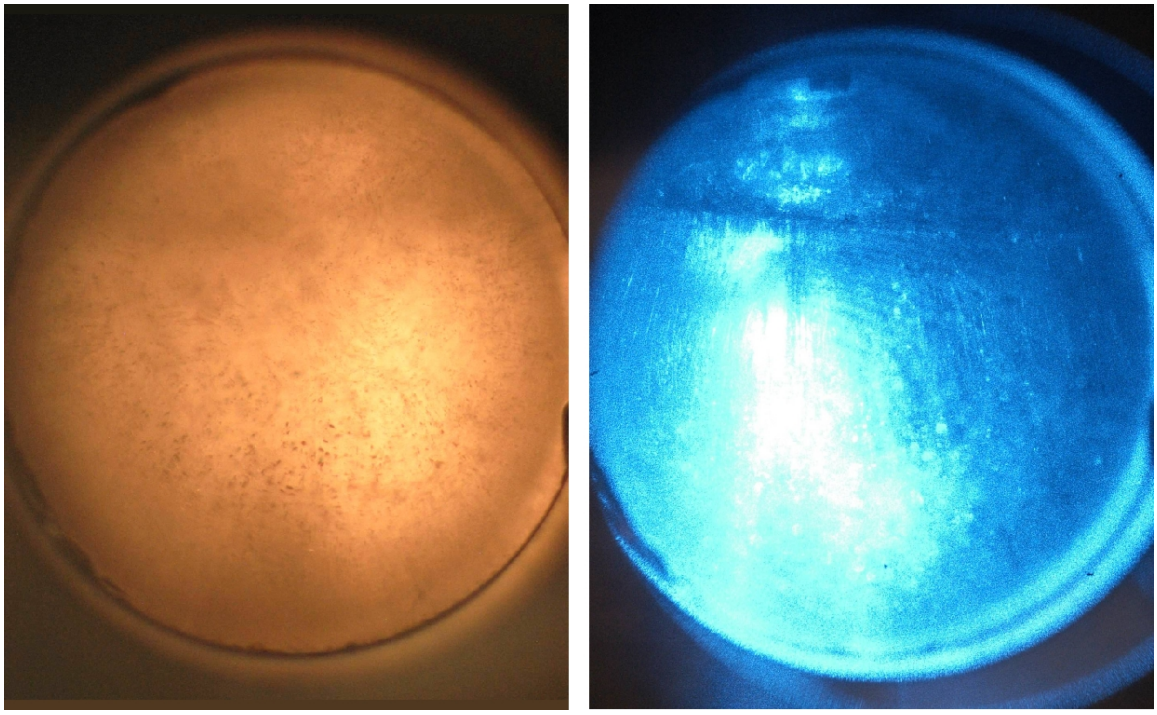

Figure 4.19: On the left side photo, the D_2 crystal at 8K grown from the gas phase in white light (the light is coming from the torch placed on the oposite side of the cell). The photo on the right side shows the same D_2 crystal at 8K, but illuminated by the blue Ar ion laser used for Raman spectroscopy.

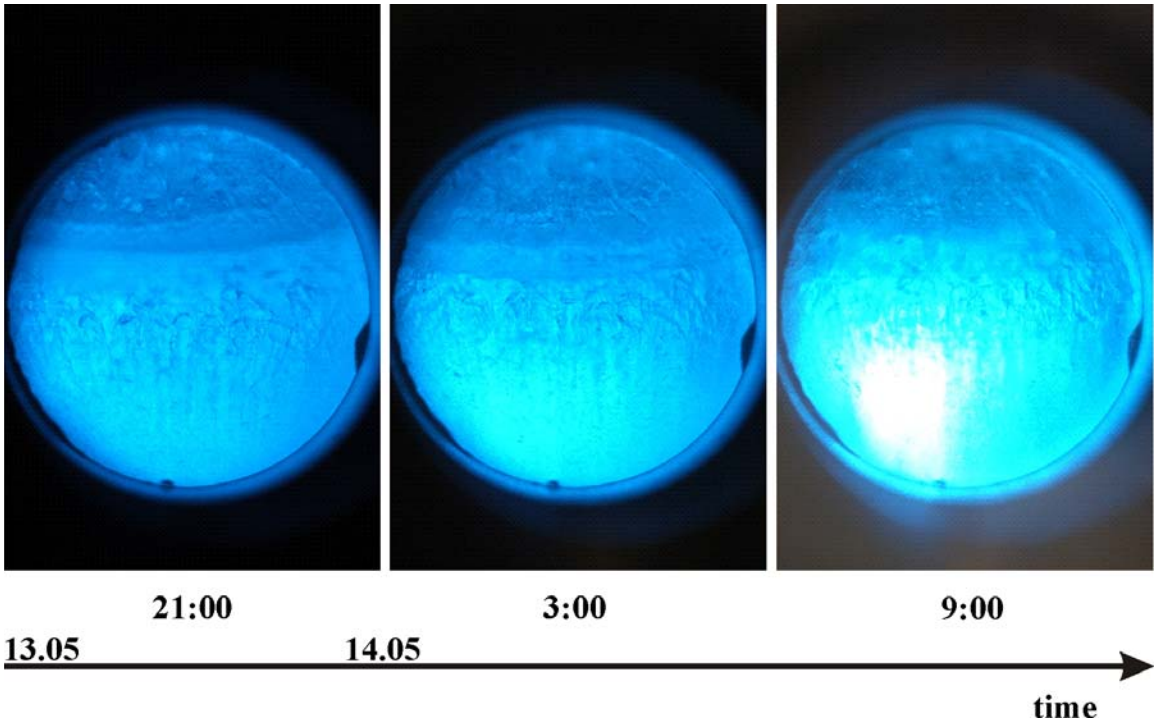

Figure 4.20: The annealing effect: while holding the crystal at the fixed temperature (here 12K) the crystal becomes more transparent for the laser light.

Figure 4.21: The comparison of the transparencies of a crystal grown from the liquid (at 18K, two pictures on the left) and grown from the gas phase (at 12K, two pictures on the right).

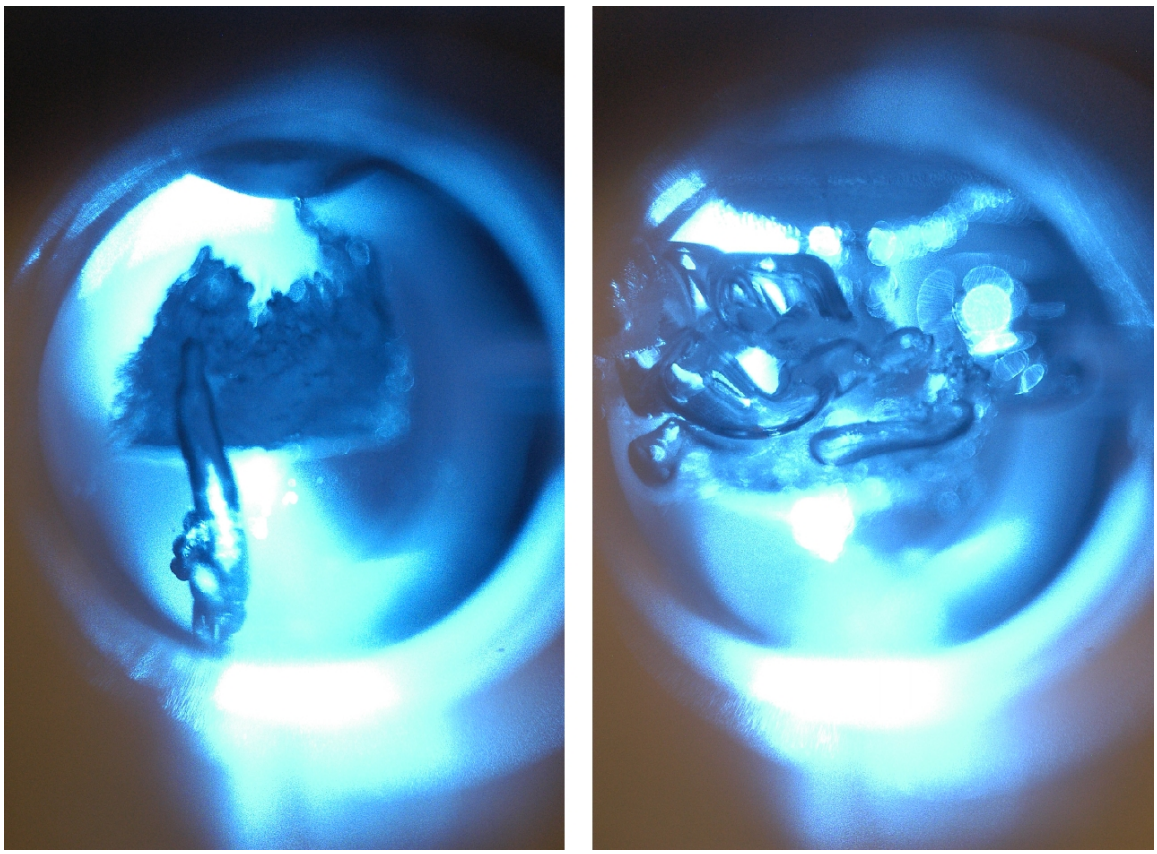

Figure 4.22: The growing of the CD_4 at 89K was more complicated than in the case of D_2. As shown in these pictures different structures were observed in the crystals,probably empty spaces.

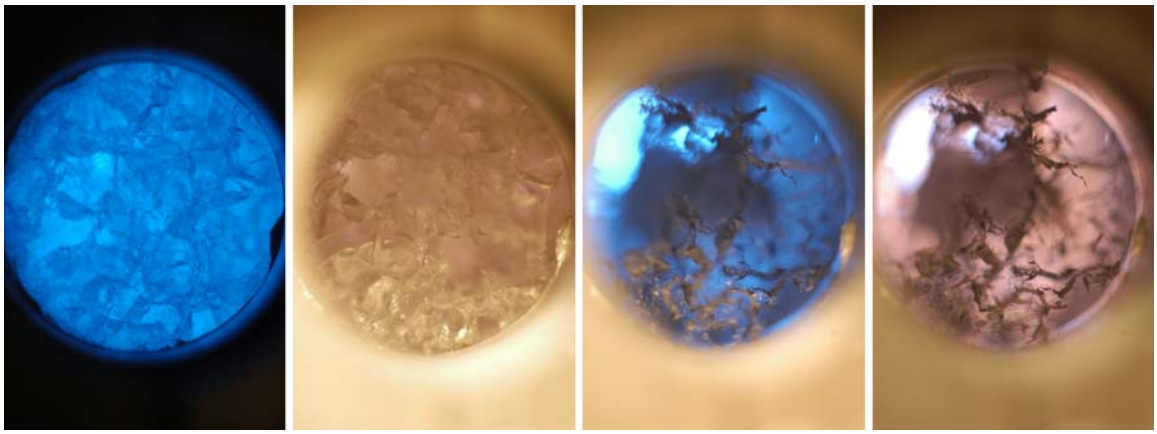

Figure 4.23: The pictures of solid CD_4 at 22K, with different illumination and focus, showing the crystal structure.

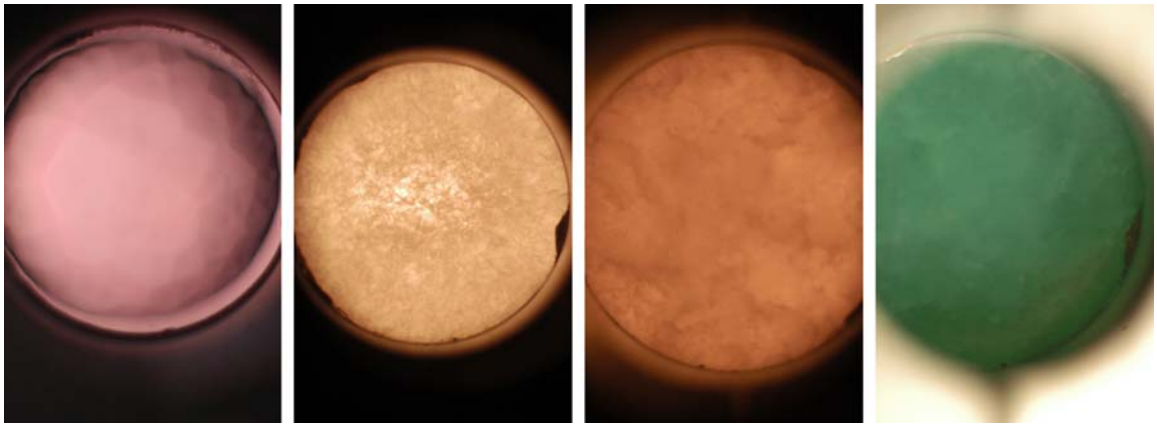

Figure 4.24: Solid O_2 at different temperatures. From left : O_2 during solidification at 50K, at 43K, at 8K illuminated with white and laser light.

4.3 The Measurements

The monitoring of the experiment is done by means of (i) the slow control system which registers the temperatures and pressures on the system, (ii) the DAQ system which records the data from both (UCN and CN) neutron detectors, from the proton beam counter, and it also monitors the status of the shutters. The details of the slow control system can be found in [80]. The DAQ system consists of (i) digital and analog DAQ controlled by the PCI cards and Labview programm, and (ii) time-of-flight DAQ. Additionally, to monitor the neutron detectors and proton beam, we have used the Borex scaler.

4.3.1 UCN Production

The experiment may be run in two ways: "storage" mode (SM) and "flow-through" mode (FM). In the storage mode, the UCN bottle (see 6 in Figure 4.1 and Figure 4.13) is filled to equilibrium. At the start of the measurement, it is open to the solid deuterium target [9] (the entrance UCN shutter open, the exit UCN shutter closed; see 5 and 6 in Figure 4.1). After a suitable time interval that allows UCN in the bottle to reach equilibrium density, the entrance UCN shutter is closed. After a few more seconds (enough time to let the non-UCN leave the bottle), the number of neutrons inside the bottle are counted by opening the exit shutter and letting them reach the UCN detector (see 2 in Figure 4.17). This method gives a direct and unbiased measurement of the UCN produced by the system. It was used during both of the experiments, the results are shown in the Figures 6.1, 6.2, 6.3, 6.4 and discussed in chapter 6.

In the flow-through mode the UCN spectrum passed is slightly wider than that in the Be storage bottle (critical velocity 6.9 m/s) but can be related to it by calculation. In this method, all shutters are open and the guide system following the target acts as a UCN spectrometer. This mode is preferred method of making (i) the integral UCN production cross section measurements in gaseous, liquid, and solid deuterium [2], (ii) the cold neutron energy dependent UCN production measurements in solid and gaseous deuterium [4], (iii) the UCN production measuremets for comparison of the efficiency of moderator materials: deuterium, oxygen, and heavy methane.

[9] Storage measurements were done only with solid deuterium

4.3.2 CN Transmission

The neutron total cross section was evaluated from the neutron beam attenuation in the measured sample. The neutron count-rate N_0 has been measured for the beam passing through an empty target cell and the neutron count-rate N_1 for the beam passing through the target cell filled with deuterium, oxygen, or heavy methane. These count-rates are related through:

$$N_1 = N_0 \exp\left(-\rho\sigma_{tot} l\right) \tag{4.2}$$

where ρ is the density of the sample, l is the length of the cell, and σ_{tot} is the total cross section. This method of determination of the total cross section assumes that the scattered neutrons do not reach the detector[10].

The raw time-of-flight spectrum is divided into 512 channels of 0.04 ms width each, with a time interval of 20.48 ms between each spectra. To obtain the total cross section, the TOF spectra for an empty and full cell are first background subtracted; as a background we take the average background of the first 10 and last 10 time bins.

[10] In order that Eq. 4.2 apply rigorously, scattered neutrons must not reach the detector i. e. the experiments must be carried out with a proper geometry which is best achieved by locating the detector as far as possible and by making the detector and the sample small. In our case the detector solid angle is about 10^{-4}.

Chapter 5

The Detailed Treatement of Neutron Scattering

The following topics in this chapter are presented, based on the deuterium example: (i) the theoretical models of a molecule and crystal lattice, (ii) the formalism of neutron scattering in gas and solid, and (iii) experimental verification of the described models. Some theoretical information and experimental results concerning oxygen and heavy methane are also included.

Neutron scattering in gas is presented using the language of quantum mechanics which describes the system in terms of linear operators in a Hilbert space (an example of this operator technique is described for instance in [81]) instead of the classical dynamical variables which are pure numbers. In particular, one replaces position coordinates q and momentum coordinates p by the operators $\hat{q}$ and $\hat{p}$, respectively. Neutron scattering on the lattice employs the formalism of field quantization, i.e. the operators $\hat{q}$ and $\hat{p}$ are represented by the so-called ladder operators or raising and lowering operators of the harmonic oscillator which serve to raise or lower the number of excitation quanta called phonons [5].

5.1 The Molecule

Molecular energy states arise from the rotation of a molecule as a whole and from the vibration of its constituent atoms relative to one another as well as from changes in its electronic configuration. In the theory of diatomic molecules [82] the total wave function $\Psi(\mathbf{r}_i, \mathbf{R}_k)$ of the molecule in the adiabatic approximation[1] can be written as a product of the nuclear wave function $\Psi_n(\mathbf{R}_k)$ (which depends on the position of nuclei Q) and the electronic wave function $\Psi_e(\mathbf{r}_i, \mathbf{R}_k)$ (which depends on the position of the electrons at arbitrary but fixed nuclear position):

$$\Psi(\mathbf{r}_\mathrm{i}, \mathbf{R}_\mathrm{k}) = \Psi_\mathrm{n}(\mathbf{R}_\mathrm{k}) * \Psi_\mathrm{e}(\mathbf{r}_\mathrm{i}, \mathbf{R}_\mathrm{k}) \tag{5.1}$$

[1] Adiabatic approximation implies that nuclear and electronic motion are independent.

The nuclear wave function $\Psi_n(\mathbf{R}_k)$ can be expressed in the following form:

$$\Psi_{\mathrm{n}}(\mathbf{R}_{\mathrm{k}}) = \Psi_{\mathrm{vib}}\Psi_{\mathrm{rot}} \tag{5.2}$$

The total energy E is the sum of the energy of the rigid molecule in the n-th electronic state and the kinetic energy of the nuclei due to their vibration and rotation:

$$E = E_{\mathrm{el}} + E_{\mathrm{rot}} + E_{\mathrm{vib}} \tag{5.3}$$

The lowest electronic state of a molecule is called the ground state. Energies needed to excite the higher electronic levels are in the range from few eV to 10^2 - 10^3 eV and thus the electronic excitation can be neglected while considering cold neutron scattering [2].

At this point, it is worth noting the difference between deuterium and oxygen molecules. The ground state of the deuterium molecule has a total spin of all electrons $S_{\mathrm{e}} = 0$ while the oxygen molecule is one of the few diatomic molecules that have a total spin $S_{\mathrm{e}} = 1$ in their ground state, which makes the O_2 molecule a magnetic system.

The energy of the vibrational levels of diatomic molecules can be approximated by the energy levels of the harmonic oscillator,

$$E_{\mathrm{vib}} = \left(\upsilon + \frac{1}{2}\right) h\nu_0 \tag{5.4}$$

where υ is the vibrational quantum number and ν_0 is the frequency of vibration. The separation between the vibrational energy levels is typically on the level of 0.1 eV and at room temperature ($E = 3/2kT$), most of the molecules exist in the $\upsilon = 0$ state. The cold neutron energies are not sufficient to excite higher vibrational states, and thus in the further consideration, the vibrational excitation will be neglected.

In the linear rigid rotor model, the rotational energy spectrum of the nuclei of diatomic molecules with the moment of interia:

$$B = mR^2 \tag{5.5}$$

where m is the mass of a nucleus and R is the distance between the two nuclei, is given by:

$$E_{\mathrm{rot}} = E_J = \frac{\hbar^2}{2B} J(J+1) \tag{5.6}$$

where J is the rotational quantum number. While considering the rotational structure of homonuclear molecules such as D_2, one needs to take into account the influence of the nuclear spin on the symmetry of the overall wave function of the molecular state, which is the product of the spatial function (including rotations) and the spin functions [84]. This is due to the spin-statistics theorem by Fierz [85] and Pauli [86] , according to which the overall wave function of fermions (bosons) must be antisymmetric (symmetric) with respect to exchange of the particles. The molecule of deuterium is a compound of two deuterons,

[2] The electronic excitations can be induced by neutron interactions through a direct magnetic interaction or through the disturbance of the molecule resulting from the neutron collision with one of the nuclei of the molecule [83]

nuclear bosons, with nuclear spin 1. The combination of the deuteron spins gives three possibilities for the total nuclear spin $S = 0, 1, 2$. The symmetry requirements divide the states of D_2 into ortho-levels, those possessing even total nuclear spin $S = 0$ and 2 and even rotational angular momenta $J = 0, 2, 4$,..., and para-levels, those with odd quantum numbers ($S = 1; J = 1, 3, 5$, ...). The population of a state, N_J, with the rotation quantum number J follows the Boltzmann distribution:

$$\frac{N_J}{N_0} = (2J+1)\exp\left(-\frac{E_J}{k_B T}\right) \tag{5.7}$$

where

$$E_J = 3.75J(J+1)\text{meV} \tag{5.8}$$

is the energy of the rotational level J [3], the $2J+1$ is the rotational degeneracy factor and T is the temperature of the system.

At room temperature the equilibrium ratio of ortho-D_2 to para-D_2 is 2:1. The transitions between rotational states with even and odd values of J require a change in the relative orientation of the nuclear spins. Transitions of the kind $\Delta J = \pm 1, \pm 3, ..., \Delta S = \pm 1$ are called conversion processes, and the resulting transformation of the two species into each other is called ortho-para conversion [75]. Higher ortho-D_2 concentrations up to 98.5% or even larger can be achieved by using ortho-para converters [74].

5.2 Neutron Scattering by Gas D_2

The description of neutron scattering by an assembly of particles takes into account the molecular energy states (rotations, vibrations), the spin correlations between neutron and molecule, and applies the methods of statistical mechanics to determine how a total fixed amount of energy is distributed among various members of an assembly. The first complete theoretical treatment of thermal neutron scattering by the hydrogen molecule was made by Schwinger and Teller [87] in connection with the experimental determination of the range and spin dependence of the neutron-proton interaction. In their paper they follow the mathematical formulation of the neutron scattering by the hydrogen molecule utilized by Fermi [88] where the short range potentials are replaced by point interactions (represented by the three-dimensional Dirac δ-functions). This work was extended by Hamermesh and Schwinger [89, 90] to the deuterium molecule so that similar information could be obtained about the neutron-deuteron interaction. As a matter of fact, this set of papers led to the conclusion that the neutron spin is 1/2.

The effective potential between a neutron at $\mathbf{r}_n$ and a proton at $\mathbf{r}_p$ using the first Born approximation is:

$$-\frac{4\pi\hbar}{m}\, a\, \delta(\mathbf{r}_n - \mathbf{r}_p) \tag{5.9}$$

where m is the neutron mass and a is the bound scattering length. The further extension of this idea[4] leads to an interaction which differs in the singlet state (proton and neutron

[3] According to the formulas 5.5 and 5.6 and using for the deuterium molecule the values $m = 3.75$ GeV and $R = 0.37$ Å

[4] To include the spin dependence of the neutron-proton interaction.

spins anti-parallel) from that in the triplet state (spins parallel) by quantization i.e. by replacing a in the formula 5.9 by the following operator:

$$\frac{1}{2}\, a_1\, (1+Q) + \frac{1}{2}\, a_0\, (1-Q) \tag{5.10}$$

where a_1 and a_0 are the eigenvalues for the triplet and singlet states, respectively. The operator Q has the eigenvalues +1 for the triplet state and -1 for the singlet state and can be expressed algebraically in terms of $\boldsymbol{\sigma}_n$ and $\boldsymbol{\sigma}_p$, the Pauli matrices of the neutron and the proton:

$$Q = \frac{1}{2}\, (1 + \boldsymbol{\sigma}_n \cdot \boldsymbol{\sigma}_p) \tag{5.11}$$

The formula 5.9 is then replaced by

$$-\frac{\pi\hbar}{m}\, (3\, a_1 + a_0 + (a_1 - a_0)\, \boldsymbol{\sigma}_n \cdot \boldsymbol{\sigma}_p)\, \delta(\boldsymbol{r}_n - \boldsymbol{r}_p) \tag{5.12}$$

Taking into account two protons in the H_2 molecule and representing the proton spin matrices by $\sigma_{\mathbf{1}}$ and $\sigma_{\mathbf{2}}$ respectively, the effective potential for the molecule is given by 5.12:

$$\begin{aligned}\left[-\frac{\pi\hbar}{m}\, (3\, a_1 + a_0 + (a_1 - a_0)\, \boldsymbol{\sigma}_n \cdot \boldsymbol{\sigma}_1)\, \delta(\boldsymbol{r}_n - \boldsymbol{r}_1)\right] + \\ \left[-\frac{\pi\hbar}{m}\, (3\, a_1 + a_0 + (a_1 - a_0)\, \boldsymbol{\sigma}_n \cdot \boldsymbol{\sigma}_2)\, \delta(\boldsymbol{r}_n - \boldsymbol{r}_2)\right]\end{aligned} \tag{5.13}$$

Expression 5.13 may be rewritten in two parts; a symmetrical part which is responsible for the transitions were the nucleus spin doesn't change i.e. ortho→ortho and para→ para-transitions, and an antisymmetric part that induces spin changes, that is ortho→para and para→ortho-transitions:

$$\begin{aligned}\left[-\frac{\pi\hbar}{m}\, (3\, a_1 + a_0 + (a_1 - a_0)\, \boldsymbol{\sigma}_n \cdot \boldsymbol{S}) \times (\delta(\boldsymbol{r}_n - \boldsymbol{r}_1) + \delta(\boldsymbol{r}_n - \boldsymbol{r}_2))\right] + \\ \left[-\frac{\pi\hbar}{m}\, (a_1 - a_0)\, \boldsymbol{\sigma}_n \cdot (\boldsymbol{\sigma}_1 - \boldsymbol{\sigma}_2) \times (\delta(\boldsymbol{r}_n - \boldsymbol{r}_1) - \delta(\boldsymbol{r}_n - \boldsymbol{r}_2))\right]\end{aligned} \tag{5.14}$$

where

$$\mathbf{S} = \frac{1}{2}(\boldsymbol{\sigma}_1 + \boldsymbol{\sigma}_2) \tag{5.15}$$

represents the total spin angular momentum of the hydrogen molecule.

In analogy to 5.14 the interaction between neutron and the two deuterons in the D_2 molecule is expressed by:

$$\begin{aligned}U = \left[-\frac{\pi\hbar}{m}\, (2\, a_{3/2} + a_{1/2} + (a_{3/2} - a_{1/2})\, \boldsymbol{\sigma}_n \cdot \boldsymbol{S}) \times (\delta(\boldsymbol{r}_n - \boldsymbol{r}_1) + \delta(\boldsymbol{r}_n - \boldsymbol{r}_2))\right] + \\ \left[-\frac{\pi\hbar}{m}\, (a_{3/2} - a_{1/2})\, \boldsymbol{\sigma}_n \cdot (\boldsymbol{S}_1 - \boldsymbol{S}_2) \times (\delta(\boldsymbol{r}_n - \boldsymbol{r}_1) - \delta(\boldsymbol{r}_n - \boldsymbol{r}_2))\right]\end{aligned} \tag{5.16}$$

where now

$$\boldsymbol{S} = \boldsymbol{S}_1 + \boldsymbol{S}_2 \tag{5.17}$$

represents the total spin of the deuterium molecule and $a_{S\pm1/2}$ are the amplitudes of the scattered waves for the two total spin states of the neutron-deuteron system.

We consider a collision between a neutron and a molecule in which the neutron momentum changes from $\boldsymbol{p}_0$ to $\boldsymbol{p}$, while the molecule simultaneously undergoes a transition between the initial state, specified by the momentum $-\boldsymbol{p}_0$ and by the vibrational, rotational, and spin quantum numbers υ, J, S, and the final state characterized by $-\boldsymbol{p}, \upsilon', J', S'$. The wave function of the initial ψ_{i} and final state ψ_{f} for a large box of volume V are:

$$\psi_i = \frac{1}{\sqrt{V}} \exp\left(\frac{i}{\hbar}\,\boldsymbol{p}_0 \cdot \boldsymbol{r}_n\right) \chi_m \;\; \frac{1}{\sqrt{V}} \exp\left(-\frac{i}{\hbar}\,\boldsymbol{p}_0 \cdot \frac{(\boldsymbol{r}_1 + \boldsymbol{r}_2)}{2}\right) \cdot \Phi_{\,\upsilon,J,m_J}\,(\boldsymbol{r}_1 - \boldsymbol{r}_2)\;\chi_{\,S,m_S} \tag{5.18}$$

$$\psi_f = \frac{1}{\sqrt{V}} \exp\left(\frac{i}{\hbar}\,\boldsymbol{p} \cdot \boldsymbol{r}_n\right) \chi_{m'} \;\; \frac{1}{\sqrt{V}} \exp\left(-\frac{i}{\hbar}\,\boldsymbol{p} \cdot \frac{(\boldsymbol{r}_1 + \boldsymbol{r}_2)}{2}\right) \cdot \Phi_{\,\upsilon',J',m'_J}\,(\boldsymbol{r}_1 - \boldsymbol{r}_2)\;\chi_{\,S',m'_S} \tag{5.19}$$

where $\frac{1}{\sqrt{V}} \exp\left(\frac{i}{\hbar}\,\boldsymbol{p}_0 \cdot \boldsymbol{r}_n\right)$ is the wave function of a free neutron with momentum $\boldsymbol{p}_0$, χ_m is the eigenfunction of the z-component of the neutron spin corresponding to the eigenvalue m, $\frac{1}{\sqrt{V}} \exp\left(-\frac{i}{\hbar}\,\boldsymbol{p}_0 \cdot \frac{(\boldsymbol{r}_1 + \boldsymbol{r}_2)}{2}\right)$ is the wave function that describes the motion of the center of gravity of the deuterium molecule with momentum $-\,\boldsymbol{p}_0$, $\Phi_{\,\upsilon,J,m_J}(\boldsymbol{r}_1 - \boldsymbol{r}_2)$ is the wave function of the relative motion of the two deuterons in a state with vibrational quantum number υ, rotational quantum number J and magnetic quantum number m_J and $\chi_{\,S,m_S}$ is the eigenfunction of the deuteron spins corresponding to a resultant spin angular momentum S and an eigenvalue of the z-component of the total spin equal to m_S . The transition probability from the initial state to the final state is given by the Fermi golden rule:

$$\frac{2\pi}{\hbar} \mid < \psi_{\mathrm{f}} \mid U \mid \psi_{\mathrm{i}} > \mid^2 \rho_E \tag{5.20}$$

where U refers to 5.16 and ρ_E represents the number of neutron momentum states per unit range of the total final energy. The total final energy E is the sum of the neutron energy and the internal energy of the molecule $E_{J,\upsilon}$ and taking into account the energy conservation law is equal to:

$$E = \frac{5}{8M}(\boldsymbol{p}_0)^2 + E_{\,J,\upsilon} = \frac{5}{8M}\boldsymbol{p}^2 + E_{\,J',\upsilon'} \tag{5.21}$$

where $\boldsymbol{p}_0$ is the momentum in the CM system and is related to $\boldsymbol{p}_0^L$, the initial neutron momentum in the L system (in which the molecule is initially at rest), by:

$$\boldsymbol{p}_0 = \frac{4}{5}\boldsymbol{p}_0^L \tag{5.22}$$

The density of final states is given by:

$$\rho_E = \frac{V}{8\pi^3\hbar^3}\frac{d\boldsymbol{p}}{dE} \tag{5.23}$$

writing the element $d\boldsymbol{p}$ in spherical coordinates:

$$d\boldsymbol{p} = p^2 d\Omega dp \tag{5.24}$$

and

$$dE = \frac{5p}{4M}dp \tag{5.25}$$

so that

$$\rho_E = \frac{VMp}{10\pi^3\hbar^3}d\Omega \tag{5.26}$$

Combining the formulae, including the summation over all values m', m'_J, m'_S and average with respect to m, m_J, m_S the transition probability 5.20 becomes:

$$\frac{1}{2(2S+1)(2J+1)}\sum_{m',m'_J,m'_S}\sum_{m,m_J,m_S} |<\psi_{\mathrm{f}}\mid U\mid\psi_{\mathrm{i}}>|^2\frac{VMp}{10\pi^2\hbar^4} \tag{5.27}$$

The differential cross section for scattering of a neutron through an angle Θ into the solid angle $d\Omega$ with excitation of the molecule from the state J, υ, S to the state J', υ', S' in the CM system, is obtained by dividing 5.27 by the incident flux of neutrons relative to the deuterium molecule $(5p_0/4MV)$:

$$\begin{aligned}\sigma_{\,J',\upsilon',S';J,\upsilon,S}(\Theta)d\Omega = \frac{16}{25}\,\frac{p}{p_0}\,\frac{1}{2(2S+1)(2J+1)}\\ \cdot\sum_{m',m'_J,m'_S}\sum_{m,m_J,m_S}\left|<\psi_{\mathrm{f}}\mid\left(\frac{VM}{2\pi\hbar^2}\right)U\mid\psi_{\mathrm{i}}>\right|^2\end{aligned} \tag{5.28}$$

The formula 5.28 can be divided into two parts; in the first part we consider the transitions in which the molecular spin is unchanged i.e. $S = S'$:

$$\begin{aligned}\sigma_{\,J',\upsilon',S';J,\upsilon,S}(\Theta)d\Omega = \frac{16}{25}\,\frac{p}{p_0}\,\left[(2\,a_{3/2}+a_{1/2})^2+\frac{1}{4}\,(a_{3/2}-a_{1/2})^2\,S(S+1)\right]\\ \cdot\frac{1}{2J+1}\sum_{m_J,m'_J}\left|\int\cos\left(\frac{(\boldsymbol{p}_0-\boldsymbol{p})\cdot\boldsymbol{r}}{2\hbar}\right)\Phi^*_{\upsilon',J',m'_J}(\boldsymbol{r})\Phi_{\,\upsilon,J,m_J}(\boldsymbol{r})\,d\tau\right|^2 d\Omega\end{aligned} \tag{5.29}$$

the second part takes care of the transitions in which the molecular spin changes:

$$\begin{aligned}\sum_{S'\neq S}\sigma_{\,J',\upsilon',S';J,\upsilon,S}(\Theta)d\Omega = \frac{16}{25}\,\frac{p}{p_0}(a_{3/2}-a_{1/2})^2\,\frac{8-S(S+1)}{4}\\ \frac{1}{2J+1}\sum_{m_J,m'_J}\left|\int\sin\left(\frac{(\boldsymbol{p}_0-\boldsymbol{p})\cdot\boldsymbol{r}}{2\hbar}\right)\Phi^*_{\upsilon',J',m'_J}(\boldsymbol{r})\Phi_{\,\upsilon,J,m_J}(\boldsymbol{r})\,d\tau\right|^2 d\Omega\end{aligned} \tag{5.30}$$

It is interesting to note that since $\Phi_{v,J,m_J}(-\boldsymbol{r}) = (-1)^J \Phi_{v,J,m_J}(\boldsymbol{r})$, equation 5.29 gives a non vanishing transition probability only if J and J' are both even or both odd, while equation 5.30 implies the even-odd and odd-even transitions in the rotational number J.

In the last step, the evaluation of the cross section formula for neutron and molecular velocities of comparable magnitudes takes into account not a particular molecule but the whole assembly of molecules and employs the methods of statistical mechanics. The target molecules are in general in thermal equilibrium at a given temperature T rather than in predetermined initial states. The quantity desired for the prediction of experimental cross sections - the effective scattering cross section for a neutron velocity v, $\bar{\sigma}(v)$, is related to the true cross section, $\sigma(v)$, by:

$$v\sigma(v) = \int |\boldsymbol{v} - \boldsymbol{u}|\sigma(|\boldsymbol{v} - \boldsymbol{u}|)P(\boldsymbol{u})(d\boldsymbol{u}) = \int w\sigma(w)P(\boldsymbol{v} + \boldsymbol{w})(d\boldsymbol{w}) \tag{5.31}$$

where $P(\boldsymbol{u})$ is the velocity distribution function of the target molecules. It should be noted that equation 5.31 is only approximate as the translation motion needs to be incorporated within the states and leads to appropriately modified versions of equations 2.17 and 2.18; this calculation has been carried out by Young and Koppel [91, 92] for gas, but in the energy region of interest here (see Figure 5.1) the difference is negligible. For gas, the velocity distribution function $P(\boldsymbol{u})$ is given by the Maxwell-Boltzmann distribution law 3.10 and equation 5.31 becomes:

$$\bar{\sigma}(v) = \frac{2}{v^2}\left(\frac{2M}{\pi k_B T}\right)^{\frac{1}{2}} \exp\left(-\frac{2Mv^2}{k_B T}\right) \int_0^\infty \exp\left(-\frac{2Mw^2}{k_B T}\right) \sinh\left(\frac{4Mvw}{k_B T}\right) w^2\sigma(w)dw \tag{5.32}$$

At this point is it worth discussing the effect of the motion of the target molecules with respect to the different phases of matter as presented by Vineyard [93]. It is particularly interesting since the aim of his work was to discover "simple formulas which approximate the cross-sections reasonably well and depend on a small number of parameters having physical meaning". As the folding of $\sigma(v)$ is made with the Maxwell-Boltzmann function, the result 5.32 is limited to scattering by gas molecules. However, according to Vineyard, things may not be so different for liquid and solid deuterium. Starting from the Van Hove [94] correlation functions and proceeding in a classical manner Vineyard derived the following relationships for the differential scattering cross sections (symbols are: $\boldsymbol{k}_0$ & $\boldsymbol{k}$ for the incident and final neutron wave vector, E_0 & E for the incident and final energies, $\hbar\omega = E_0 - E$ for the energy loss by the neutron, a_{coh} & a_{inc} for the scattering lengths and $\kappa = \sqrt{k_0^2 + k^2 - 2kk_0\cos\varphi}$ for the momentum transfer)

$$\frac{d^2\sigma_{\text{coh}}}{d\Omega dE} = \frac{a_{\text{coh}}\, k}{h\, k_0}\, \Gamma_{\text{s}}(\boldsymbol{\kappa}, \omega)[1 + \gamma(\boldsymbol{\kappa})] \tag{5.33}$$

$$\frac{d^2\sigma_{\text{inc}}}{d\Omega dE} = \frac{a_{\text{inc}}\, k}{h\, k_0}\, \Gamma_{\text{s}}(\boldsymbol{\kappa}, \omega) \tag{5.34}$$

where

$$\Gamma_{\mathrm{s}}(\boldsymbol{\kappa},\omega) = \int\int G_{\mathrm{s}}(\boldsymbol{r},t)\exp\left[i(\boldsymbol{\kappa}\cdot\boldsymbol{r}-\omega t)\right]d\boldsymbol{r}\,dt \tag{5.35}$$

is the double Fourier transform in position and time of the self correlation function, $G_s(\boldsymbol{r},t)$ which is a part of the Van Hove generalized pair correlation function $G(\boldsymbol{r},t)$ [5] and describes the probability of finding an atom at time t given the same atom was at the origin at $t=0$, i.e. the wandering of an atom away from an arbitrary initial position. $\Gamma_s(\boldsymbol{\kappa},\omega)$ describes thus the spread of scattered energies caused by the motion of atoms. The form factor present in the coherent cross section, $[1+\gamma(\boldsymbol{\kappa})]$, where

$$\gamma(\boldsymbol{\kappa}) = \int (g(\boldsymbol{r})-g_0)\exp\left(i\boldsymbol{\kappa}\cdot\boldsymbol{r}\right)d\boldsymbol{r} \tag{5.36}$$

describes the interference effects arising from the correlations in atomic positions.The examples of G_s for different systems as given by Vineyard are shown in the table 5.1.

Table 5.1: The examples for $G_s(\boldsymbol{r},0)$ as given by Vineyard [93].

Model	$G_s(\boldsymbol{r},t)$
Perfect gas	$\dfrac{1}{(\sqrt{\pi}v_0\lvert t\rvert)^3}\exp\left(-\dfrac{\boldsymbol{r}^2}{(v_0t)^2}\right)$
Harmonic oscillator[a]	$\left[\dfrac{\omega_1^2}{2\pi v_0^2(1-\cos(\omega_1 t))}\right]^{\frac{3}{2}}\exp\left(\dfrac{-\omega_1^2\boldsymbol{r}^2}{2v_0^2(1-\cos(\omega_1 t))}\right)$
Lattice[b]	$\left[\pi w^2(t)\right]^{\frac{3}{2}}\exp\left(\dfrac{-\boldsymbol{r}^2}{w^2(t)}\right)$
Diffusing atom[c]	$\left[4\pi Dt\right]^{\frac{3}{2}}\exp\left(\dfrac{-\boldsymbol{r}^2}{4Dt}\right)$

[a] Here ω_1 represents the oscillator frequency.

[b] For the Debye model $w^2(t) = [12kT/(M\omega_D)^2][1-\sin(\omega_D t)/(\omega_D t)]$ where ω_D is a Debye frequency.

[c] Here D is the coefficient of self-diffusion.

[5] In case of systems composed of distinguishable particles the G function splits into a part G_s describing the correlations between positions of one and the same particle at different times, and a part G_d referring to pairs of distinct particles, for t = 0, $G_s(\boldsymbol{r},0)=\delta(\boldsymbol{r})$ and $G_d(\boldsymbol{r},0)=g(\boldsymbol{r})$ where $g(\boldsymbol{r})$ is a conventional pair distribution function which describes the average density distribution.

The experimental verification of the described Hamermesh-Schwinger (HS) and Young-Koppel (YK) models was done by our UCN collaboration and is published [95]. The measurements have been performed using cold neutrons at the SANS-I instrument [96] of the SINQ facility at PSI and with VCN and UCN at the PF-2 instrument [97] of the Institute Laue-Langevin (ILL). The total cross sections have been measured using the transmission technique (see section 4.3.2) and calculated with the help of:

$$\sigma = \frac{ln(N_0/N_1)}{\rho d} \tag{5.37}$$

where N_0 and N_1 are the transmitted intensities for the empty and full sample cells, ρ is the density and d is the thickness of the sample cell. In Figure 5.1 the results of the measurements with ortho-D_2 are shown together with the cross section calculated with the YK and HS models. Both models are equivalent over the displayed energy region and the agreement between the data and theory is remarkable. The calculations are made for the 'self' scattering i.e. refering to a single D_2 molecule, since for gaseous D_2 the influence of the interference of neutron waves scattered from different molecules is very small. However, for liquid and solid D_2, the interference effects (see Eq. 5.36 and Eq. 5.33) become important as it can be seen in the measured cross sections presented in Figure 5.2. In the case of a solid, the interference effects manifest as a coherent elastic Bragg scattering, for a liquid, this is somewhat similar due to the rather well defined correlations between neighbouring molecules.

In addition, it is worth to remark that the coherent a_{coh} and incoherent a_{inc} scattering lengths for deuterium atom are of the same sign and the same order of magnitude (a_{coh} = 6.671 fm and a_{inc} = 4.04 fm), which makes deuterium different, in this manner, from hydrogen, which is mainly an incoherent scatterer with a_{coh} = -3.7406 fm and a_{inc} = 25.274 fm. The scattering in deuterium is largely coherent and the interference effects play an important role in scattering.

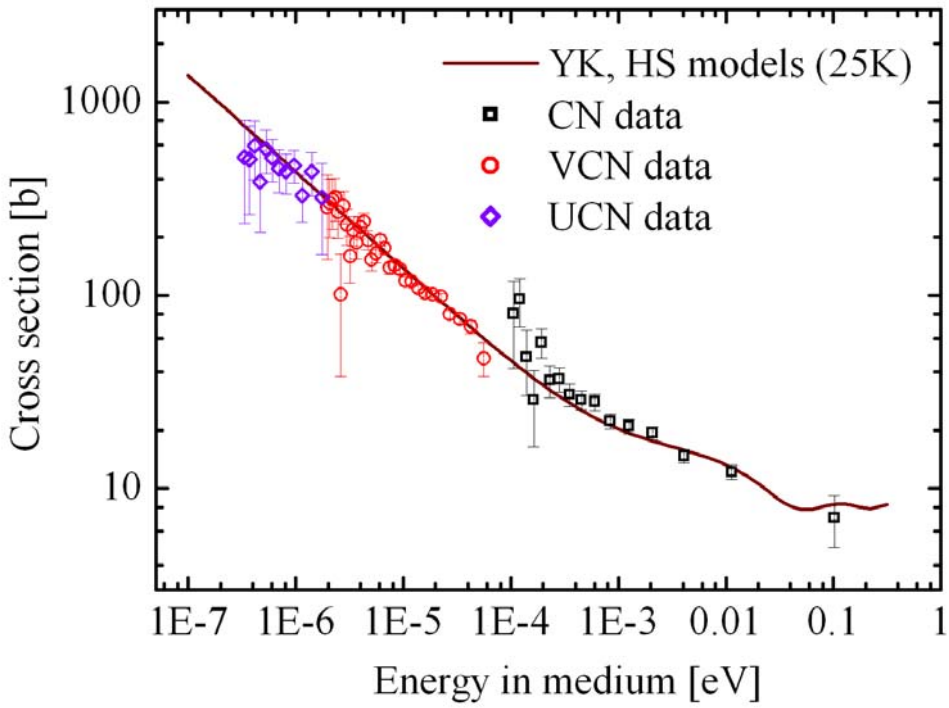

Figure 5.1: Measured total neutron scattering cross sections per molecule as a function of the in-medium neutron energy for gaseous D_2 at 25 K. The Hamermesh and Schwinger and the Young and Koppel models reproduce the measured cross sections of D_2 in the gas phase. The bump in the cross section around the energy of 10 meV is due to excitation of the J=1 rotational level of D_2 molecule.

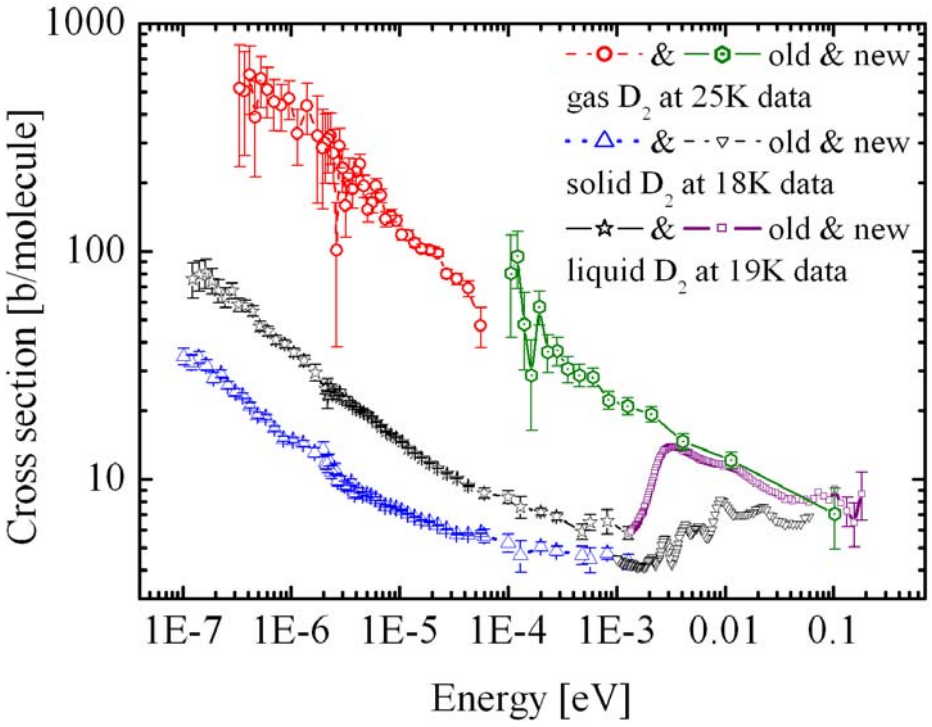

Figure 5.2: Measured total neutron scattering cross sections per molecule as a function of the in-medium neutron energy for gaseous (25K), liquid (19K) and solid (18K) D_2. The previously published data (see [1, 95]) is completed with the new data coming from the transmission TOF measurements with CN. Comparing the different slopes of cross sections of gaseous, liquid, and solid D_2, one can notice a rapid increase in the cross section for solid and liquid D_2 above the Bragg cut-off energy due to the interference effects arising from the correlation in molecular positions, while for gas no interference effects are visible at this energy.

5.3 The Crystal Structure

The crystal structure is a periodic arrangement of atoms and its mathematical description is based on a concept of a lattice which is defined as an array of points in space. The building block i.e. the smallest repeating volume of the lattice is called the unit cell and it is set by the three lattice constants a_1, a_2, a_3 (the lengths of the basis vectors $\boldsymbol{a}_1$, $\boldsymbol{a}_2$, $\boldsymbol{a}_3$) and by the three angles α, β, γ, which separate these vectors from one another. The lattice points are located at the corners of the unit cell and are shared with seven other unit cells, and since each cell has eight corners, there is only one lattice point per unit cell (so-called *primitive* unit cells). For some crystal lattices the unit cell can have two or more lattice points, then the additional points will be located at positions other than the corners of the cell; for example the unit cell of the hexagonal close-packed (hcp) lattice has two lattice points per unit cell at site[6] (0,0,0) and $(\frac{2}{3},\frac{1}{3},\frac{1}{2})$. The positions of atoms are given in terms of coordinates which describe fractions of the lattice constants; the atom in the center of an unit cell has coordinates $(\frac{1}{2},\frac{1}{2},\frac{1}{2})$.

The crystal lattice can be described in relation to its symmetry properties. Full consideration of the possible symmetries for the lattice leads to seven crystal systems: triclinic, monoclinic, orthorhombic, tetragonal, cubic, trigonal, and hexagonal, determined by the lattice constants and the angles. More details about the classification of the crystal structures can be found [98]. The information about the crystal structure of solid D_2, O_2 and CD_4 are collected in the table 5.2.

Another important concept connected with crystal structure is a lattice plane. The position and orientation of a crystal plane is set by giving the coordinates of three non-collinear atoms lying in the plane and it is specified by Miller indexes (hkl) [98]. The indexes hkl denote a single plane or a set of parellel planes and are the reciprocals of the intercepts on the three basis axes in terms of the lattice constants; if a plane intersects[7] the $\boldsymbol{a}_1$, $\boldsymbol{a}_2$ and $\boldsymbol{a}_3$ axes at distances x_1, x_2 and x_3 respectively, then the Miller indexes of that plane are given by :

$$h = C\,\frac{a_1}{x_1} \qquad\qquad k = C\,\frac{a_2}{x_2} \qquad\qquad l = C\,\frac{a_3}{x_3} \tag{5.38}$$

where C is a scalar which clears the indexes off fractions or common factors.

The interaction of radiation of a wavelength λ with the crystal structure results in the elastic coherent scattering, i.e. Bragg scattering. The Bragg law says that the constructive interference of the radiation reflected from parallel planes of atoms separeted by a distance d_{hkl} will occur when the path difference is an integral number n of wavelengths. The condition for constructive reflection is :

$$2d_{hkl}\sin\Theta = n\lambda \tag{5.39}$$

[6] In units of the basis vectors.

[7] If a plane is parallel to the axis then the corresponding index is zero.

Table 5.2: Crystal structures and lattice parameters for solid D_2, CD_4 and O_2. (at equilibrium vapour pressure)

Material	Lattice type	Lattice parameters
D_2 [a]	hcp	$a_1 = a_2 \neq a_3$ $\alpha = \beta = 90°$, $\gamma = 120°$ $a_1 = 3.607$ Å$a_3 = 5.81$ Å
CD_4 I phase [b] 27.1 K < T < 89.9 K	fcc	$a_1 = a_2 = a_3$ $\alpha = \beta = \gamma = 90°$ $a_1 = 5.925$ Å
CD_4 II phase [c] 22.1 K < T < 27.1 K	fcc	$a_1 = a_2 = a_3$ $\alpha = \beta = \gamma = 90°$ $a_1 = 5.829$ Å
CD_4 III phase [d] T < 22.1 K	tetragonal	$a_1 = a_2 \neq a_3$ $\alpha = \beta = \gamma = 90°$ $a_1 = 5.768$ Å$a_3 = 5.861$ Å
O_2 γ phase [e] 43.8 K < T < 54.4 K	cubic	$a_1 = a_2 = a_3$ $\alpha = \beta = \gamma = 90°$ $a_1 = 6.732$ Å
O_2 β phase [c] 23.9 K < T < 43.8 K	rhombohedral	$a_1 = a_2 \neq a_3$ $\alpha = \beta = 90°$ $\gamma = 120°$ $a_1 = 3.274$ Å, $a_3 = 11.293$ Å
O_2 α phase [d] T < 23.9 K	monoclinic[f]	$a_1 \neq a_2 \neq a_3$ $\alpha = \gamma = 90° \neq \beta$ $a_1 = 5.375$ Å, $a_2 = 3.434$ Å, $a_3 = 4.242$ Å $\beta = 117.76°$

[a] [99]
[b] at 65K [100]
[c] at 25K [100]
[d] at 8K [100]
[e] at 45K [100]
[f] Oxygen in α phase has an ordered arrangement of axes and magnetic moments of molecules which results in a quazi two dimentional antiferromagnetic.

The scattering angle Θ depends on the spacing of the lattice planes which can be expressed with reference to the reciprocal lattice vector $\boldsymbol{K}_{hkl}$:

$$d_{hkl} = \frac{2\pi}{|\boldsymbol{K}_{hkl}|} \tag{5.40}$$

The reciprocal lattice is a special coordinate system commonly used in description of radiation scattering from a crystal lattice. For a lattice represented by the vectors $\boldsymbol{a}_1$, $\boldsymbol{a}_2$, and $\boldsymbol{a}_3$ the corresponding reciprocal basis vectors $\boldsymbol{b}_1$, $\boldsymbol{b}_2$, and $\boldsymbol{b}_3$ fullfill the relation:

$$\boldsymbol{a}_\mathrm{i}\boldsymbol{b}_\mathrm{j} = \delta_\mathrm{ij} \tag{5.41}$$

where δ_{ij} is the Kronecker delta, $\boldsymbol{b}_\mathrm{j}$ and are given by:

$$\boldsymbol{b}_1 = \frac{\boldsymbol{a}_2 \times \boldsymbol{a}_3}{V} \tag{5.42}$$

$$\boldsymbol{b}_2 = \frac{\boldsymbol{a}_1 \times \boldsymbol{a}_3}{V} \tag{5.43}$$

$$\boldsymbol{b}_3 = \frac{\boldsymbol{a}_1 \times \boldsymbol{a}_2}{V} \tag{5.44}$$

$$\tag{5.45}$$

where $V = \boldsymbol{a}_1 \cdot (\boldsymbol{a}_2 \times \boldsymbol{a}_3)$ is the volume of the unit cell in the real lattice. The reciprocal lattice vector from the origin to the point (h,k,l) of the reciprocal lattice is normal to the (hkl) plane of the real crystal lattice and it is given by:

$$\boldsymbol{K}_{hkl} = h\boldsymbol{b}_1 + k\boldsymbol{b}_2 + l\boldsymbol{b}_3 \tag{5.46}$$

5.4 Elastic Scattering of a Crystal Lattice

The interaction between a neutron of a wavelength λ and the crystal structure leads to coherent elastic scattering and it becomes particulary important for neutrons with energies above the Bragg cut-off, which corresponds to the condition:

$$\lambda \leq 2d_{hkl} \tag{5.47}$$

where d_{hkl} is the largest lattice spacing occuring in the crystal given by Eq. 5.40 and depends on the lattice constants. The coherent elastic cross section per unit cell of a polycrystalline sample, which is proportional to the total number of neutrons scattered coherently in all directions, is given by:

$$\sigma_{\mathrm{el,coh}} = \frac{N_{\mathrm{c}}\,\lambda^2}{2} \sum_{\substack{hkl \\ d_{hkl} \geq \lambda/2}} F_{hkl}^2 d_{hkl} \tag{5.48}$$

where N_c is the number of unit cells per unit volume and F_{hkl} is the nuclear unit cell structure factor:

$$F_{hkl} = \sum_d b_{\mathrm{coh}_d} \exp\left(i\boldsymbol{d}\cdot\boldsymbol{K}_{hkl}\right) \tag{5.49}$$

where $\boldsymbol{d}$ is the position vector of an atom, b_{coh_d} the coherent scattering amplitude for the atom at position d which determines the intensity of the Bragg reflections. $\boldsymbol{K}_{hkl}$ is the reciprocal lattice vector (Eq. 5.46). The summation in Eq. 5.48 is taken over all planes (hkl) which are capable of giving Bragg reflection for the given neutron wavelength, since the microcrystals which constitute the polycrystal are oriented at random to collectively produce all possible orientations. If, however, there is a specified axis of crystal growth, the microcrystals might be oriented in a direction which reduced the number of planes capable of giving Bragg reflection. As an example, the calulation of the coherent elastic cross section has been made for the solid D_2 hcp lattice structure (see Tab. 5.2) with two deuterium molecules per unit cell. For a crystal with the hcp structure the structure function, F_{hkl} is given by:

$$F_{hkl} = 2b_{\mathrm{coh}_d} \cos\left(\frac{\pi}{6}(4h+2k+3l)\right) \tag{5.50}$$

and the separation between the hkl planes is:

$$d_{hkl} = \sqrt{\left(\frac{3a^2c^2}{4c^2(h^2+hk+k^2)+3l^2a^2}\right)} \tag{5.51}$$

The summation in Eq. 5.48 was taken over (i) all possible planes, (ii) planes parallel to the xy crystal plane (h=k=0), (iii) planes parallel to the z axis (l=0). For the purpose of comparision between the calculations and the measured total cross sections, the total elastic cross section has to be taken into account:

$$\sigma_{\mathrm{el,tot}} = \sigma_{\mathrm{el,coh}} + \sigma_{\mathrm{el,inc}} \tag{5.52}$$

where $\sigma_{\mathrm{el,inc}}$ is the incoherent elastic cross section given by:

$$\sigma_{\mathrm{el,inc}} = 4\pi \sum_d b^2_{\mathrm{inc}_d} \tag{5.53}$$

where b_{inc_d} the incoherent scattering amplitude for the atom at position d.
A similar calculation has been done for the solid CD_4 fcc lattice structure (see Tab. 5.2) with four CD_4 molecules per unit cell. The structure function F_{hkl} for the fcc lattice is given by:

$$F_{hkl} = b_{\mathrm{coh}_d}(1 + (-1)^{h+k} + (-1)^{k+l} + (-1)^{h+l}) \tag{5.54}$$

and d_{hkl}:

$$d_{hkl} = \frac{a}{\sqrt{h^2 + k^2 + l^2}} \tag{5.55}$$

In the Figures 5.3 and 5.7 the calculated values together with the experimental data are shown. In case of solid oxygen only the experimental data are shown in Figure 5.11.

The calculations presented here do not include many interesting phenomena. The effect of the thermal motion of the molecules in the crystal given by the Debye-Waller factor is not properly considered, however, the influence of the Debye-Waller factor on the calculated values is shown in the Figure 5.12 and discussed briefly. The inelastic scattering in the region of Bragg scattering is also not shown. Those two effects (i.e Debye-Waller factor and inleastic scattering), although they usually compensate each other, certainly should be included in the proper theoretical model of neutron scattering by the lattice in the Bragg region. One possible way of modeling the data in the region of Bragg scattering, decribed by Atchison [101], takes into account the Hamermesh and Schwinger formalism with the coherent cross section modified with the structure function S(Q)(measured for liquid D_2 by Zoppi et al. [102] and translated into molecular liquid structure function $[1+\gamma(\boldsymbol{\kappa})]$ of Vineyard or the $S_m(Q)$ of Granada et al. [103]) and folded with a Gauss fuction to represent the thermal motion of the target molecules.

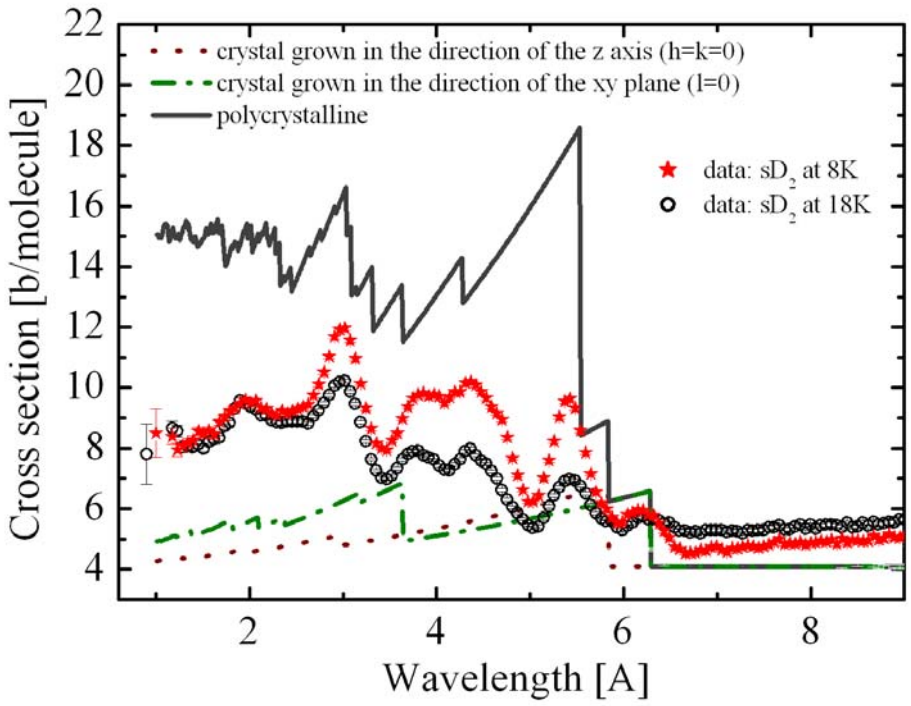

Figure 5.3: Measured total neutron scattering cross sections in the region of Bragg scattering as a function of the neutron wavelength for solid D_2 at 18 (circles) and 8 K (stars). The solid, dashed, and dotted lines show the theoretical elastic cross section (the sum of coherent and incoherent) calculated by taking into account solid D_2 crystal lattice parameters. The solid line represents the total elastic cross section for a polycrystalline structure, while the dashed and dotted ones show the elastic cross section for crystals grown in specific directions. The comparison between the experimental data and theoretical cross sections should be treated qualitatively i.e. in terms of understanding the structure of the deuterium crystals grown in the experiment. The measured cross sections are between the calculated cross sections for polycrystalline and for the oriented crystal structure suggesting that the measured sample was in the state between the polycrystal and single crystal. An additional hint comes from the comparison of the data at 18K and 8K (see also Figure 5.4); higher cross sections at 8K indicate a more random polycrystalline structure, which is in agreement with the optical observation of the crystal as well as with the Raman spectra (see Figure 5.5).

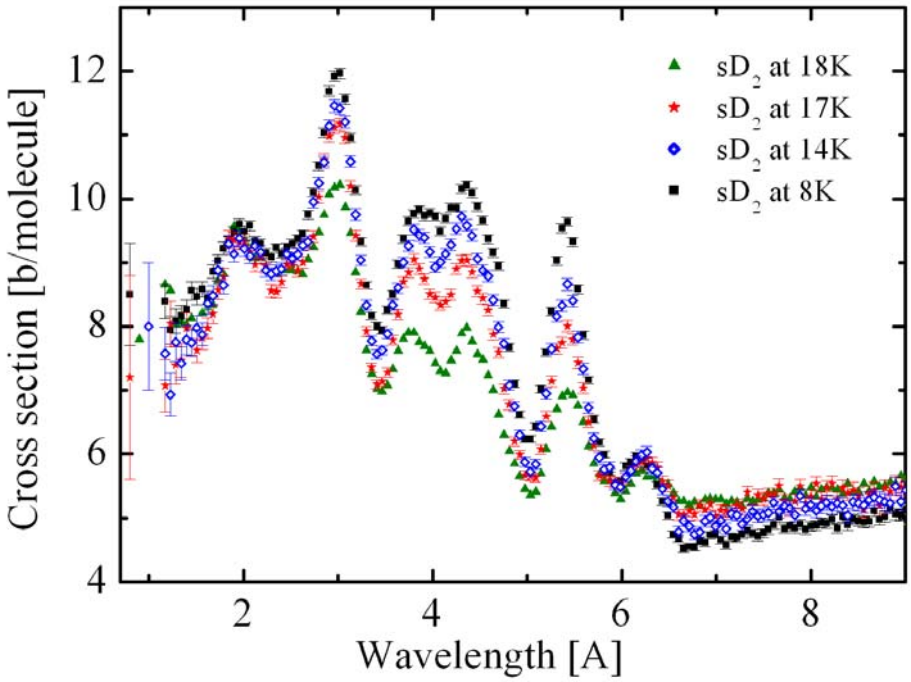

Figure 5.4: Measured total neutron scattering cross sections in the region of Bragg scattering as a function of the neutron wavelength for solid D_2 at 18K (triangles), 17K (stars), 14K (diamonds) and 8 K (squares). In the Bragg region the cross section grows with lowering the temperature of the sD_2 crystal, while it decreases for longer wavelength.

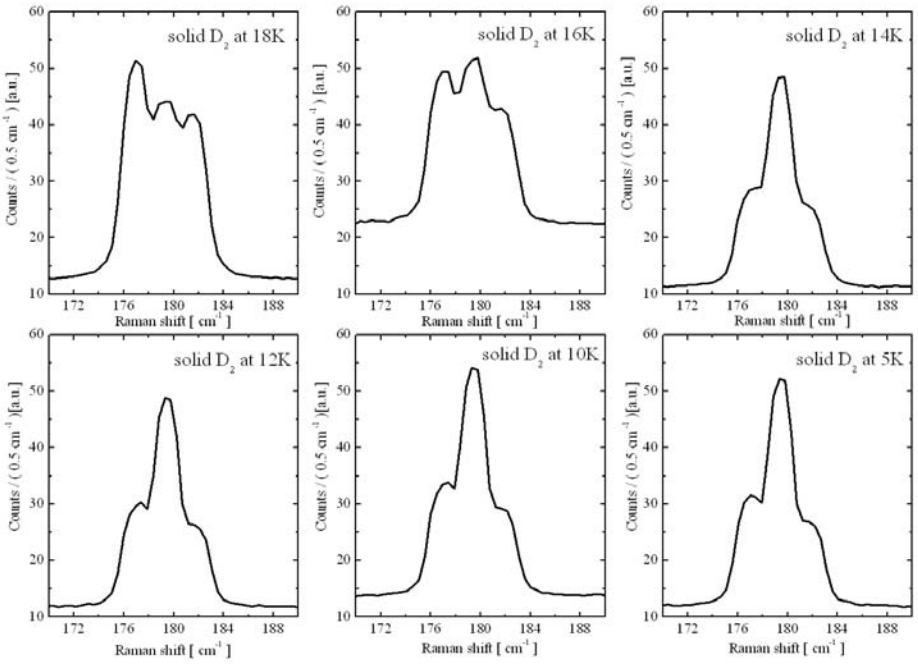

Figure 5.5: The rotational Raman spectra of the J=0 to J=2 transition, S_0 (0) line, in solid deuterium at different temperatures for the same sD_2 crystal. The focus of the light has been kept at the same position. The splitting of the $S_0(0)$ line comes from the fact that the J=2 level form three energy bands belonging to m = ± 1 (α), m = ± 2 (β), m = ± 0 (γ). The line intensity ratios within the multiplet contain information about the relative orientation of the crystal (or crystallites) with respect to the direction of the Raman collector. With the change of temperature, the line intensity ratios change, indicating that the relative orientations of the crystallites is changing in the sample. This might be an explanation for the different intensities of the Bragg scattering at different crystal temparatures. It is important to note that moving the focus of the laser light along the dimensions of the crystal also influences the line intensity ratios, but not as much as changing the temperature. The change due to temperature is reversible, i.e. by keeping the laser focused at one point, then cooling down from 18K to 5K, and afterwards warming up back to 18K, one sees the same line intensity ratio at 18K.

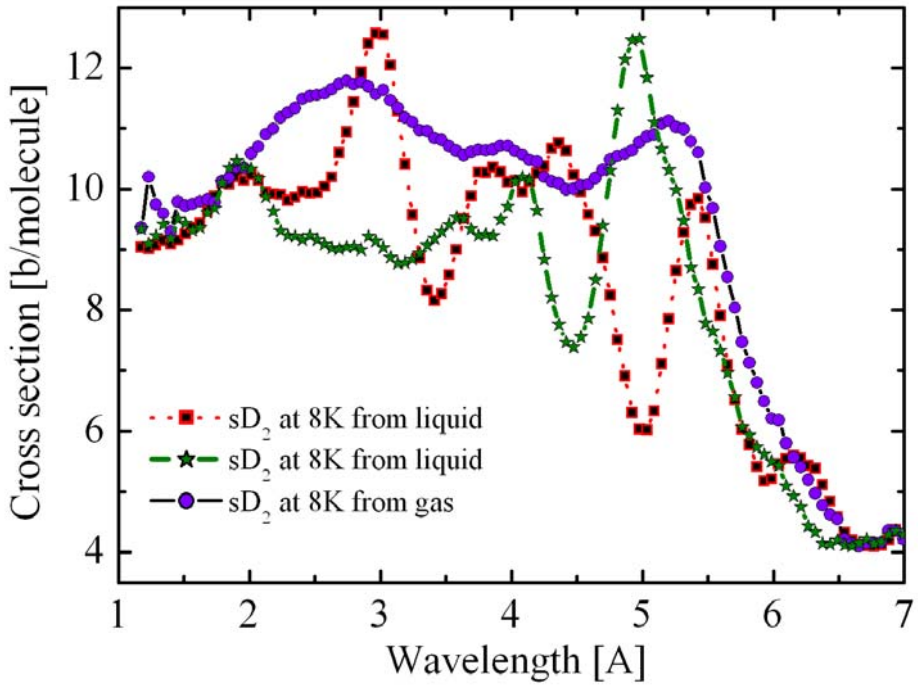

Figure 5.6: Comparison of the measured total neutron scattering cross sections between three different sD_2 crystals at 8K. Two crystals were frozen from the liquid phase at the same conditions (stars and squares) and one was grown from the gas phase (circles). The cross sections in the Bragg region differ significantly while they are the same in the region above the Bragg cut-off wavelength. This indicates that CN scattering (Bragg region) is very sensitive to the specific crystal structure. Those data also show that it is difficult to grow identical crystals i.e. with the same Bragg scattering pattern, even under very similar conditions. The average total cross section, however, is not particularly sensitive to the crystal structure.

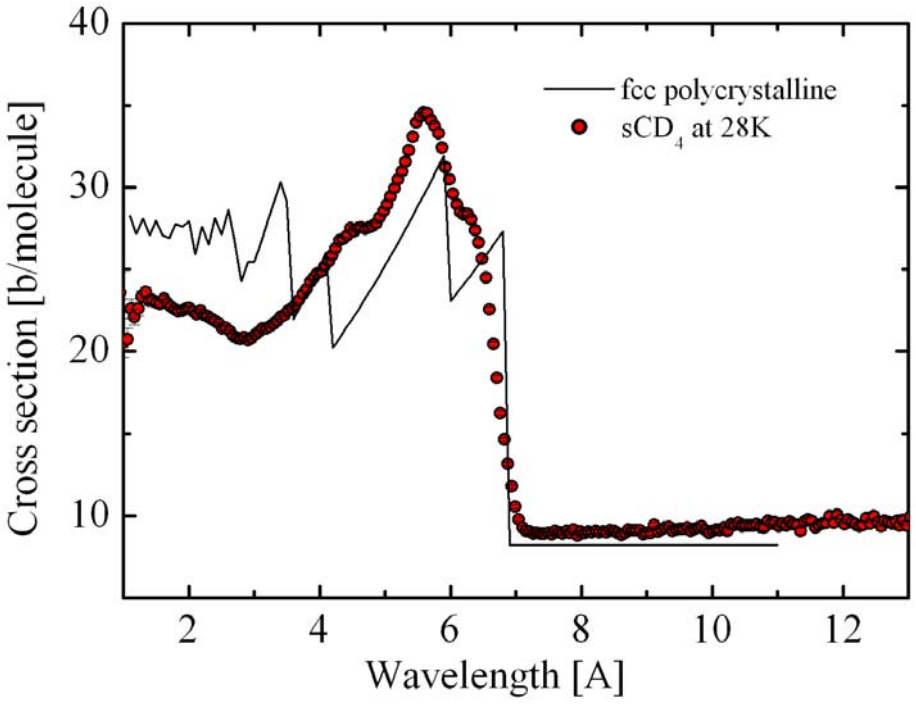

Figure 5.7: Measured total neutron scattering cross sections in the region of Bragg scattering as a function of the neutron wavelength for solid (at 28K) CD_4. The theoretical calculations show the elastic total cross section for the fcc lattice (polycrystalline). The cross section values above the Bragg cut-off wavelenght can be explained by the incoherent contribution from the deuterium atoms (4×2.05 b), since there is no incoherent cross section for ^{12}C. Note the slight increase in cross sections towards long wavelength indicating thermal upscattering, see also Figure 5.8.

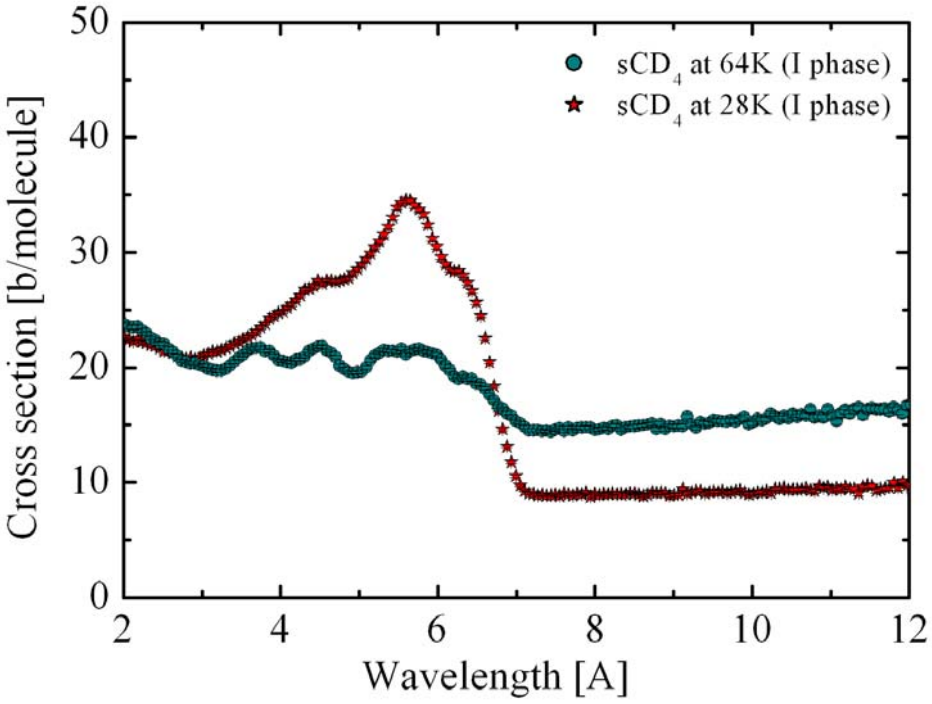

Figure 5.8: Measured total neutron scattering cross sections in the region of Bragg scattering as a function of the neutron wavelength for solid CD_4 in phase I at two different temperatures at 64K (circles) and 28K (stars). The Bragg cut-off is at about the same wavelength, but the cross section in the Bragg region is higher at lower temperature. In the region above the Bragg cut-off wavelength, the cross section is higher and also increasing with wavelength, suggesting strong thermal upscattering. This behavior of the cross section is similar for solid D_2 (see Figure 5.4). The cross section above the Bragg cut-off wavelength is about 8 b/molecule, which is comparable to the incoherent cross section of the D atoms, i.e. 4×2.05 barn.

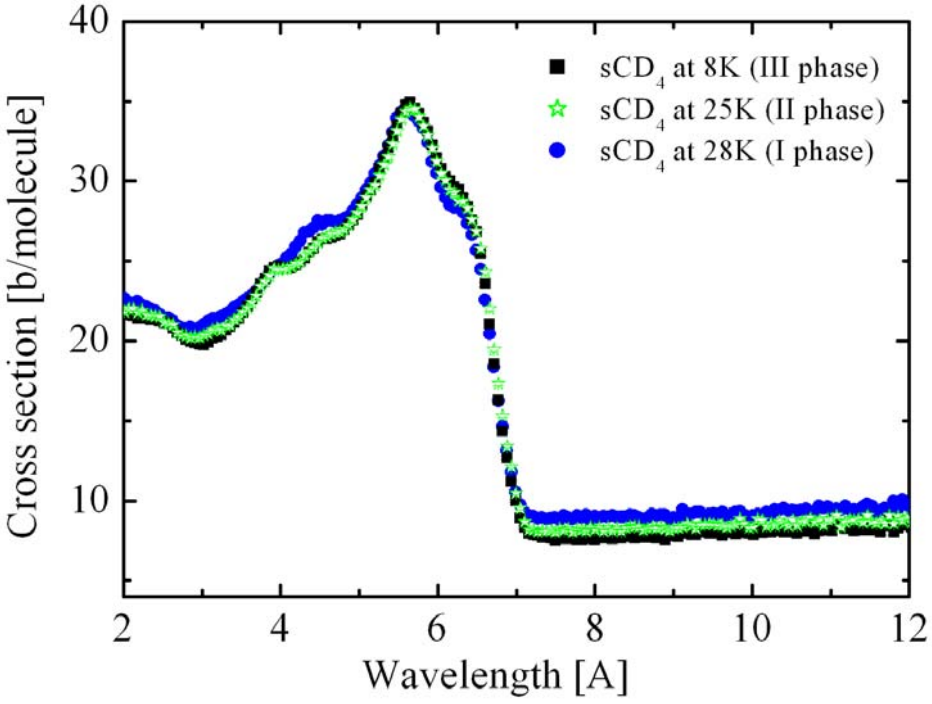

Figure 5.9: Measured total neutron scattering cross sections in the region of Bragg scattering as a function of the neutron wavelength for solid CD_4 in different phases (the data points overlap: phase I (circles), phase II (stars), phase III (squares)). The cross sections are the same, suggesting no change in the crystal structure, this is in agreement with the crystallographic data [100]. It is interesting to compare these results with Figure 5.8 and Figure 5.4. The fact that the cross section doesn't change with lowering temperature might indicate that the sCD_4 sample obtained at 28 K was a polycrystal. It is also worth noting that the phase change doesn't influence the crystal structure strongly, however, it can be seen in the Raman spectra (see Figure 5.10).

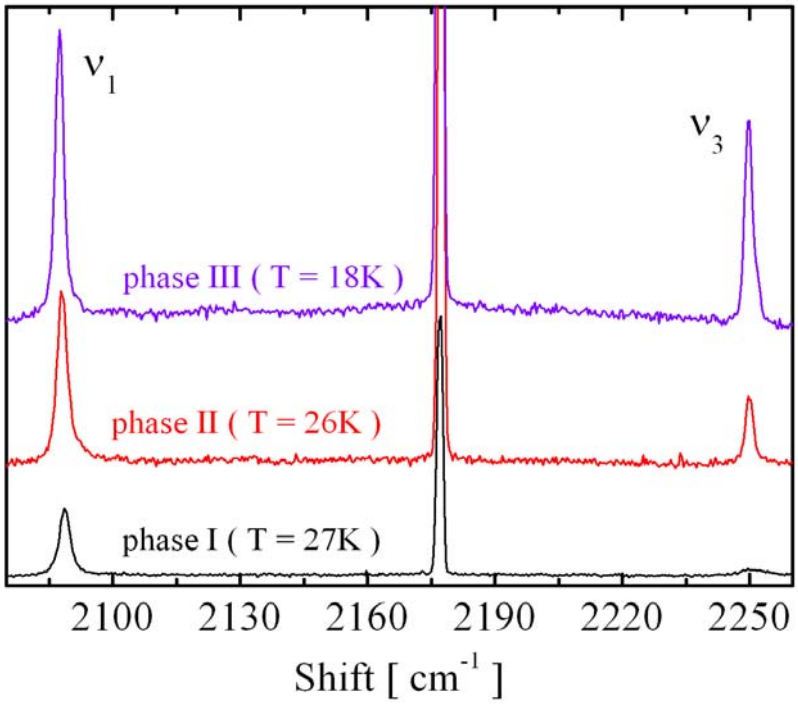

Figure 5.10: The Raman spectra of solid CD_4 in variuos phases (see also [104]). Measured bands are: ν_1 (2084.7 cm^{-1}) and ν_3 (2258.2 cm^{-1}), which represent C-D stretch vibrations. In liquid CD_4 we have observed only the ν_1 band. In the first phase, the ν_1 band has been observed as well as the broad and small ν_3 line. The biggest change in the Raman spectrum has been observed during first phase transition (phase I to phase II), namely, the ν_3 line became much more pronounced and narrower. The observations are in agreement with [105].

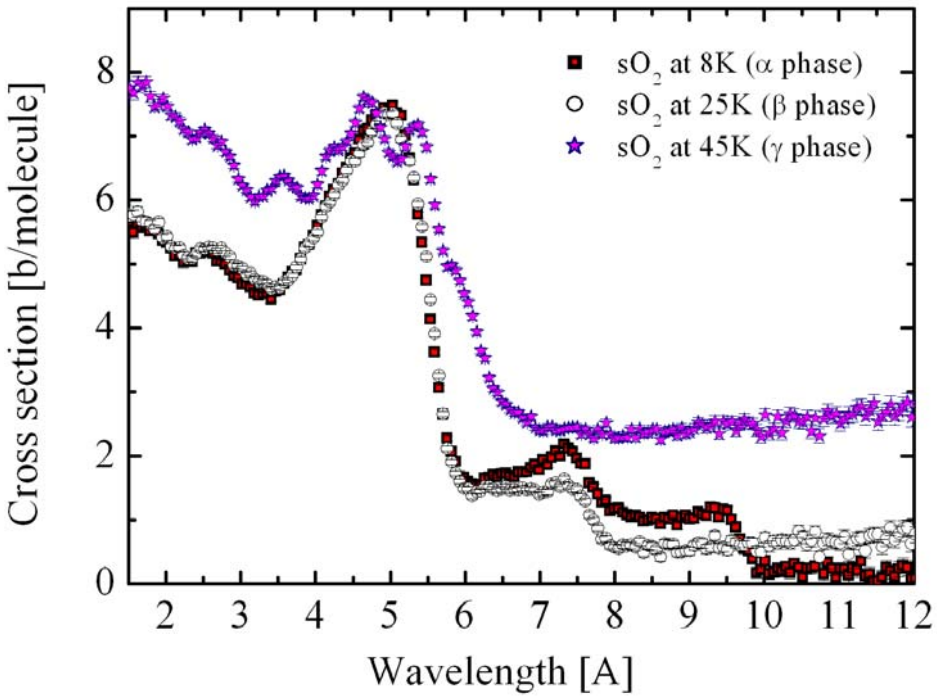

Figure 5.11: Measured total neutron scattering cross sections in the region of Bragg scattering as a function of the neutron wavelength for three phases of solid oxygen. It is interesting to note that the cross section changes with the phase change. In the cubic γ-phase (triangles), one pronounced Bragg edge is visible (starting at about 7 Å). In the rhombohedral β-phase (stars), two Bragg edges show up - one at about 8 Å and the second at 6 Å- and in the monoclinic α - phase (spheres), three Bragg edges appear - two basically the same as for the β-phase and one additional at about 10 Å. Those observations can be explained by the different crystal structures and thus different lattice parameters of α-, β-, γ-phases of solid oxygen (see Tab. 5.2). Above the Bragg cut-off wavelength, the cross section at low temperatures tends to 0, which is in agreement with the fact that oxygen (^{16}O) has no incoherent cross section.

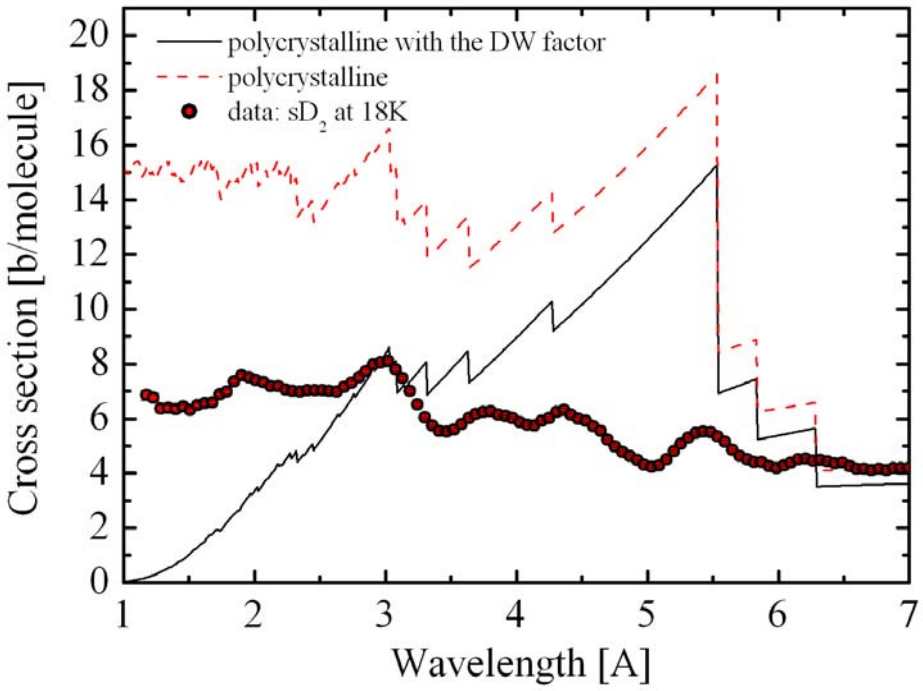

Figure 5.12: The influence of the Debye-Waller factor on the elastic cross section calculation for solid D_2. The reduction of the elastic cross section at shorter wavelength is compensated by the inelastic contribution coming from the rotational excitations. In the wavelength region shown here, the excitations of following rotational levels are possible: J=1, 2, 3, 4; according to Eq. 5.8 the corresponding energies (wavelengths) are E = 7.5 meV (3.3 Å), 22.5 meV (1.9 Å), 45 meV (1.35 Å), 75 meV (1.05 Å).

5.5 The Dynamics of the Crystal Lattice

The dynamics of the lattice is presented using the formalism of phonons. The basic idea comes from the quantum mechanical treatment of the linear chain, i.e. a finite system of N discrete point masses lined up on a one-dimensional linear chain, being separated by an equilibrium distance a. The quantized vibration of the system are called phonons. The neutrons exchange energy with collective motions in solid by creation or anihilation of phonons. Those processes are described by the ladder operators. At low temperatures and low neutron energies, the so-called one-phonon processes, in which one phonon is created or annihilated, predominate, but with an increase of temperature and energy, the multiphonon processes become increasingly important (see Figure 5.13).

The phonon frequency spectrum for a given crystal can be approximated by a Debye model, which assumes that the ordinary velocity of sound observed in a crystal at radio frequencies will hold approximately up to the cut-off frequency ω_D, charactarized by the Debye temperature θ_D.

$$\theta_D = \frac{\hbar\omega_D}{k_B} \tag{5.56}$$

The normalized phonon density of states according to the Debye model is:

$$Z(\omega) = \frac{3\ \omega^2}{\omega_D^3} \tag{5.57}$$

The position vector of the lth atom in the crystal of N atoms can be written as:

$$\boldsymbol{R}_l = \boldsymbol{\rho}_l + \boldsymbol{u}_l(t) \tag{5.58}$$

where $\boldsymbol{\rho}_l$ represents the equilibrium position of the lth atom. The displacement $\mathbf{u}_l(t)$ of the atoms from their equilibrium configuration for the harmonic lattice can be written as [33]:

$$\mathbf{u}_l(t) = \sum_{s,\boldsymbol{q}} \left[\boldsymbol{\xi}_i(s,\boldsymbol{q}) a_{s,\boldsymbol{q}} + \boldsymbol{\xi}_i^*(s,\boldsymbol{q}) a_{s,\boldsymbol{q}}^+\right] \tag{5.59}$$

where $\boldsymbol{q}$ is the wave vector, $a_{s,\boldsymbol{q}}$ and $a_{s,\boldsymbol{q}}^+$ are the phonon annihilation and creation operators

$$a_{s,\boldsymbol{q}}|n_{s,\boldsymbol{q}}\rangle = \sqrt{n_{s,\boldsymbol{q}}}\ |n_{s,\boldsymbol{q}} - 1\rangle \tag{5.60}$$

$$a_{s,\boldsymbol{q}}^+|n_{s,\boldsymbol{q}}\rangle = \sqrt{n_{s,\boldsymbol{q}} + 1}\ |n_{s,\boldsymbol{q}} + 1\rangle \tag{5.61}$$

and

$$\boldsymbol{\xi}_i(s,\boldsymbol{q}) = \sqrt{\frac{\hbar}{2NM\omega_s(\boldsymbol{q})}}\ \boldsymbol{\gamma}_s(\boldsymbol{q})\ \exp\left(i\boldsymbol{q}\cdot\boldsymbol{\rho}\right) \tag{5.62}$$

$\omega_s(\boldsymbol{q})$ represents the normal-mode frequencies, the index s=1,2,3 denotes the three solution for ω for each $\boldsymbol{q}$ [106] and $\boldsymbol{\gamma}_s(\boldsymbol{q})$ is related to the polarization vector. We assume that all

the atoms have the same mass M. Substituting 5.58 and 5.59 into the matrix element of the general incoherent cross section formula:

$$\left(\frac{d^2\sigma}{d\Omega dE'}\right)_{\text{inc}} = \frac{1}{N}\frac{k}{k_0}b_{\text{inc}}^2 \sum_{\lambda'\lambda} p_\lambda \sum_l \left|\langle\lambda'|\exp(i\boldsymbol{\kappa}\cdot\mathbf{R}_l)|\lambda\rangle\right|^2 \delta(\hbar\omega + E_\lambda - E_{\lambda'})$$
$$\equiv \frac{k}{k_0}b_{\text{inc}}^2\ S_{\text{inc}}(\boldsymbol{\kappa},\omega) \qquad (5.63)$$

where κ is the momentum transfer

$$\kappa = \sqrt{k_0^2 + k^2 - 2kk_0\cos\varphi} \qquad (5.64)$$

gives

$$\langle\lambda'|\exp(i\boldsymbol{\kappa}\cdot\mathbf{R}_i)|\lambda\rangle = \exp(i\boldsymbol{\kappa}\cdot\boldsymbol{\rho}_i)$$
$$\times\prod_{s,\boldsymbol{q}}\langle\lambda'|\exp\left\{i\boldsymbol{\kappa}\cdot\left[\boldsymbol{\xi}_i(s,\boldsymbol{q})a_{s,\boldsymbol{q}} + \boldsymbol{\xi}_i^*(s,\boldsymbol{q})a_{s,\boldsymbol{q}}^+\right]\right\}|\lambda\rangle \qquad (5.65)$$

Applying a Taylor expansion of the exponential function in the operator we get

$$\exp\left\{i\boldsymbol{\kappa}\cdot\left[\boldsymbol{\xi}_i(s,\boldsymbol{q})a_{s,\boldsymbol{q}} + \boldsymbol{\xi}_i^*(s,\boldsymbol{q})a_{s,\boldsymbol{q}}^+\right]\right\} = 1 + i\boldsymbol{\kappa}\cdot\left[\boldsymbol{\xi}_i(s,\boldsymbol{q})a_{s,\boldsymbol{q}} + \boldsymbol{\xi}_i^*(s,\boldsymbol{q})a_{s,\boldsymbol{q}}^+\right] +$$
$$-\frac{1}{2}\left[(\boldsymbol{\kappa}\cdot\boldsymbol{\xi}_i)^2 a_{s,\boldsymbol{q}}^2 + (\boldsymbol{\kappa}\cdot\boldsymbol{\xi}_i)^2(a_{s,\boldsymbol{q}}^+)^2 + |\boldsymbol{\kappa}\cdot\boldsymbol{\xi}_i|^2(a_{s,\boldsymbol{q}}a_{s,\boldsymbol{q}}^+ + a_{s,\boldsymbol{q}}^+ a_{s,\boldsymbol{q}}\right] + \ldots \qquad (5.66)$$

Since $a_{s,\boldsymbol{q}}$ and $a_{s,\boldsymbol{q}}^+$ annihilate and create, respectively, phonons, we see that the second term changes the phonon number by one, while the third term changes the phonon number by two or zero.
To calculate the one-phonon contribution to the neutron cross section we can use 5.60, 5.61 and 5.62 and write 5.65 as:

$$\langle\lambda'|\exp(i\boldsymbol{\kappa}\cdot\mathbf{R}_i)|\lambda\rangle = \exp\left[-W(\boldsymbol{\kappa})\right]\sqrt{\frac{\hbar}{2NM\omega_s(\boldsymbol{q})}}\ i\boldsymbol{\kappa}\cdot\boldsymbol{\gamma}(s,\boldsymbol{q})$$
$$\times\begin{cases}\exp\left[i\boldsymbol{\rho}_i\cdot(\boldsymbol{\kappa}-\boldsymbol{q})\right]\sqrt{n_{s,\boldsymbol{q}}+1} & \text{phonon creation}\\ \exp\left[i\boldsymbol{\rho}_i\cdot(\boldsymbol{\kappa}+\boldsymbol{q})\right]\sqrt{n_{s,\boldsymbol{q}}} & \text{phonon annihilation}\end{cases} \qquad (5.67)$$

where the term $\exp[-W(\boldsymbol{\kappa})]$, the Debye-Waller factor, describes the zero phonon expansion. For a cubic lattice $W(\boldsymbol{\kappa})$ is [106]:

$$W(\boldsymbol{\kappa}) = \frac{1}{6}\kappa^2\langle\mathbf{u}^2\rangle \qquad (5.68)$$

where $\langle \mathbf{u}^2 \rangle$ is the mean squared displacement of a nucleus.
Using 5.67, the incoherent double differential cross section of 5.63 becomes:

$$\left(\frac{d^2\sigma}{d\Omega dE'}\right)_{\text{inc}} = \frac{k'}{k} b_{\text{inc}}^2 \sum_{s,\boldsymbol{q}} \frac{\hbar}{2NM\omega_s(\boldsymbol{q})} \exp[-2W(\boldsymbol{\kappa})] |\boldsymbol{\kappa} \cdot \boldsymbol{\gamma}_s(\boldsymbol{q})|^2 \times \begin{cases} [n_s(\boldsymbol{q}) + 1]\ \delta(\hbar\omega_{s,\boldsymbol{q}} - \hbar\omega) & \text{phonon creation} \\ n_s(\boldsymbol{q})\ \delta(\hbar\omega_{s,\boldsymbol{q}} + \hbar\omega) & \text{phonon annihilation} \end{cases} \tag{5.69}$$

Finally, after replacing the summation over s,q by the normalized density of states [106], one obtains:

$$\left(\frac{d^2\sigma}{d\Omega dE'}\right)_{\text{inc}} = \frac{3}{2M} b_{\text{inc}}^2 \frac{k'}{k} \exp[-2W(\boldsymbol{\kappa})] \left\{ |\boldsymbol{\kappa} \cdot \boldsymbol{\gamma}_s(\boldsymbol{q})|^2 \right\}_{\text{av}} \times \frac{Z(\omega)}{\omega} \begin{cases} n(\omega) + 1 & \text{if } \omega \geq 0, \text{ phonon creation} \\ n(\omega) & \text{if } \omega < 0, \text{ phonon annihilation} \end{cases} \tag{5.70}$$

where $\hbar\omega$ is the energy lost by the neutron. The subscript av in 5.70 stands for the average over a surface in $\boldsymbol{\kappa}$ with constant ω and in cubic symmetry this average is equal to $\frac{1}{3}\kappa^2$. The coherent scattering is usually small because it is restricted by the energy and momentum conservation and very often it is sufficient to use the 'incoherent approximation', which consists of using 5.70 with b_{inc}^2 replaced by $b_{\text{coh}}^2 + b_{\text{inc}}^2$. The validity of 'incoherent approximation' is discussed in [69].

Here, it is worth mentioning the influence of the molecular effects on the scattering length. The neutron scattering cross sections depend on the rotational states and as it was pointed out by Sarma [107], and later by Nielsen [99, 108], this effect should be included in the scattering length. Thus for solid ortho-D_2, instead of using energy independent scattering lengths, the form factors of the following form should be applied:

$$f_{0\to 0} = b_{\text{coh}}\ j_0(\frac{\kappa d}{2}) \tag{5.71}$$

$$f_{0\to 1} = b_{\text{inc}}\ j_1(\frac{\kappa d}{2}) \tag{5.72}$$

where $j_i(\frac{\kappa d}{2})$ are the spherical Bessel functions and d denotes the separation between the nuclei in a molecule. The function 5.71 is used when the rotational quantum number J retains the value of zero. This factor accounts for the spatial extension of the molecule. If the rotational quantum number is changed from J to J' (0 to 1 in case of ortho-D_2), the formula 5.72 is also employed. However, this requires that the energy transfer between the neutron and the molecule is larger than the energy difference between the two rotational states, which in the case of ortho-D_2, is equal 7.5 meV.

Equation 5.70 is applied to calculate the upscattering cross section for neutrons in the energy range 100 neV $< E_n <$ 0.5 meV interacting with solid ortho-D_2 at 18 K. Due to low

neutron energies and low temperature of solid D_2, we neglect the multiphonon contribution and the effects connected with the change of the rotational quantum number. Deuterium crystallises in the hcp structure [99, 109] with an intermolecular separation of 3.7 Å. At low temperatures ($T \leq 18$ K) the vibrational v and rotational J quantum numbers are zero. Thus the ortho-D_2 molecule is spherically symmetric and may be considered as a single particle with a neutron scattering length given by the $b\ j_0(\frac{\kappa d}{2})$ in which $b^2 = b^2_{\rm coh} + 5/8 b^2_{\rm inc}$ (following from the statistical weights of the nuclear spin configuration S = 0, 2 of ortho-D_2; see also [87, 90, 91]) and the separation d between the deuterons in the D_2 molecule equal to 0.74 Å. Following [110] we can use a cubic lattice, rather than the actual hcp structure, to describe the solid deuterium structure so that the single phonon scattering cross section is written as

$$\left(\frac{d^2\sigma}{d\Omega dE'}\right)^{1\ \text{phonon}}_{\rm inc} = \frac{1}{2M_{D_2}}\ \left[2b_{\rm coh} j_0\left(\frac{\kappa d}{2}\right)\right]^2\ \frac{k}{k_0}\exp[-2W(\boldsymbol{\kappa})]\ \kappa^2$$
$$\times \frac{Z(\omega)}{\omega}\begin{cases} n(\omega)+1 & \text{if } \omega \geq 0, \text{ phonon creation} \\ n(\omega) & \text{if } \omega < 0, \text{ phonon annihilation} \end{cases} \tag{5.73}$$

The population number $n(\omega)$ of phonons with the frequency

$$\omega = \frac{\hbar}{2M_n}Q^2 \tag{5.74}$$

is given by Bose-Einstein statistics

$$n(\omega) = \frac{1}{\exp\left(\frac{\hbar\omega}{k_B T}\right) - 1}. \tag{5.75}$$

The upscattering cross section is obtained by intergating Eq. 5.73 (phonon anihilation part) over all final energies, starting from the initial neutron energy. The direct validation of this model is done by comparison with the measured total scattering cross section of neutrons with energies 100 neV $<$ E_n $<$ 0.5 meV with solid D_2 (see next section).

5.6 Inelastic Scattering

For neutrons with energies lower than the Bragg cut-off of the material, (for solid D_2 below 2 meV), the total cross section is the sum of the absorption cross section, the inelastic scattering cross section, and the incoherent elastic cross section and can be written as:

$$\sigma_{tot} = \sigma_{inc} + \frac{\Xi}{\sqrt{E}} \tag{5.76}$$

where Ξ is the sum of neutron upscattering processes which have $1/v$ energy dependence:

- the thermal upscattering on phonons calculated according to the formula 5.73,

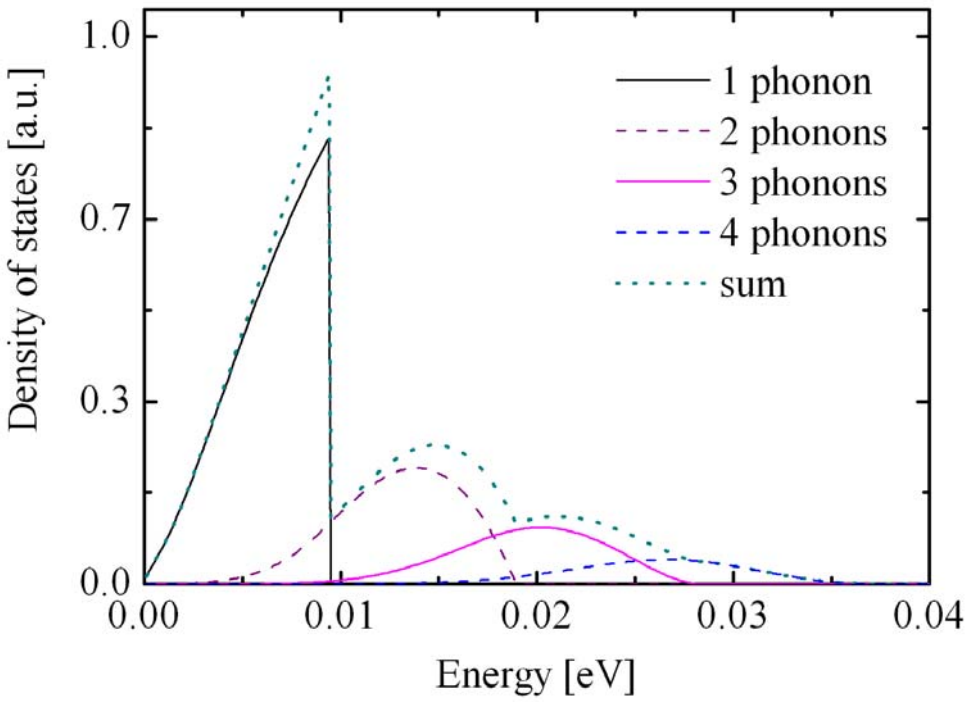

Figure 5.13: The effect of one, two, three and four - phonon processes in case of solid D_2.

- upscattering on para-D_2; the para-D_2 fraction contributes about $1/v \times$ (1-c_0) $\times$ 220 barn m/s (estimated using [110]),
- absorption by D_2 ($1/v \times$ 1.1 barn m/s),
- upscattering on H_2 molecules; the H contamination c_H contributes $c_H \times$ 82 barn incoherent scattering and $1/v \times c_H \times$ 730 barn m/s absorption cross section.

The dominating contribution to Ξ comes from the thermal upscattering on phonons; the other effects are maximal at the lowest energies and at those lower energies amount to an increase in cross section by 2.5 %. The experimental verification of the described model was done by our UCN collaboration and is published in the paper [2]. The measurements have been performed using cold neutrons at the SANS-I instrument [96] of the SINQ facility at PSI and with VCN and UCN at the PF-2 instrument [97] of the Institute Laue-Langevin (ILL). The total cross sections have been measured using the transmission technique (see section 4.3.2). In Figure 5.14 the cross sections for solid ortho-D_2 at 18K are shown together with the theoretical expectation dominated by thermal upscattering calculated using the Debye model.

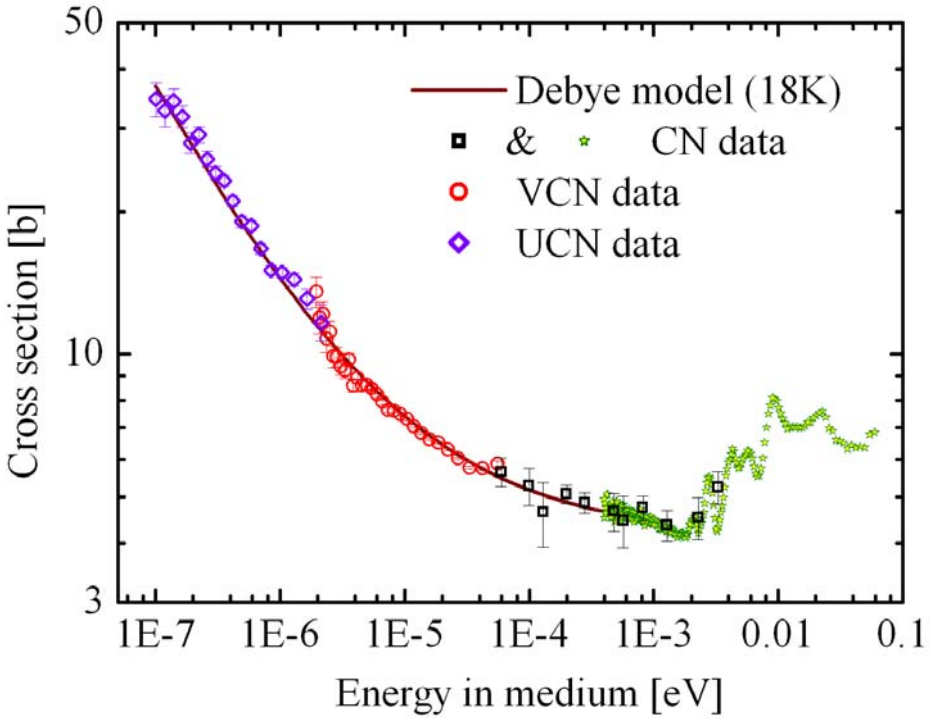

Figure 5.14: Measured total neutron scattering cross sections per molecule as a function of the in-medium neutron energy for solid D_2 at 18 K. The data come from ultracold, very cold, and cold neutron transmission experiments. In the case of the cold neutron cross sections two experiments were performed - one at the SANS-I instrument (black squares) and the second at the FUNSPIN beam (green circles) of the SINQ facility at PSI. For the SANS-I measurements: the Bragg peaks are suppressed due to the poor velocity resolution (about 10%) in the small angle neutron scattering technique measurement. The Bragg peak structure is visible in the second set of data - this measurement was performed using a chopped CN spectrum and the transmission technique. The two sets of results are in good agreement in the shared energy region below about 2 meV; above 2 meV coherent Bragg scattering is possible, but depends on details of the particular crystal. The overlap of different sets of data is very good. The solid brown line represent the theoretical total cross section values calculated assuming a simple Debye model. The low energy part of the cross section reproduced the measured cross sections.

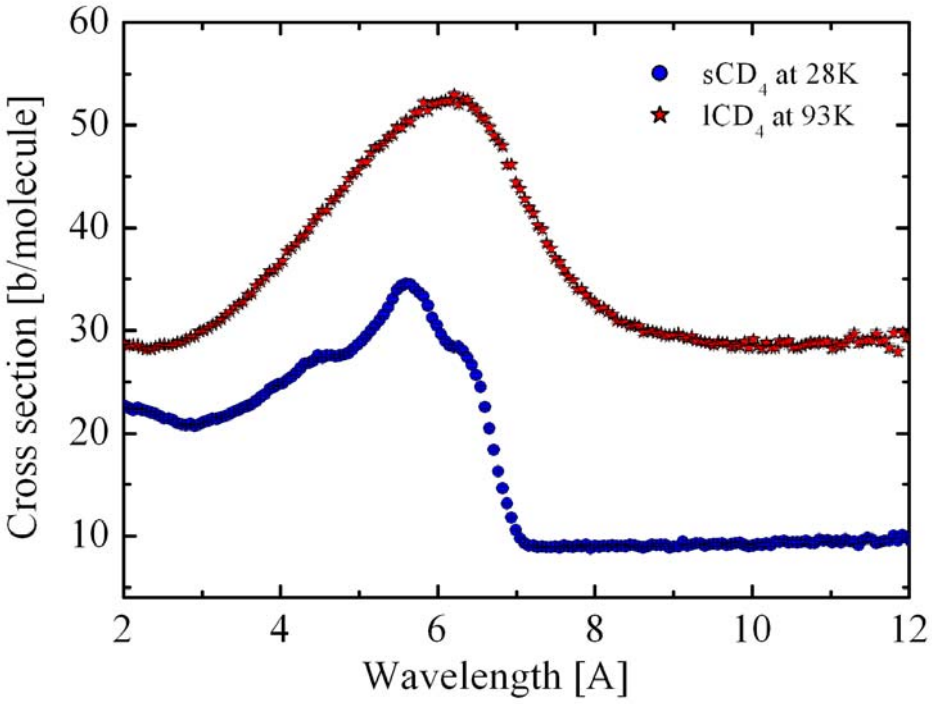

Figure 5.15: Measured total neutron scattering cross sections in the region of Bragg scattering as a function of the neutron wavelength for solid (circles) and liquid (stars) CD_4. The behavior of the cross sections is similar to D_2 cross sections (see Figure 5.2). For liquid CD_4 the cross section is higher above and below the Bragg cut-off.

5.7 Scattering by liquids

In the previous sections we have described in detail the scattering of neutrons by gases and solids which can be understood as two extremes. In the case of gases, we deal with point particles in uncorrelated motion, while in the case of solids, we have a model of crystal lattice and its collective motions. For the liquid states, none of these solutions can be applied. Instead, one needs to determine the structure of the liquid, which is, in fact, the pair-correlation function discussed above (see Tab. 5.1).

Here, the measured total cross sections for liquid CD_4 and O_2 are presented and compared with the solid CD_4 and O_2 cross sections (see Figure 5.15 and Figure 5.16). The total cross section data for liquid D_2 are compared with the total cross sections measured by Seiffert [111].

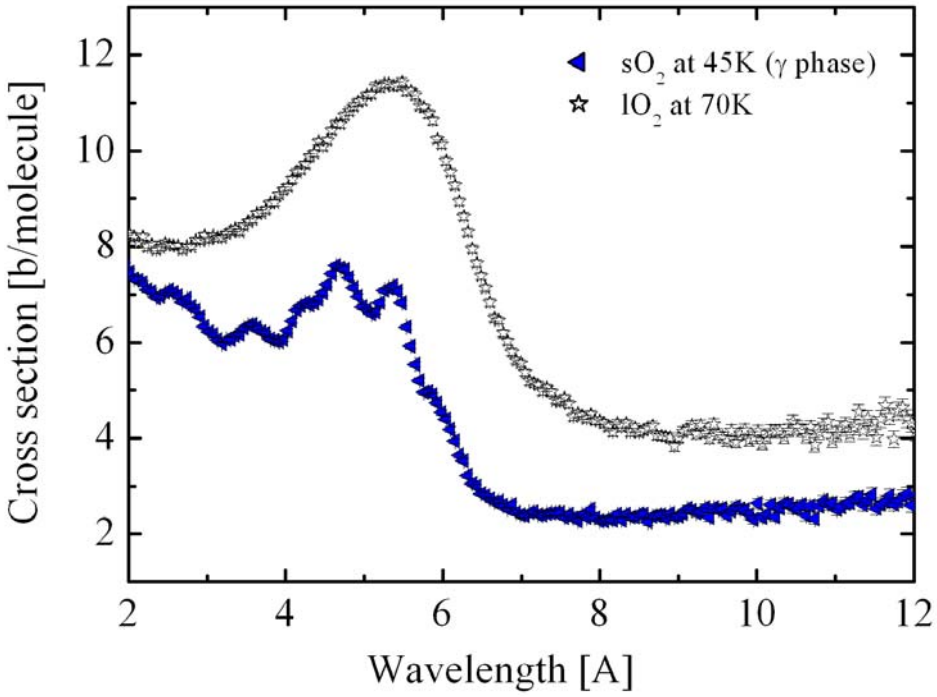

Figure 5.16: Measured total neutron scattering cross sections in the region of Bragg scattering as a function of the neutron wavelength for solid (triangles) and liquid (stars) oxygen. Again the behavior of the liquid O_2 cross sections is similar to the D_2 and CD_4 cross sections, the increase in the cross section in the Bragg scattering region is visible.

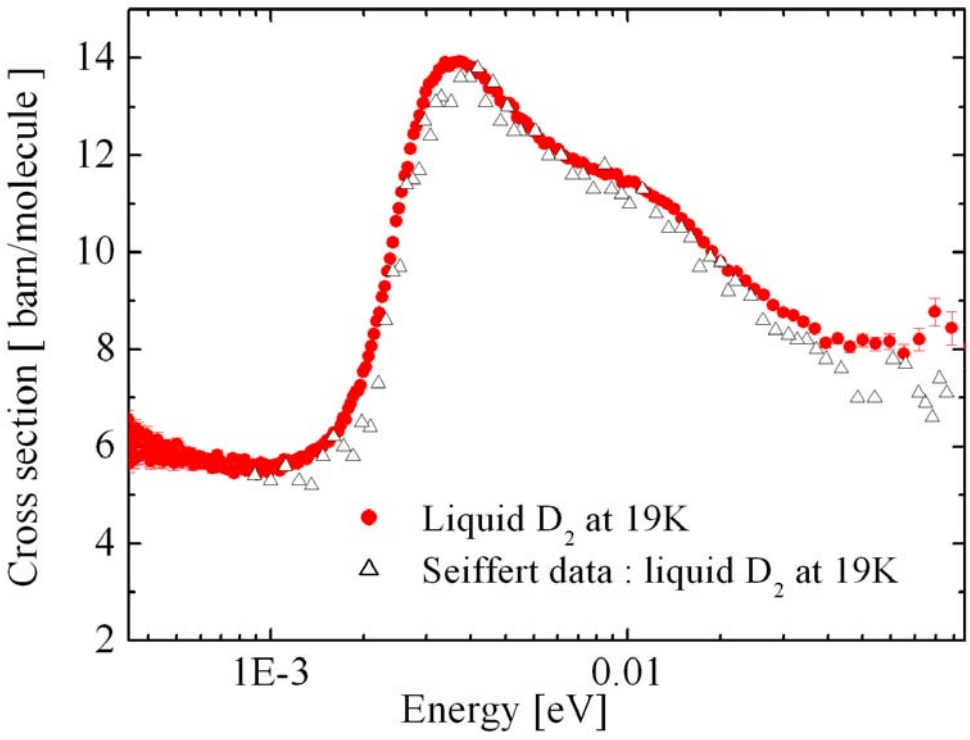

Figure 5.17: Measured total neutron scattering cross sections in the region of Bragg scattering as a function of the neutron wavelength for liquid D_2; our data - circles, Seiffert data - triangles.

Chapter 6

The Production of Ultracold Neutrons - Results of The Measurements

In two experiments, we have successfully measured the absolute UCN production cross sections in gaseous, liquid, and solid D_2, the energy dependent UCN production in gaseous and solid D_2, and the UCN production in O_2 and CD_4. In this chapter we present the results of these measurements, the method of data analysis and the accompanying theoretical discussion. Most of the information gathered in this chapter has already been published (see [2, 4]).

6.1 UCN Production in Deuterium

The measurement of the UCN production rate from cold neutrons interacting in solid D_2 has been done by using a UCN detector with a well-defined geometry and a normalized simulation to calculate the detection efficiency. To expedite this process, results for both liquid and gaseous D_2 have been taken during the experiment. To extract the production cross section from the measured data, we need to deconvolute the overall efficiency function for the UCN spectrometer, including the coupling to the target cell. Presently there is insufficient detailed knowledge to be able to estimate this directly; for instance, we do not know what ratio of diffuse to specular reflection at the guide walls to use or the velocity distribution of the neutrons escaping the target cell. However, these difficulties are by-passed by using results measured for gaseous D_2 to normalize a detailed simulation of the spectrometer. In the case of gas, the scatterer density is low, so that the UCN production in the target cell will be closely being spatially homogeneous. The experimental results of the measurement of cross sections show very good agreement with the model of Young and Koppel for neutron energies down to the UCN region (see chapter 5, Figure 5.1). That is, in the case with gas in the target cell, the main open parameters are reduced to the amount of diffuse scattering and the efficiency of the gas detector (this will include extra losses arising from system imperfections). The D_2 gas results may be used to set values for

these, which can then be used for the liquid and solid D_2 results. Although, in truth, we cannot obtain unique values for these two parameters, it is helpful to keep them separate. The simulation calculations have been carried out using the GEANT4 UCN-Monte Carlo code [112], which tracks UCN through a detailed model of the target cell UCN spectrometer system, and used to extract estimates for the UCN extraction efficiency ε_{ext} for the various sample temperatures.

6.1.1 UCN Storage Mode

The storage mode (SM) measurements were performed to unambiguously demonstrate that the produced neutrons actually were UCN and that quantitative agreement with the flow-through results exists, so that the latter can be used to draw conclusions about UCN production. Storage mode measurements were more time consuming and were made only for the case of solid D_2 at 8K, which was the lowest accessible temperature and gave the highest flow-through rates. Figures 6.1 and 6.2 show examples for different storage times with UCN counts accumulated for 100 filling-storage-emptying cycles. The background has been subtracted from the data. Figure 6.4 shows the resulting UCN counts for four different storage times. An exponential fit to the data points gives a storage lifetime of 24 ± 8 s and an extrapolation to t = 0 of

$$N_{\text{ucn}}^{\text{SM}} = 0.21 \pm 0.03 \tag{6.1}$$

UCN in the bottle at equilibrium per storage cycle. The value in Eq. 6.1 is consistent with the flow-through mode (FM) measurement. The flow-through mode measures the net neutron current through the bottle. The neutron spectrum in the flow through mode is rather wider than can be stored in the bottle, v_c = 6.9 m/s; (45 ± 4)% of the neutrons have $v \leq v_c$ (the hatched area in Figure 6.12). Thus, closing the exit UCN shutter (number 7 in the Figure 4.1) makes the UCN fraction of this current, $I_{\text{ucn}} = 0.45(4) \times I^{FM}$, which fills the bottle. After a filling time t_f, the number of neutrons in the bottle is

$$N_{\text{ucn}} = I_{\text{ucn}} \tau_1 \left(1 - \exp\left(-\frac{t_f}{\tau_1}\right)\right) \tag{6.2}$$

where τ_1 is the UCN lifetime in the bottle with either exit or entrance shutter open. This time constant is dictated by the geometry of the bottle system. The symmetry of the system used suggests that the time constants for the arrangement are the same. Thus, τ_1 can be extracted from the emptying curve of the storage measurements (compare Figures 6.1, 6.2, 6.3) and found to be τ_1 = 0.97 ± 0.25 s. Therefore, the estimated number of UCN in the bottle per filling cycle by using the flow-through data is

$$N_{\text{ucn}}^{\text{FM}} = 0.18 \pm 0.05. \tag{6.3}$$

6.1.2 UCN Production in the Flow-Through Mode

The main results from the experiment are the variation of UCN production with temperature of the D_2; these are shown in Figures 6.5, 6.6, and 6.7 as counts (corrected for

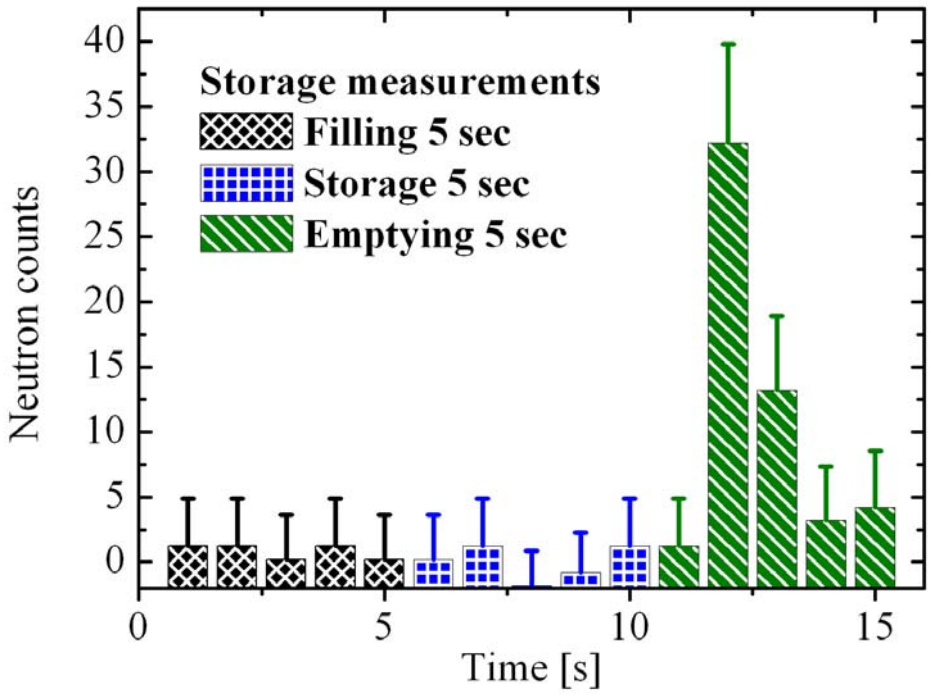

Figure 6.1: Background subtracted time spectra for UCN counts during filling, storing, and emptying times of 5 s each. Those data were taken during the first UCN production experiment in 2004.

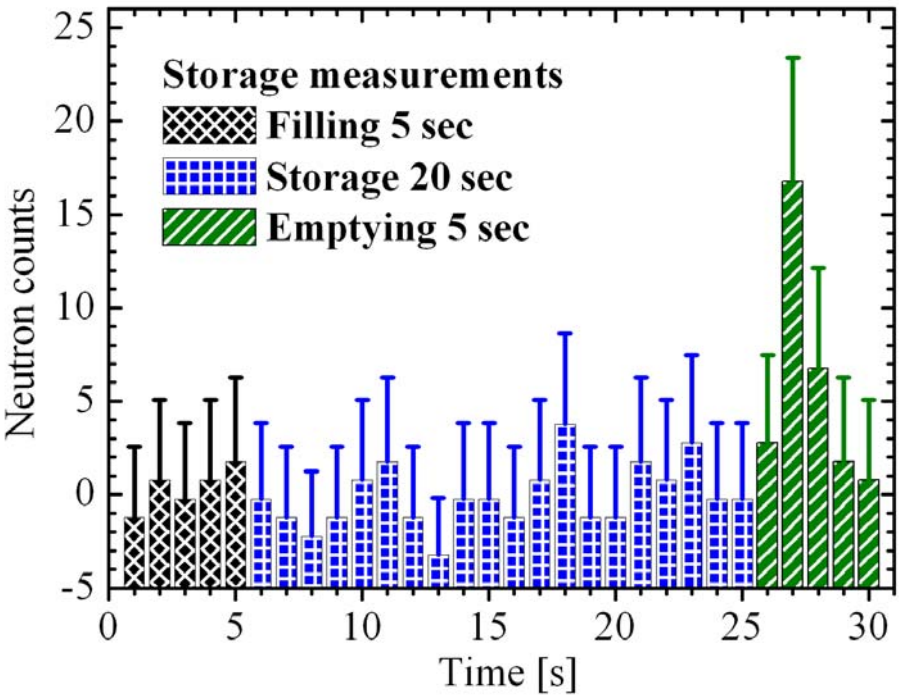

Figure 6.2: Background subtracted time spectra for UCN counts during 5 s filling, 20 s storing, and 5 s emptying. Those data were taken during the first UCN production experiment in 2004.

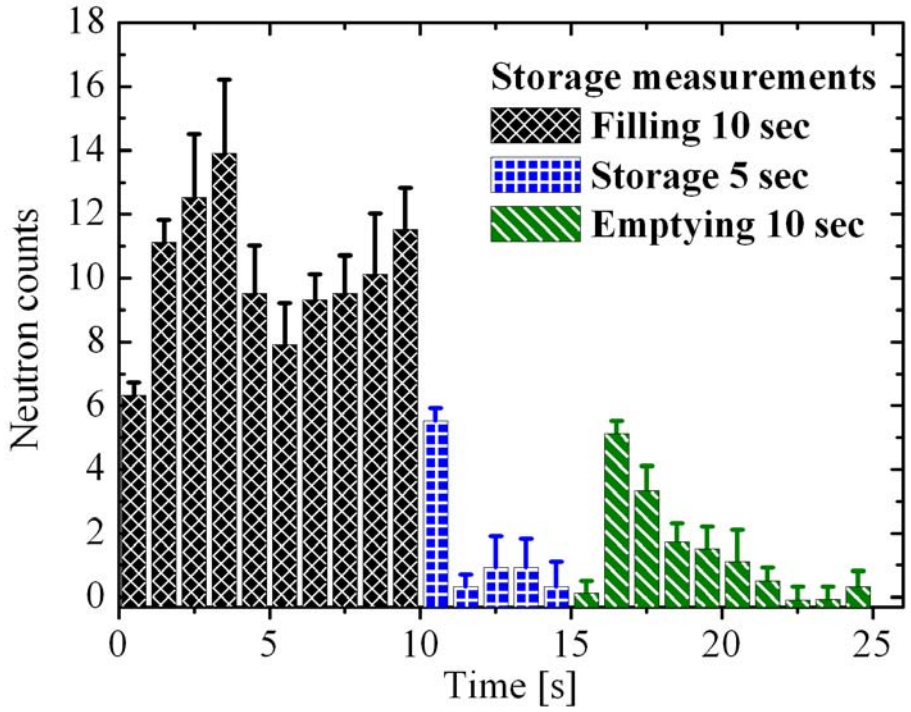

Figure 6.3: Background subtracted time spectra for UCN counts during 5 s filling, 20 s storing, and 5 s emptying. Those data were taken during the second UCN production experiment in 2005. The difference compared to the data taken in 2004 is relatively high background while filling the storage bottle. This is due to another foil material used for the second UCN shutter; in the first experiment we have used a DLC coated PET foil, while during the second experiment, a DLC coated Al foil has been used.

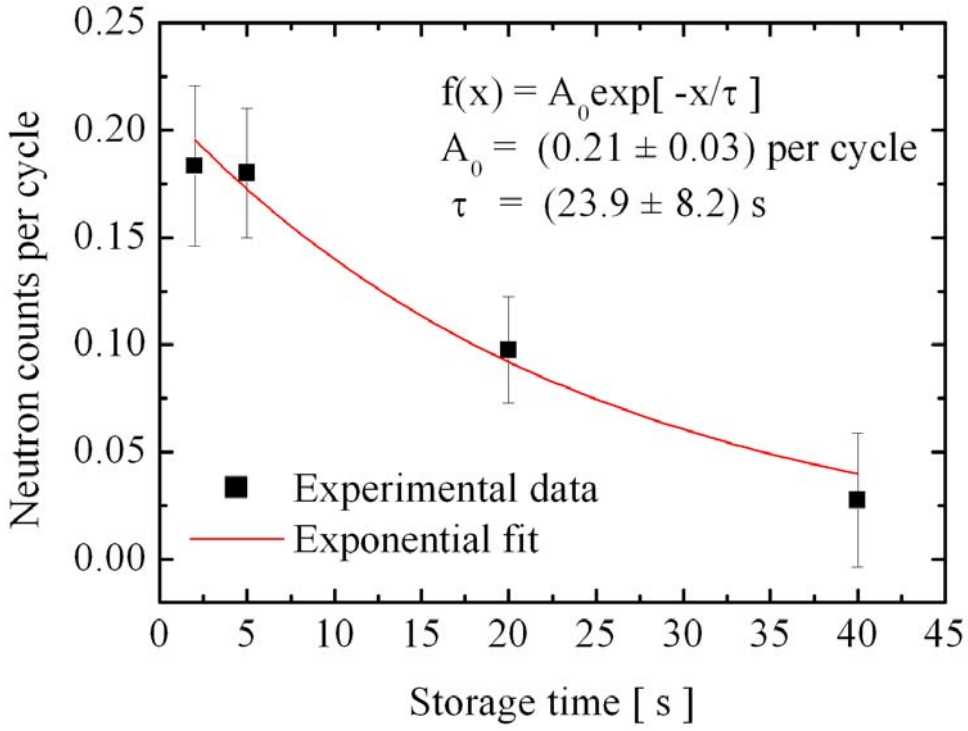

Figure 6.4: Decay of the UCN density in the bottle as a function of storage time. The four measured points are given along with an exponential fit. The storage lifetime is found to be 24 ± 8 s; the equilibrium population after filling is 0.21 ± 0.03 UCN per fill.

background) per coulomb proton charge onto the SINQ target as a function of temperature. At 8K, a neutron current of $I^{\mathrm{FM}} = (0.42 \pm 0.04)\ \mathrm{s}^{-1}$ has been measured for 1.2 mA proton beam onto the SINQ target.

The data shown in Figure 6.5 were measured during the first UCN production experiment in 2004. The data point at 85K shown in Figure 6.5 was measured for the evacuated target cell. Thus, without D_2 in the target, the measured UCN production is consistent with zero. All other data points are with D_2 in the target cell: above 24K as gas, between 24 and 18.7K as liquid, and below 18.7K as solid. Data for two differently prepared crystals are included in Figure 6.7, one was cooled slowly, the other one fast. The results show no difference within the statistical uncertainties. The fact that the treatment of solid D_2 does not influence the UCN yield was confirmed during the second UCN production experiment in 2005. In Figure 6.6 the data for a crystal grown from the liquid and gaseous phase are shown. There is again no significant difference in the number of detected UCN between those two crystals, although when optically observed, the crystal frozen from the gas phase (frozen to 11K and cooled down to 8K) was more transparent and did not have cracks as the crystal which had been frozen from liquid at 18.7K and cooled down to 8K. The difference between the UCN counts in 2005 and 2004 is due to the Fe-analyzer (see chapter 4). After removing the Fe-analyzer the difference in the UCN counts was on the level of the typical systematic fluctuations due to the quality of the grown crystal (about 10%).

In the flow-through mode, the neutron count rate I is measured for a given incoming neutron flux $\Phi(E_i)$ and for various target conditions (gas, liquid, and solid at various temperatures, with D_2 density ρ and illuminated target volume V_D). The integrated neutron flux incident on the target cell was measured using gold foil activation method (see Appendix B) and was[1]:

$$\Phi_{\mathrm{CN}} = (4.5 \pm 1.0) \times 10^7 \mathrm{cm}^{-2}\mathrm{s}^{-1}\mathrm{mA}^{-1} \tag{6.4}$$

Using subscripts i and f to denote values for initial and final states:

$$\frac{I}{\rho V_D} = \int\int \varepsilon_{\mathrm{rest}}\varepsilon_{\mathrm{tra}}\varepsilon_{\mathrm{ext}}\Phi(E_i)\sigma(E_i \rightarrow E_f)dE_i dE_f \tag{6.5}$$

where $\sigma(E_i \rightarrow E_f)$ is the downscattering cross section and three factors are introduced: $\varepsilon_{\mathrm{rest}}$ for the efficiency of the actual detector and other loss factors outside the simulation (e.g. gaps between guide section), $\varepsilon_{\mathrm{tra}}$ the efficiency for transporting the neutrons through the UCN spectrometer and $\varepsilon_{\mathrm{ext}}$ the efficiency for the transport of the neutrons from their production position to the start of the spectrometer. These three factors depend on final energy E_f and are obtained from a simulation of the experiment and from use of measurements with gaseous D_2. The experiment is not set up[2] to measure the influence of the incident energy E_i, and σ is replaced by an average cross section for producing neutrons of energy E_f, $\bar{\sigma}(E_f)$, which is proportional to $\sqrt{E_f}$. Equation 6.5 may be rewritten as

$$\frac{I}{\rho V_D} = \Phi_{\mathrm{CN}} \int \varepsilon_{\mathrm{rest}}\varepsilon_{\mathrm{tra}}\varepsilon_{\mathrm{ext}}\bar{\sigma}(E_f)dE_f. \tag{6.6}$$

[1] During the experiment in 2004.

[2] However, see section 6.2 - Energy Dependent UCN Production in Deuterium

The dependence of $\varepsilon_{\text{rest}}$ on E_f will be weak and can be separated and replaced by an average $\bar{\varepsilon}_{\text{rest}}$. It is also sometimes more convenient to work with velocity as the dependent variable. The velocity dependence of $\bar{\sigma}(v_f) = \bar{\sigma}^{\text{CN}\to\text{UCN}} f(v)$ is known, $f(v) \sim v^2$, so that Equation 6.6 can be written as

$$\frac{I}{\rho V_D} = \Phi_{\text{CN}} \bar{\varepsilon}_{\text{rest}} \bar{\sigma}^{\text{CN}\to\text{UCN}} \int P(v) dv, \tag{6.7}$$

where

$$P(v) = f(v)\varepsilon_{\text{tra}}(v)\varepsilon_{\text{ext}}(v) \tag{6.8}$$

with the normalization condition

$$\int_{v_1}^{v_2} f(v) dv = 1 \tag{6.9}$$

where v_1 and v_2 are the velocities *in* the target material that lead to UCN storable in the bottle.

UCN Production by D_2 Gas and the Extraction of Values for ε_{tra} and $\bar{\varepsilon}_{\text{rest}}$

The main open parameter stopping the determination of ε_{tra} is the diffuse scattering fraction at the guide wall. A value can be assigned that together with $\bar{\varepsilon}_{\text{rest}}$ matches experiment and simulation calculation. It is clear that unique values cannot be obtained. However, limiting values to those that are physically reasonable, e.g., a diffuse scattering fraction of more than 3% would require $\bar{\varepsilon}_{\text{rest}}$ to be greater than 1, yields an indicative value for the diffuse scattering fraction. Finally, the diffuse scattering fraction is set in the simulation to 1% as this leads to a reasonable numerical value for $\bar{\varepsilon}_{\text{rest}}$.

The individual calculated values for ε_{tra} and ε_{ext} obtained from the gas-target simulation are show in Figure 6.8, and the values for the efficiency function $P(v)$ are displayed in Figure 6.9. The neutrons contributing to the UCN stored in the bottle lie in the energy range 100 to 350 neV in the gas, so that

$$P_{\text{int}}^{\text{gas}} = \int_{4.37\ \text{m/s}}^{8.18\ \text{m/s}} P(v) dv = 0.037. \tag{6.10}$$

The detailed results of the simulation show that the UCN extraction efficiency is almost independent of temperature, as the variation of density and neutron upscattering cross section virtually compensate one another; the measured values for the gas target (collected in the Tab. 6.1) are consistent with this.

We use the Young and Koppel model (see chapter 5) to calculate the downscattering cross section σ_{YK} of neutrons of initial energy E_i into the UCN region. The final energies have been set to the interval 100 - 350 neV, which is consistent with the energy range for neutrons in the gas that can be stored in the bottle at 1 m height.

$$\sigma_{\text{YK}}(E_i \to E_{\text{UCN}}) = \int_{100\ \text{neV}}^{350\ \text{neV}} \frac{d\sigma_{\text{YK}}}{dE_f}(E_i) dE_f \tag{6.11}$$

Table 6.1: Measured numbers of UCN (flow-through mode) for a proton beam charge of 1 C on the SINQ spallation target for different target conditions. The measurements were made while warming up the target and the temperatures given are average values. The D_2 number densities ρ have been calculated for the van der Waals gas parameters of Ref.[113]. Within the experimental uncertainties I/ρ is constant.

T [K]	D_2 number density ρ [cm^{-3}]	UCN rate I [C^{-1}]	I/ρ [C^{-1} cm^3]
24	3.19×10^{20}	104 ± 12	3.3 (4) $\times 10^{-19}$
48	2.08×10^{20}	71 ± 10	3.4 (5) $\times 10^{-19}$
64	1.54×10^{20}	50 ± 10	3.2 (6) $\times 10^{-19}$
75	1.31×10^{20}	45 ± 9	3.4 (7) $\times 10^{-19}$
85	Evacuated	-2 ± 5	

$$\sigma_{\mathrm{YK}}^{\mathrm{CN}\to\mathrm{UCN}} = \int \Phi(E_i)\sigma_{\mathrm{YK}}(E_i \to E_{\mathrm{UCN}})dE_i \tag{6.12}$$

The calculated downscattering cross section, $\sigma_{\mathrm{YK}}^{\mathrm{CN}\to\mathrm{UCN}}$, together with other derived parameters relevant to estimation of $\bar{\varepsilon}_{\mathrm{rest}}$ are collected in Table 6.2. The (positive) uncertainties attached to the values of $\sigma_{\mathrm{YK}}^{\mathrm{CN}\to\mathrm{UCN}}$ in Table 6.2 come from an estimation of the contribution of lower energy neutrons in the FUNSPIN spectrum. This estimate was made using an extrapolation assuming that the source spectrum for the FUNSPIN guide is Maxwellian. We note that this adds at most a few percent additional uncertainty, which is small compared to the statistical uncertainty of the gas measurement. The four individual determinations of $\bar{\varepsilon}_{\mathrm{rest}}$ (see Table 6.2)are statistically consistent and give an overall average value of

$$\bar{\varepsilon}_{\mathrm{rest}} = 0.74 \pm 0.06 \pm 0.16. \tag{6.13}$$

This value is affected by the ($\pm$ 0.16) systematic uncertainty of the cold neutron flux determination (see Eq.6.4). However not affected by this systematics is the product

$$\bar{\varepsilon}_{\mathrm{rest}}\Phi_{\mathrm{CN}} = (3.33 \pm 0.27) \times 10^{10}\mathrm{C}^{-1} \tag{6.14}$$

Table 6.2: Calculated downscattering (single scattering) cross sections per molecule averaged over the incoming cold neutron spectrum and various D_2 gas temperatures. See text for an explanation of the uncertainties in the second column; E_{UCN} = 100...350 neV; V = 45 cm^3; $R_{gas} = \sigma_{YK}^{CN\to UCN}\rho$; $P_{UCN} = \Phi_{CN} R_{gas} V$; P_{int}=0.037; $\bar{\varepsilon}_{rest} = I/(P_{int}P_{UCN})$. The attached errors on $\bar{\varepsilon}_{rest}$ concern the last digits and are for the statistical uncertainty (first) and the systematics (second) coming from the measurement of Φ_{CN}. The values in the last column are not affected by this systematic uncertainty.

T [K]	$\sigma_{YK}^{CN\to UCN}$ [10^{-30} cm^2]	R_{gas} [10^{-9} cm^{-1}]	P_{UCN} [C^{-1}]	$P_{UCN}P_{int}$ [C^{-1}]	$\bar{\varepsilon}_{rest}$	$\bar{\varepsilon}_{rest}\Phi_{CN}$ [10^{10} C^{-1}]
24	6.63(+0.22)	2.11	4273	158	0.66(8)(15)	2.96(36)
48	6.01(+0.16)	1.25	2531	94	0.76(11)(17)	3.41(49)
64	5.66(+0.15)	0.87	1762	65	0.77(15)(17)	3.45(67)
75	5.42(+0.14)	0.71	1438	53	0.85(17)(19)	3.81(76)

UCN Production by Liquid D_2

In case of liquid D_2, the high density means that both the incident cold neutrons and the produced UCN will be significantly attenuated over the length of the target. These effects are taken into account in the simulation of ε_{ext}. The CN flux distribution within the liquid D_2 is calculated using the code MCNPX [114]; the measured incoming spectrum and the liquid ortho-D_2 scattering law of Bernnat et al. [115] are used, and a selection of flux spectra from the calculation is displayed in Figure 6.10. The expected cooling of the incident CN spectrum may be seen; but as UCN production cross sections averaged over the incident spectrum are used throughout, this effect is not included in the simulation. An attenuation factor $\alpha_{att} = 0.65 \pm 0.10$ is deduced for which $\alpha_{att}\Phi_{CN}$ corresponds to the average cold neutron flux over the target cell. The assigned systematic uncertainty accounts for limitations in the simulation of the target itself and its surroundings. This results are in agreement with the measured CN transmission through liquid D_2 (see Figure 6.11).

The simulation to obtain $P(v)$, see Figure 6.12, uses the calculated spatial variation of cold flux within the liquid together with an isotropic UCN spectrum $f(v) \sim v^2$ to define the source and the measured liquid D_2 cross sections (see chapter 5, Figure 5.2). Taking

a material potential for liquid D_2 of 90 neV (i.e. the neutron energy range for producing stored neutrons in the bottle is now 10 to 260 neV), then

$$P_{\rm int}^{\rm liquid} = \int_{1.38\ {\rm m/s}}^{7.05\ {\rm m/s}} P(v)dv = 0.007 \pm 0.001. \tag{6.15}$$

The systematic uncertainty has been determined from the propagation of the estimated errors in the primary spatial distribution.

The neutron rate for liquid D_2 at 20 K (see Figure 6.7) is measured as $I = (115\pm10)\ {\rm C}^{-1}$. Using the value for $\bar{\varepsilon}_{\rm rest}\Phi_{\rm CN} = (3.33 \pm 0.27) \times 10^{10}\ {\rm C}^{-1}$ determined from the gas results (see Eq. 6.14) and taking the liquid density from [116], then

$$\sigma_{\rm liquid,20K}^{\rm CN\to UCN} = \frac{I}{\alpha_{\rm att}\Phi_{\rm CN}\rho V P_{\rm int}^{\rm liquid}\bar{\varepsilon}_{\rm rest}} = (6.6 \pm 1.6) \times 10^{-31}{\rm cm}^2, \tag{6.16}$$

and

$$R_{\rm liquid,20K} = \sigma_{\rm liquid,20K}^{\rm CN\to UCN}\rho = (1.70 \pm 0.41) \times 10^{-8}{\rm cm}^{-1}. \tag{6.17}$$

UCN Production from Solid D_2

The method used for extraction of UCN production cross sections for solid D_2 is completely analogous to that used for liquid. The $P(v)$ distribution is included in Fig. 6.12. The energy range for the source neutrons is 0 to 250 neV in this case (the material potential of the solid is roughly 100 neV) and

$$P_{\rm int}^{\rm solid} = \int P(v)dv = 0.034 \pm 0.004 \tag{6.18}$$

The uncertainty is dominated by the effect of variations in the UCN scattering and loss cross sections on the extraction efficiency $\varepsilon_{\rm ext}$; because the losses are small, comparable to those in the case of gas target, this turns out to be quite a weak effect.

We detected neutron rates of $I = (360 \pm 10)\ {\rm C}^{-1}$ in solid D_2 at 8K, see Figure 6.7. Again taking $\bar{\varepsilon}_{\rm rest}\Phi_{\rm CN}$ from Eq. 6.14, using the same cold neutron attenuation factor $\alpha_{\rm att}$ as for liquid and taking the solid density from [116], we then obtain

$$\sigma_{\rm solid,8K}^{\rm CN\to UCN} = \frac{I}{\alpha_{\rm att}\Phi_{\rm CN}\rho V P_{\rm int}^{\rm solid}\bar{\varepsilon}_{\rm rest}} = (3.7 \pm 0.8) \times 10^{-31}{\rm cm}^2, \tag{6.19}$$

and

$$\mathrm{R}_{\rm solid,8K} = \sigma_{\rm solid,8K}^{\rm CN\to UCN}\rho = (1.11 \pm 0.23) \times 10^{-8}{\rm cm}^{-1}. \tag{6.20}$$

Discussion

The observation that the differently prepared crystals produce equally high UCN rates allows one to conclude that UCN extraction at 8K, in the geometry of our experiments, is

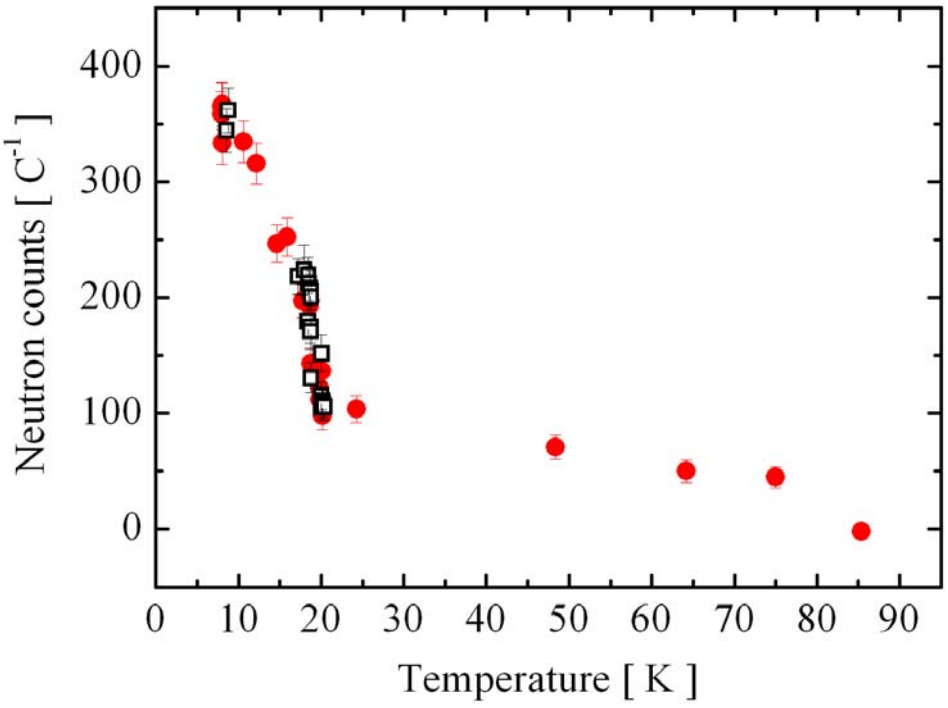

Figure 6.5: Number of neutrons detected in flow-through mode per 1 C of proton charge onto SINQ target as a function of D_2 temperature. The data have been corrected for background (typical background rates: $\sim$ 0.010 - 0.015 s^{-1} at 1.2 mA). The measurement at 85K was with an empty cell to confirm the background correction. One data point typically required 1000 s with 1.2 mA onto the SINQ target.

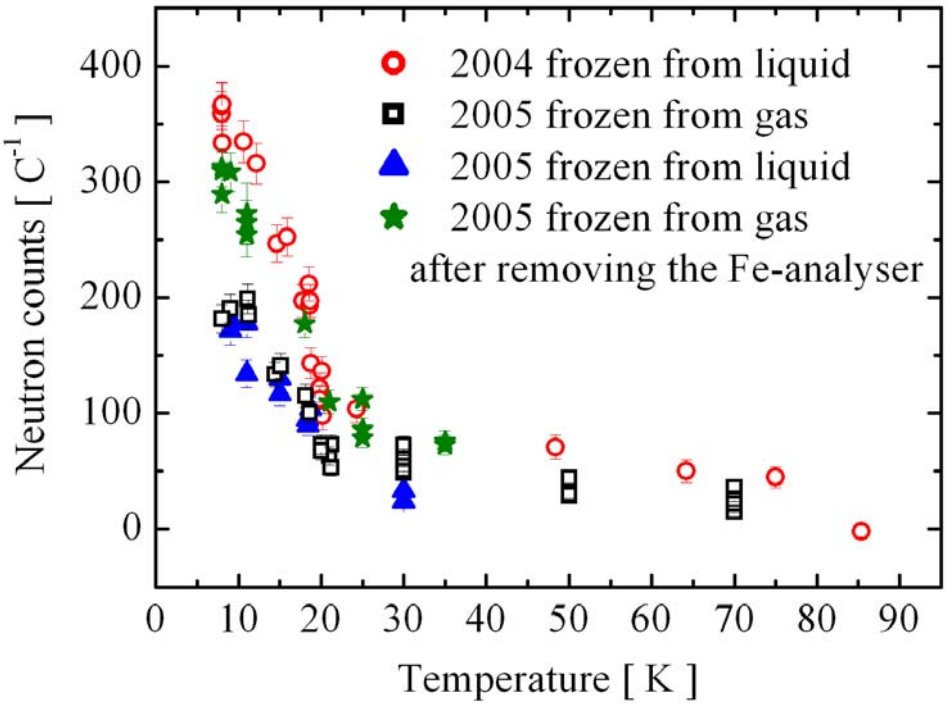

Figure 6.6: Comparison between the data taken during the first (2004) and the second (2005) UCN production experiment. During the measurements with the Fe-analyzer we detected less neutron counts than during the previous experiment (for solid deuterium we have observed 1.8-2 times less). The ratio between the number of neutrons produced in sD_2 at 8K and at 18K is 1.9 (in the last year the ratio was 1.75). We have also observed that for liquid and gaseous deuterium, the number of neutrons is lower by a factor 2. After removing the Fe-analyzer, the number of detected neutrons increased by a factor 1.5.

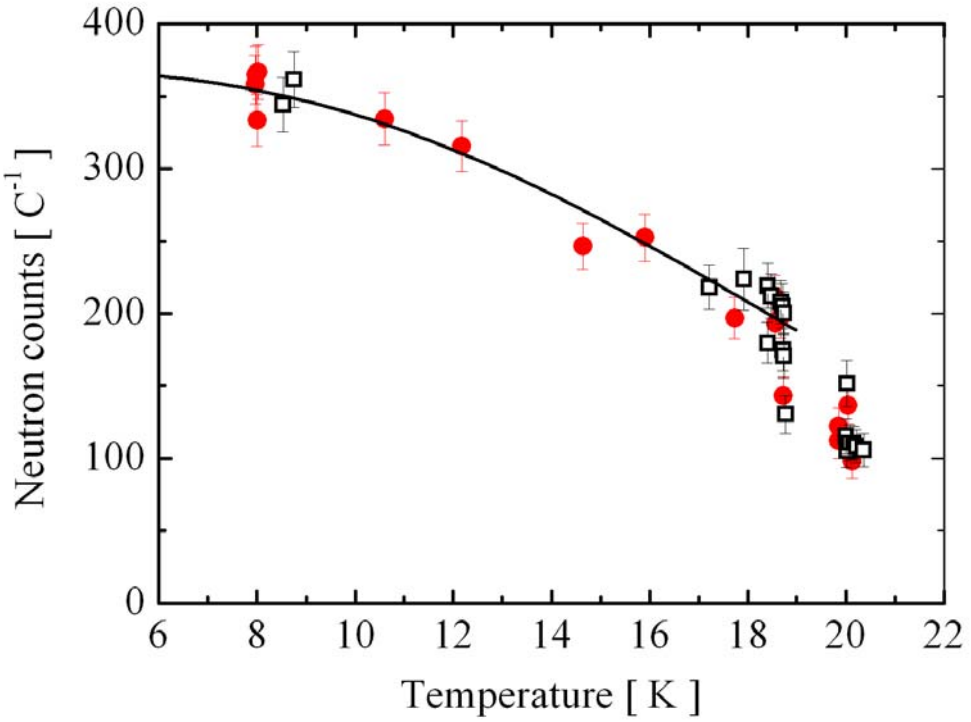

Figure 6.7: Same as Figure 6.5 but zoomed in on the liquid and solid D_2 region. Circles are for the slowly cooled crystal; squares are for the rapidly cooled crystal. The solid line was obtained using the simulation for UCN extraction and taking into account the temperature dependence of both thermal upscattering losses and UCN production.

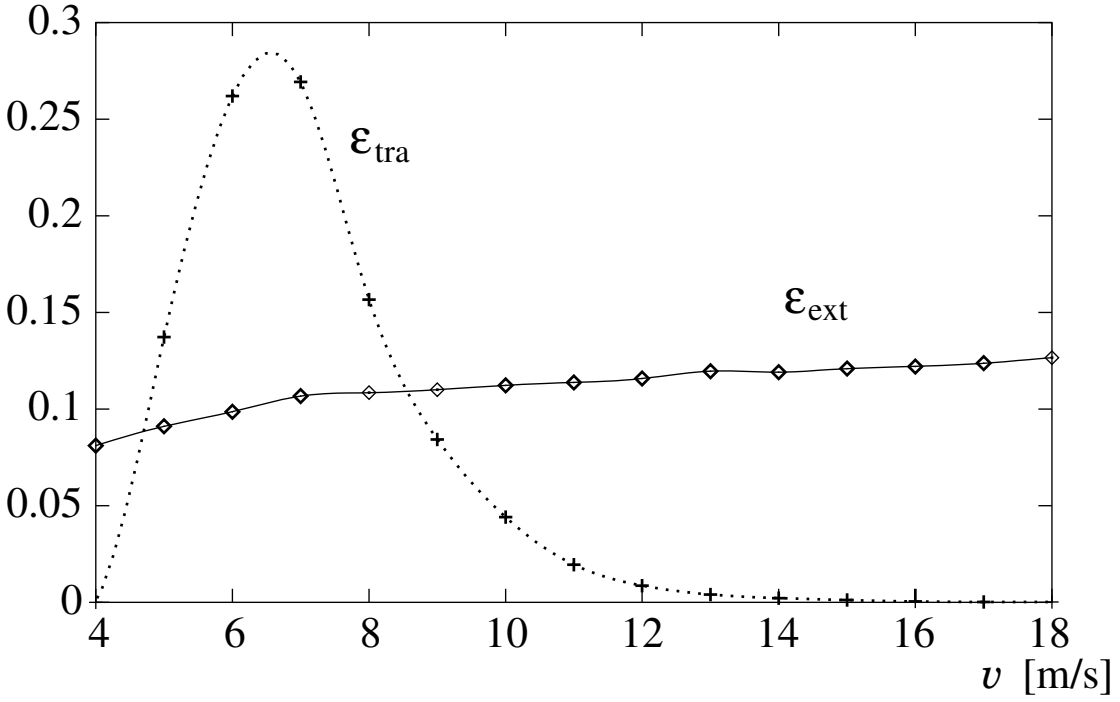

Figure 6.8: Simulated efficiencies for extraction ε_{ext} and transport ε_{ext} as functions of neutron velocity *inside* the D_2 gas target at 24 K. Ultracold neutrons with velocities below 4 m/s in the gas target cannot reach the detector.

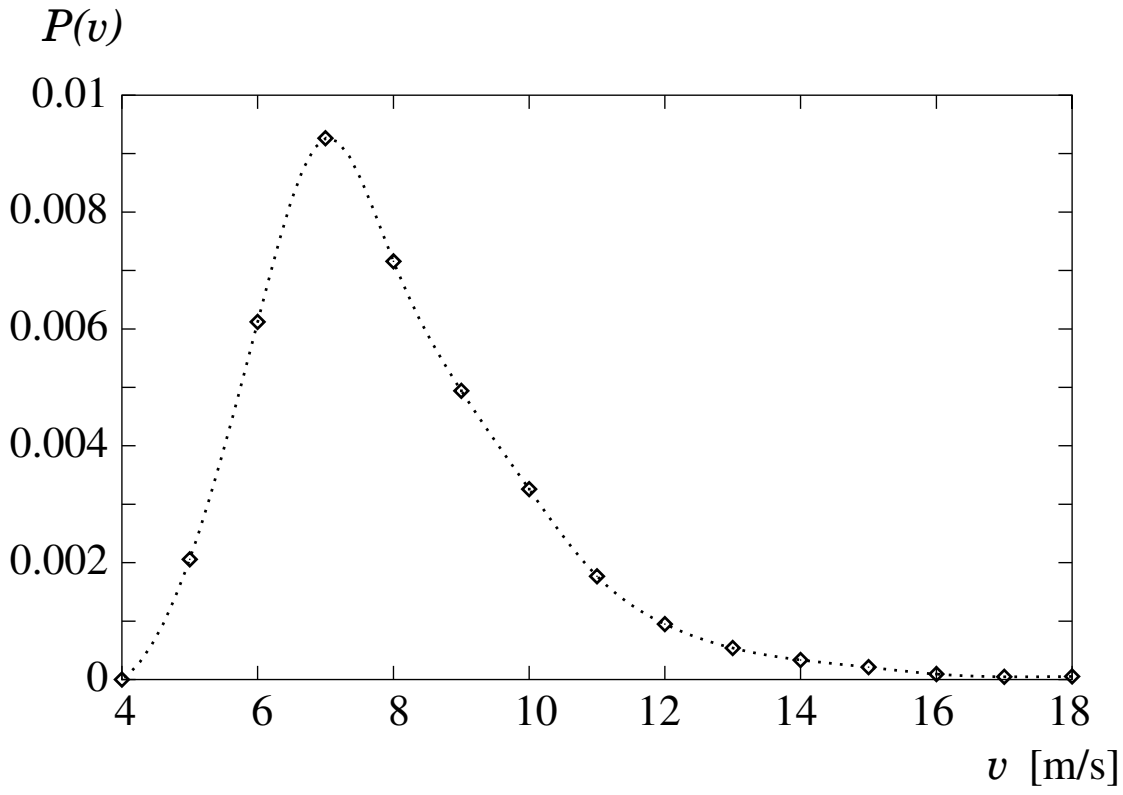

Figure 6.9: The product P(v) of the simulated efficiencies ε_{ext}, ε_{tra} (see Figure 6.8) and the velocity distribution $f(v)$ is displayed (see Eq.6.8) for the D_2 gas target at 24K as a function of neutron velocity *inside* the target. The normalization condition for $f(v)$ is explained in the text.

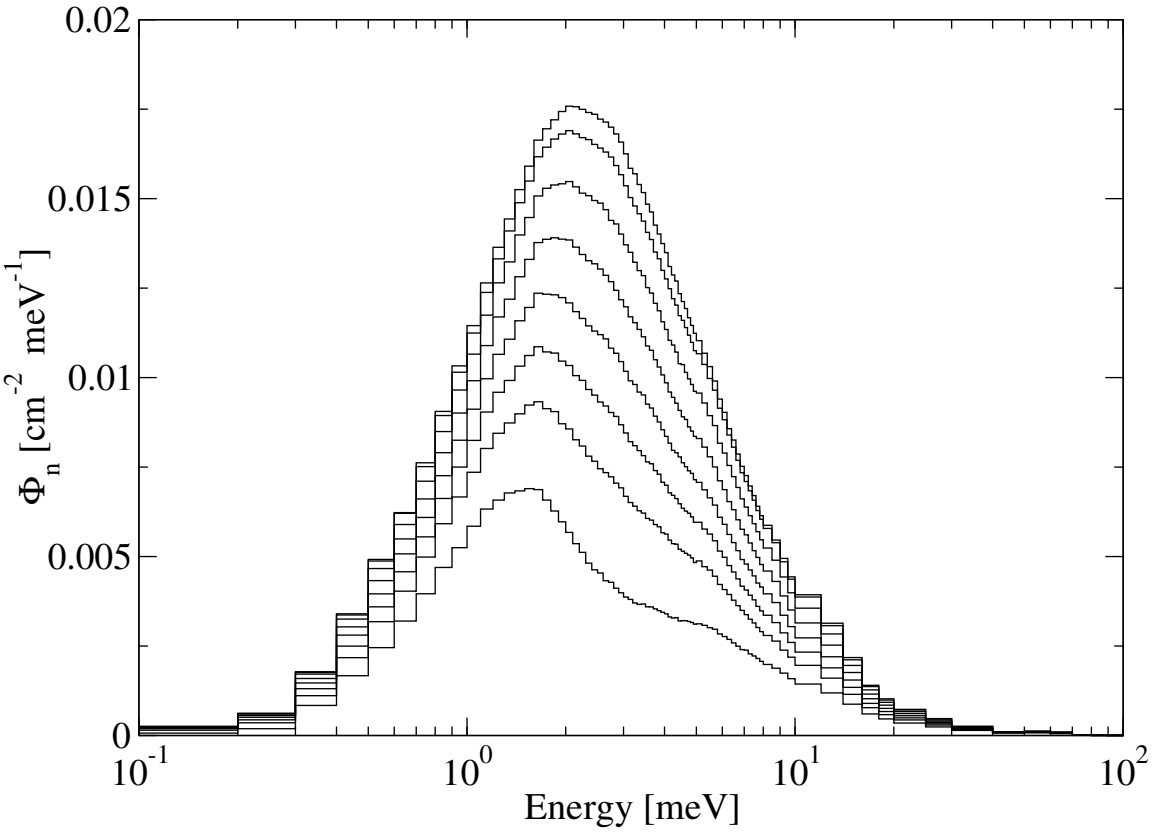

Figure 6.10: MCNPX [114] simulation by M. Wohlmuther of the attenuation and spectral change of the cold neutron flux per incident source particle in liquid D_2. The spectra displayed are averages over 10 mm diameter, 5 mm long cylinders on the beam axis. The intensity varies systematically with distance, with the highest values by the entrance window and the lowest by the UCN exit window. The simulation uses the IKE Stuttgart scattering kernel.[115]

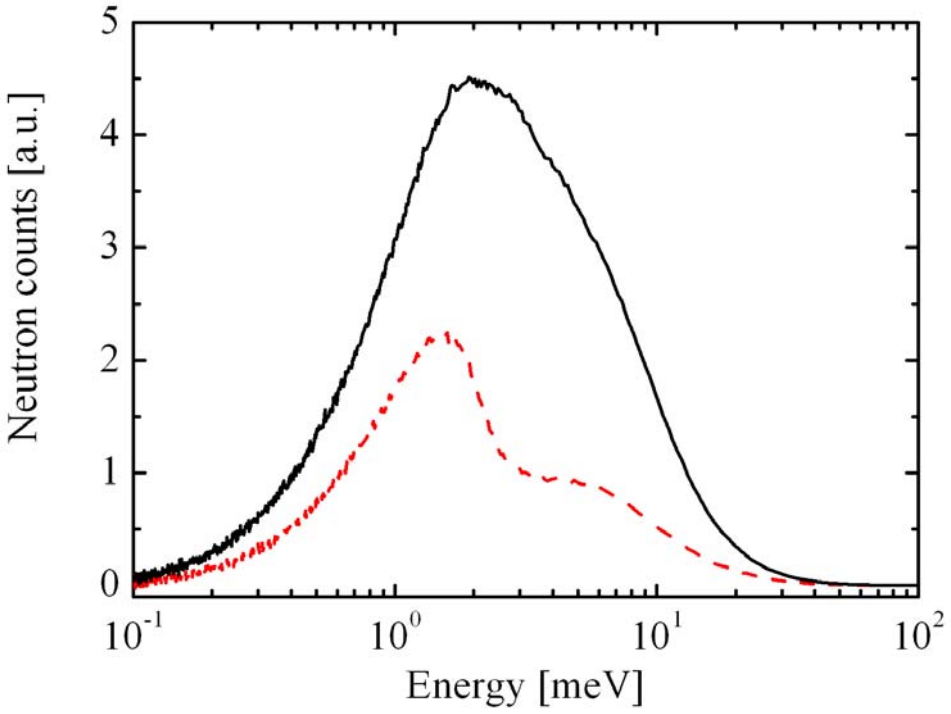

Figure 6.11: The measured CN transmission through an empty cell (black solid line) and liquid D_2 at 20 K. The attenuation and spectral change agrees with the MCNPX simulation (Fig. 6.10). The attenuation factor α_{att}^{exp} calculated by integrating the shown spectra is 0.67 $\pm$ 0.02 and agrees with the value obtained from the simulation.

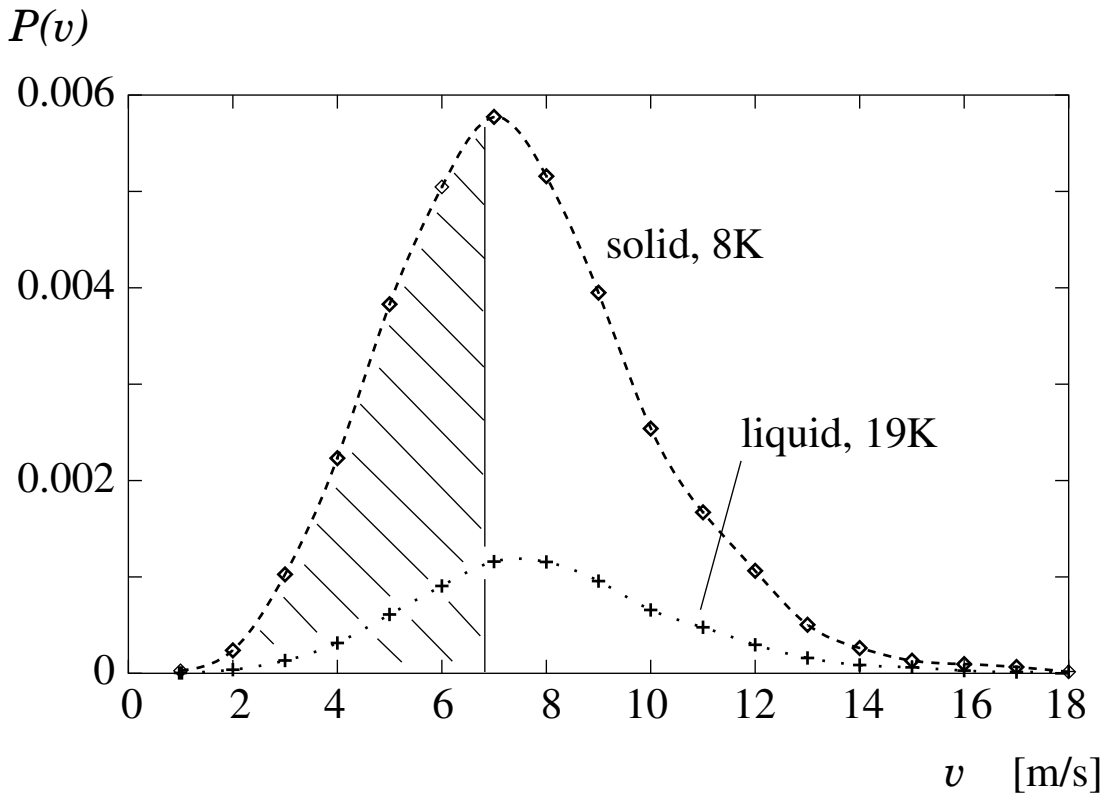

Figure 6.12: The product P(v) of the simulated efficiencies ε_{ext} and ε_{tra} and the velocity distribution $f(v)$ is displayed (see Eq. 6.8) for liquid and solid D_2. The different normalization conditions for $f(v)$ are explained in the text.

not strongly influenced by specific details of the crystal, and this should be the case when the average time the UCN spend in the D_2 before extraction becomes small in comparison with their lifetime in the solid. For solid D_2 at 8K used in the experiments, the estimated UCN lifetime is about 24 ms, dominated by thermal upscattering (40 ms lifetime), influenced by the para upscattering (about 100 ms) [110], and the neutron-deuteron absorption (150 ms). In our case, hydrogen contamination of the target was negligible. Neutrons with velocities of 5 m/s travel 12 cm in 24 ms, a distance larger than the target dimensions in our experiment. For solid D_2 at 8K under comparable conditions (e.g. 98 % ortho concentration), UCN lifetimes of about 20 ms have been measured [45].

It is instructive to compare our UCN production cross section, Eq. 6.17 with prediction [59, 60]. These calculations were performed using the incoherent approximation, single phonon exchange, and one of two models for the phonon spectrum, the Debye model (A) or a "realistic" spectrum (B) [60]. To make them comparable, the equilibrium UCN densities presented in [60] should be divided by the UCN lifetime due to absorption (150 ms) and by factor of 0.75 to remove their correction for the D_2 potential. We extract from [60] values for solid D_2 at 5K and for a Maxwellian neutron spectrum with $T_n \approx 25$ K (being not particularly sensitive to either and thus appropriate for a rough comparison with 8K and FUNSPIN):

$$\begin{aligned} R_A &= 1.1 \times 10^{-8} \ \ \mathrm{cm}^{-1} \\ R_B &= 1.3 \times 10^{-8} \ \ \mathrm{cm}^{-1}. \end{aligned} \tag{6.21}$$

Together with the authors of [60], one concludes that the specific form of the phonon spectrum is not of great importance for the UCN production (see however next section). They further argue that neglecting the influence of molecular effects in their treatment resulted in an average 20% overestimation of the cross sections. At the same time, the consideration of multiple phonon creation (see also next section) will raise the cross section by a similar amount. This suggests that our experimental result is in agreement with the predicted cross sections, even that based on the simple Debye spectrum.

The temperature dependence of the measured UCN current from solid D_2, see Figure 6.7, can in principle be treated within the same model and understood as the balance between the temperature dependence of thermal upscattering and UCN production. However, one finds that limiting the treatment of UCN production to the creation of only one single phonon does not properly describe the system. The inclusion of multiple phonon production in the downscattering process and, thus a temperature-dependent UCN source, leads to an agreement of the measured data and the simulation of extraction (see curve in Figure 6.7). The major significant temperature dependence in downscattering, in case of the FUNSPIN spectrum, is obtained already from the two-phonon creation. It is worth mentioning that almost the same curve is obtained by fitting a simple product of production and loss to the data with only one scale factor N_0 and one more parameter d for the mean UCN track length in the target:

$$N(T) = N_0 \frac{\sigma_{\mathrm{down}}(T)}{\sigma_{\mathrm{down}}(8K)} \exp\left[-\rho \sigma_{\mathrm{up}}(T) d\right]. \tag{6.22}$$

Here we calculate $\sigma_{\mathrm{up}}(T)$ in accordance with, e.g.[110], and $\sigma_{\mathrm{down}}(T)$ along the lines of [117], and obtain from the fit $d \approx 2$ cm for the path length, in agreement with the results from the simulation for the average UCN velocity of 7 m/s (see Figure 6.12).

It is important to note that the observed increase in extracted UCN between 20 and 8 K (see Figure 6.7) cannot directly be compared with the 'gain factors' as reported in [58, 65]. In the present experiment, the extraction of production cross sections is straightforward because the incoming cold neutron spectrum does not change significantly with target temperature, while the incoming spectrum is strongly affected in [58, 65] due to the sample being the cold moderator at the same time. Also, the geometries and sizes of the cold sources influence strongly the observed experimental gain as can be seen when comparing [58] and [65].

The results presented above for the UCN production are used for the prediction of the UCN density in the PSI source (see chapter 2).

6.2 Energy Dependent UCN Production in Deuterium

In order to improve the understanding of the underlying processes, we have measured the UCN production from gaseous and solid D_2 targets using a velocity selected CN beam. The measurements of the UCN rates were done in flow-through mode with a typical measurement time of 1000 s, and the UCN counts were normalized to the CN flux. Because of the good agreement between the theoretical expectation and the measurement of the absolute production cross sections (see section 6.1), here one can allow for an overall scale factor (different for gas and solid D_2) for UCN transport and detection efficiencies.

6.2.1 Theoretical Models

Gaseous D_2

The scattering of neutrons by the deuterium molecule was described in the chapter 5. There we have also shown the experimental validation of the YK and HS models. The same model is used to calculate the downscattering of CN into the energies of UCN. In order to compare the model with the measurements the cross section is calculated via

$$\sigma_{\mathrm{gas}}^{\mathrm{CN}\rightarrow\mathrm{UCN}} = \int dE_i \Phi(E_i) \int_{100\ \mathrm{neV}}^{350\ \mathrm{neV}} dE_f \frac{d\sigma_{\mathrm{YK}}}{dE_f}(E_i) \tag{6.23}$$

where the integration is done over the incoming CN energy spectrum $\Phi(E_i)$ (see Fig. 6.15) and the final UCN energies. The final energies have been set to the interval 100 - 350 neV, which is consistent with the energy range for neutrons in the gas that can be stored in the bottle at 1 m height.

Solid D_2

The downscattering of CN into UCN via phonon creation can be described by the same model as presented in chapter 5 while considering the upscattering of neutrons (see Fig-

ure 5.14). Here, however, we have to include the multiphonon contribution, since the neutron energies are high enough for this effect to become significant. The final cross section formula for downscattering, using 'incoherent approximation' and following [117] (compare also [61]) is:

$$\sigma(E_{CN} \rightarrow E_{UCN}) = \sigma_0 \sqrt{\frac{E_{UCN}}{ECN}} \exp\left(-\frac{E_{CN}+E_{UCN}}{\mu\tau}\right) \times \sum_{n=1}^{\infty} \frac{g_n(E_{CN}-E_{UCN})}{n!} \left(\frac{E_{CN}+E_{UCN}}{\mu}\right)^n \tag{6.24}$$

Because $E_{UCN} \ll E_{CN}$ one can use $\epsilon = E_{CN} - E_{UCN} \approx E_{CN} + E_{UCN} \approx E_{CN}$ in Eq. 6.24. We use, according to the 'incoherent approximation', the characteristic bound scattering cross section $\sigma_0 = 4\pi(b^2_{\text{coh}} + b^2_{\text{inc}}) = 7.63$ barn and the mass ratio of deuteron to neutron $\mu = \frac{m_d}{m_n}$. The term

$$\tau = \frac{\hbar^2}{2m_d\gamma} \tag{6.25}$$

is a characteristic energy[3] corresponding to the localization of a particle of a mass m_d in a region γ. The quantity

$$\gamma = \frac{\hbar^2}{2m_d} \int_0^{\infty} \frac{1}{\epsilon} \coth\left(\frac{\epsilon}{2k_BT}\right) Z(\epsilon) d\epsilon \tag{6.26}$$

is the average of the square displacement of D_2 in the lattice over the normalized phonon density of states $Z(\epsilon)$. The density of states can either be represented by a simple Debye spectrum

$$Z(\epsilon) = \frac{3\epsilon^2}{(k_B\theta_D)^3} \tag{6.27}$$

where θ_D is the Debye temperature, compare also with Eq. 5.57 and see Figure 6.13 or a more realistic phonon spectrum [60, 99] (see Figure 6.14). With

$$g(\epsilon) = \frac{Z(\epsilon)}{\epsilon(1-\exp\left(-\epsilon/(k_BT)\right))} \tag{6.28}$$

and $g_1(\epsilon) \equiv g(\epsilon)$, the multiphonon contributions are calculated via

$$g_n = \int_{-\infty}^{\infty} g_{n-1}(\epsilon') g(\epsilon - \epsilon') d\epsilon' \tag{6.29}$$

The final calculations are done according to

$$\sigma_{\text{solid}}^{\text{CN}\rightarrow\text{UCN}} = \int dE_i \Phi(E_i) \int_{0\text{ neV}}^{250\text{ neV}} dE_f \frac{d\sigma}{dE_f}(E_i) \tag{6.30}$$

The final energies have been set to the interval 0 - 250 neV, which is consistent with the energy range for neutrons in the solid D_2 that can be stored in the bottle at 1 m height.

[3] For an oscillator in the ground state $\tau = h\omega$

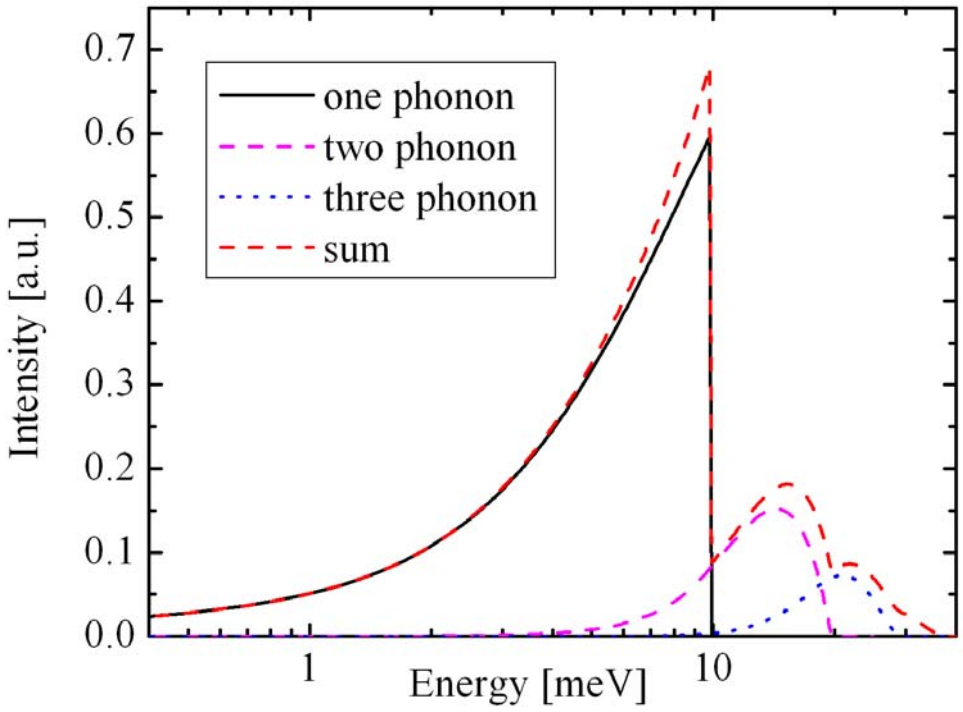

Figure 6.13: Density of states for sD_2 according to the simple Debye model.

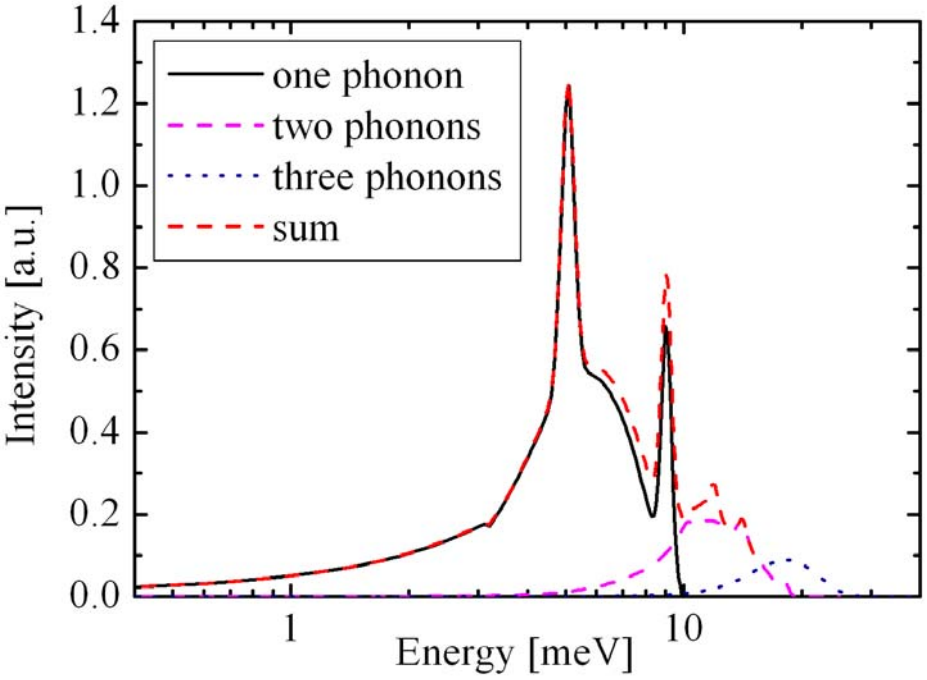

Figure 6.14: Realistic density of states for sD_2.

6.2.2 Data Analysis

In the case of the gas target, the extraction probability is independent on the CN energy and thus the measured UCN production cross section is

$$\sigma_{\text{gas, 25 K}} = \varepsilon_{\text{gas}} \frac{N_{\text{UCN}} - N_{\text{back}}}{v_{\text{CN}} \times N_{\text{CN}}} \tag{6.31}$$

where ε_{gas} is the overall scale factor for the gas target, N_{UCN} is the measured UCN rate per second, N_{back} is the background rate. The CN rate N_{CN}, measured simultaneously with the UCN rate (see Figure 6.15), is corrected for the $1/v_{\text{CN}}$ dependence of the CN detector (see Appendix B).

The situation is more complex for solid D_2: the shape of the UCN energy spectrum at the instant of production does not depend on CN energy, but the spatial distribution of CN interactions and, thus, of the UCN production does; this leads to a CN energy dependent UCN extraction efficiency. Relative energy dependent corrections have been determined by modeling the UCN extraction from the target cell, starting the UCN according to calculated axial flux distributions which are consistent with the measured CN total cross sections (the average of the cross sections for two different crystals see Figure 5.6). We divide the target cell into 5 mm long cylinders on the beam axis. For each cylinder the CN intensity is calculated according to the formula:

$$N_{\text{CN}_i}(E_{CN}) = N_{\text{CN}}(E_{\text{CN}}) \exp\left(\rho \sigma_{\text{av}}(E_{\text{CN}}) l_i\right) \tag{6.32}$$

where $\text{N}_{\text{CN}}(E_{\text{CN}})$ is the CN transmission measured simultaneously with the UCN rate (see Figure 6.16) and l_i is the distance from the middle of the cylinder to the end of the cell. The total cross section $\sigma_{\text{av}}(E_{\text{CN}})$ is the average cross section for CN for two different crystals measured without the velocity selector (see Figure 5.6). The variation of the measured total cross section for different crystals causes the dominant uncertainty in the modeling, and makes a significant contribution to the cross section error.
The measured UCN production cross section is:

$$\sigma_{\text{solid, 8 K}} = \varepsilon_{\text{solid}} \frac{N_{\text{UCN}} - N_{\text{back}}}{v_{\text{CN}} \times \sum_{i=1}^{8} N_{\text{CN}_i} \Omega_i} \tag{6.33}$$

where Ω_i is a solid angle for each cylinder. The background rate N_{back}, within statistical limits, was independent of VS settings and not affected by small variation in the proton beam current (as this was very stable while taking data, 1252 ± 3 μA) . With the proton beam and the CN beam on the D_2 target, the background rate was (0.0054 ± 0.0003) s^{-1}, as measured with one or both UCN shutters closed. The background without proton beam was less than 0.003 s^{-1}. Typical UCN count rates with UCN shutters open were in the region 0.01 to 0.06 s^{-1}.

A final normalization was performed in which a constant factor[4] that minimized the mean square deviation between the cross section model and the measured results was applied to the data. The cross section values are shown in Figure 6.15 for gaseous ortho-D_2 (c_0

[4]The overall scale factor $\varepsilon_{\text{solid}}$ or ε_{gas}

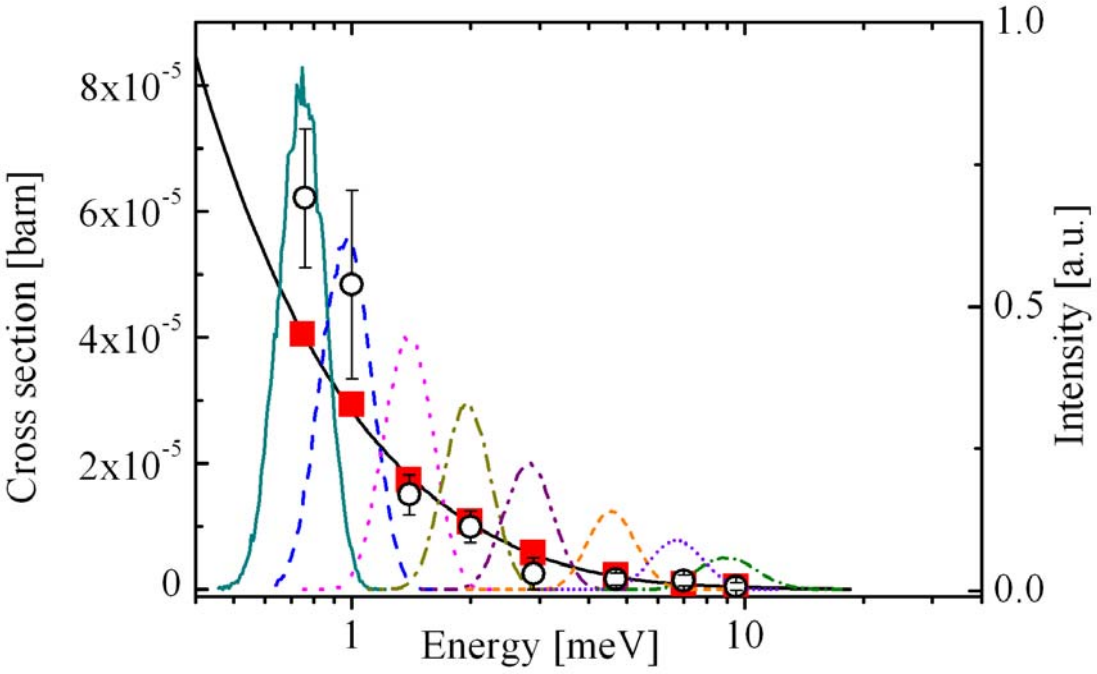

Figure 6.15: Scaled measured (open circles) and calculated UCN production cross sections per molecule versus the CN energy (Young and Koppel model: continuous black line and red squares, see text) for gaseous ortho-D_2 at 0.12 MPa and 25 K. The velocity selected CN intensity distributions are normalized to the same intensity.

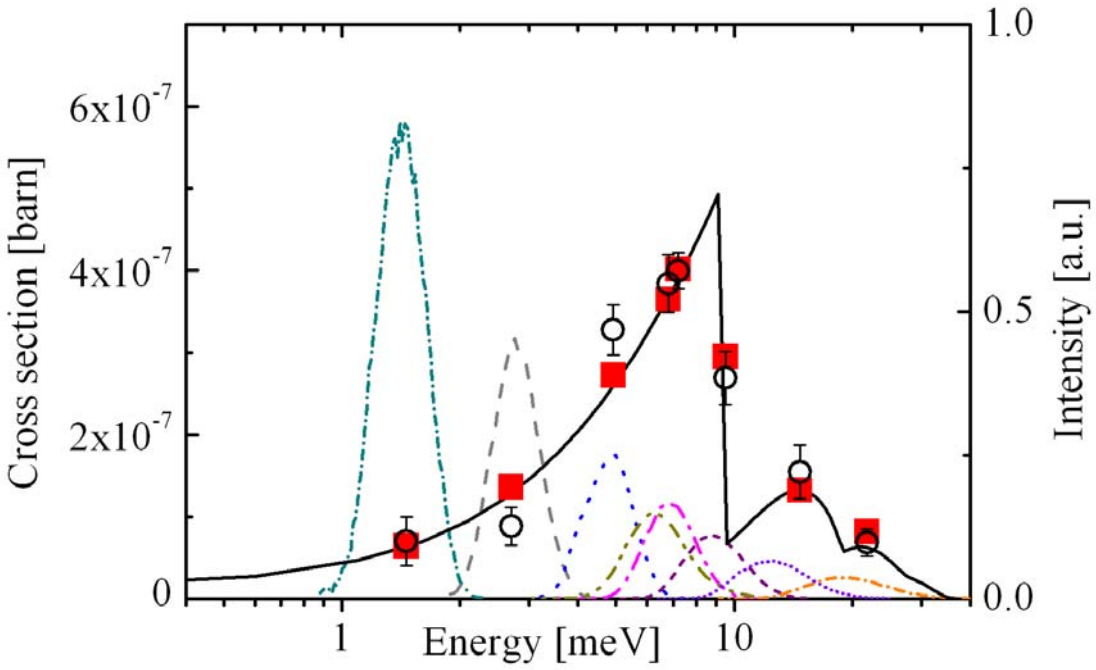

Figure 6.16: Scaled measured (open circles) and calculated UCN production cross sections per molecule versus the CN energy (multiphonon Debye model: continuous black line and red squares, see text) for solid ortho-D_2 at 8 K. The velocity selected CN intensity distributions are normalized to the same intensity.

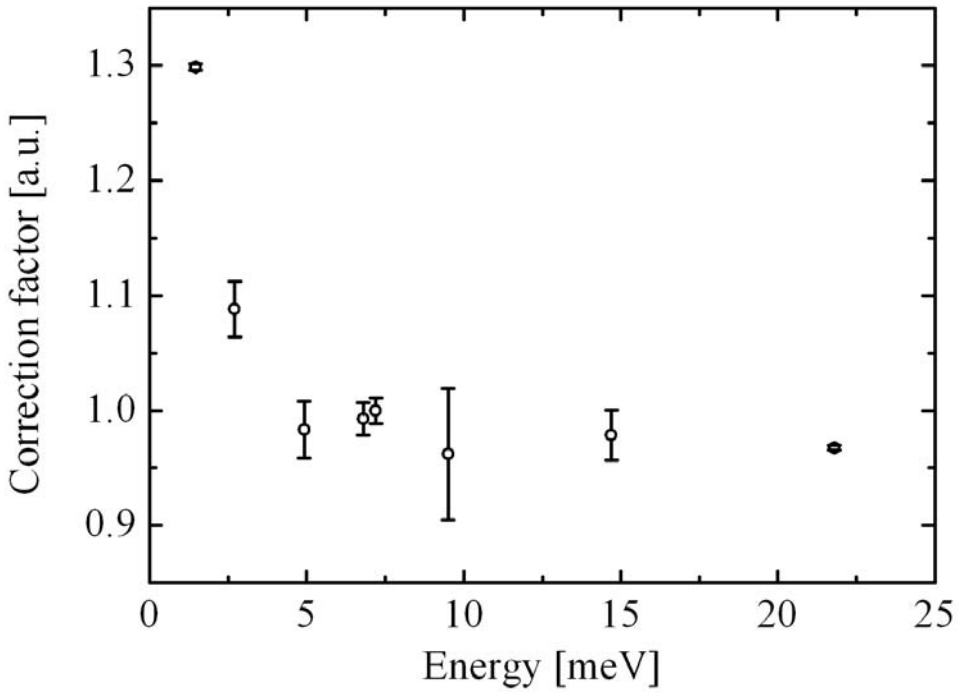

Figure 6.17: The calculated energy dependent correction factors for the CN energy bins. These factors are applied to the data to correct for the CN energy dependent extraction efficiency. The overall scale factor is not included in this graph since it is the same for all CN energy bins. The large uncertainty at 9 meV comes from the variation in the total cross sections for CN transmission due to different Bragg scattering patterns (see text and Figure 5.6).

≈ 0.98) at 25 K and a pressure of 0.12 MPa and in Figure 6.16 for solid ortho-D_2 at 8 K (in equilibrium with its saturated vapor pressure in the gas system above the target). For each data point the normalized velocity-selected CN spectrum is displayed on the CN energy axis. Along with the data, the model calculations are shown as continuous function of CN energy (black line) and averaged over the velocity-selected CN spectra (red squares), respectively.

For the gas measurement the fit of the 8 data points to the Y-K model results in $\chi^2 = 8.54$ for 7 degrees of freedom ($\chi^2_{\mathrm{red}} = 1.22$), confirming the proper understanding of the UCN production in gaseous D_2, a reasonable control of the systematic effects in the experiment, and the statistical origin of deviations between the model and the data. Qualitatively, the energy dependence is easy to understand: The CN require D_2 molecules of a certain velocity class in direction of the CN beam for the downscattering. As the Maxwell-Boltzmann distribution peaks at zero for any velocity component, there will always be more molecules available to downscatter CN of lower energy.

The fit to the data of solid D_2 to the simple Debye model results in $\chi^2 = 9.73$ for 7 degrees of freedom ($\chi^2_{\mathrm{red}} = 1.39$). Qualitatively, one again understands that the energy dependence follows the final state density of the phonons in the solid. Interestingly, the fit gets considerably worse when using the 'more realistic' phonon density of states of [60, 99] (see Figure 6.14). It is, however, difficult to draw final conclusions from this discrepancy because of some systematic issues which are difficult to estimate, particularly differences between the crystals in the Bragg region, the validity of the 'incoherent approximation', and also the influence of the molecular effects. These issues have been recently discussed [118] in connection with a new recent measurements of the phonon density of states in solid D_2 [119]. Nevertheless, we would like to emphasize the good agreement of the data and the Debye model in Figure 6.16. In particular, the UCN production above 10 meV provides strong evidence for two- and three-phonon contributions.

6.3 UCN Production in Different Converters

We have investigated the UCN production in three materials: deuterium (D_2), oxygen (O_2), and heavy methane (CD_4). All the measurements were done with the same setup configuration (see chapter 4 and Figure 4.1), at the same CN beam line in the flow-through mode, and took one week for each substance. During this period the produced UCN and transmitted CN have been detected for gaseous, liquid, and solid phases of D_2, O_2, and CD_4 at various temperatures. The information about temperatures of phase transitions have been collected in Table 6.3. Below the data analysis and interpretation of the obtained results are presented.

The data analysis follows the method used in section 6.1.2 with some modification due to e.g. different way of normalization; during these measurement we could simultaneously detect the CN counts along with the UCN. To determine the UCN production rates I_{meas} in the sample, the number of detected UCN N_{UCN} is normalized to the simultaneously

Table 6.3: Temperatures of phase transitions in D_2, O_2 and CD_4

	D_2	CD_4	O_2
Boiling point	23.5 K	112 K	90.2 K
Melting point	18.5 K	89.9 K	54.8 K
Solid Phases		27.1 K < I < 89.9 K 27.1 K < II < 22.1 K III < 22.1 K	43.8 K < γ < 54.4 K 23.9 K < β < 43.8 K α < 23.9 K

measured transmitted CN counts N_{CN}:

$$I_{\mathrm{meas}} = \frac{N_{\mathrm{UCN}} - N_{\mathrm{back}}}{N_{CN}} \tag{6.34}$$

where N_{back} is the background rate. The rates I_{meas} are shown in Figure 6.18 for D_2, CD_4, and O_2 as a function of temperature. The rates I_{meas} are the convolution of : (i) the downscattering cross section in the material $\sigma^{\mathrm{CN}\rightarrow\mathrm{UCN}}$, (ii) the extraction efficiency $\varepsilon_{\mathrm{ext}}$, (iii) the transport efficiency $\varepsilon_{\mathrm{trans}}$ which can be determined from the simulation. Since here the intention is to compare the UCN production rates in the samples, there is no need to determine the UCN production cross sections as was done in section 6.1.2. However, we have to take into account various transport efficiencies of the UCN spectrometer due to different Fermi potentials of the investigated solids[5]. The efficiencies $\varepsilon_{\mathrm{trans}}$ are obtained by simulation calculations carried out using the GEANT4 UCN-Monte Carlo code [112], which tracks UCN through a detailed model the UCN spectrometer system. The extraction efficiencies $\varepsilon_{\mathrm{ext}}$ may also differ due to various UCN lifetimes in the investigated materials. Here we assume that these efficiencies are the same. This assumption is based on the fact that the UCN extraction in case of solid D_2 is not influenced by specific details of the crystal but by the UCN lifetime in sD_2which is dominated by thermal upscattering. One can conclude that this will be also the case for sCD_4 and sO_2. The capture contribution for sO_2 is negligible, and for sCD_4, it is influenced by the neutron-deuteron absorption as for sD_2. The upscattering coming from rotational excitations will also influence the UCN lifetime, especially in CD_4, since the energy levels are much lower than for D_2. However, at low temperatures around 8 K, this contribution should be comparable with the thermal

[5]For the gaseous phases of D_2, CD_4, and O_2 the effect of the Fermi potential and thus the difference in transport efficiencies is negligible since for all three gases the Fermi potential is smaller than 1 neV

upscattering. The remaining question is how large should the thermal upscattering be in order to influence the extraction. The target dimension in our experiment is 4 cm; to travel this distance, the neutrons with velocity of 5 m/s need 8 ms. This means that only in case of UCN lifetime lower then 8 ms i.e. the thermal upscattering 5 times stronger than for sD_2, the extraction efficiency would be different in the geometry of our experiments. Certainly the measurements of UCN lifetime in solid CD_4 and O_2 would be helpful for the comparison between the converter materials, but since now there are no data available, the assumption made above seems reasonable.

Taking into account the arguments discussed above, we correct the measured UCN production rates I_{meas} for the transport efficiencies. We introduce the function $T(v)$ to include the dependence of the average UCN production cross section $\bar{\sigma}(v_f)$ on the final neutron velocity v_f, $\bar{\sigma}(v_f) = \bar{\sigma}^{\mathrm{CN}\to\mathrm{UCN}} f(v)$ where, $f(v) \sim v^2$, so that:

$$T(v) = f(v)\varepsilon_{\mathrm{trans}} \tag{6.35}$$

with the normalization condition (see also Eq. 6.9)

$$\int_{v_1}^{v_2} f(v)dv = 1 \tag{6.36}$$

where v_1 and v_2 are the velocities *in* the target material that lead to UCN storable in the bottle (0-250 neV). The distributions $T(v)$ for solid D_2, CD_4 and O_2 are shown in Figure 6.19. To calculate the correction factors, functions $T(v)$ are integrated over the neutron velocity range that contributes to the UCN stored in the bottle. For solid D_2 the neutron velocity lies in the velocity range 0 to 6.8 m/s (corresponding to the energy range 0-250 neV) and

$$T(v)^{\mathrm{sD_2}}_{\mathrm{int}} = \int_0^{6.8\ \mathrm{m/s}} T(v)^{\mathrm{sD_2}} dv = 0.039 \tag{6.37}$$

In case of solid CD_4 with the Fermi potential V_F of 177 neV[6] the corresponding neutron velocity range is 0 to 5.8 m/s (energy range 0-173 neV):

$$T(v)^{\mathrm{sCD_4}}_{\mathrm{int}} = \int_0^{5.8\ \mathrm{m/s}} T(v)^{\mathrm{sCD_4}} dv = 0.031 \tag{6.38}$$

Solid O_2 has $V_F = 87$ neV[7] and thus the velocity range is 1.6 to 7.1 m/s (energy range 13-263 neV):

$$T(v)^{\mathrm{sO_2}}_{\mathrm{int}} = \int_{1.6\ \mathrm{m/s}}^{7.1\ \mathrm{m/s}} T(v)^{\mathrm{sO_2}} dv = 0.041 \tag{6.39}$$

The corrected UCN rates I_{corr} are calculated using:

$$I_{\mathrm{corr}} = \frac{I_{\mathrm{meas}}}{T(v)_{\mathrm{int}}}. \tag{6.40}$$

and are shown in Figure 6.20 and for 8 K solids collected in Table 6.4.

[6]The value of V_F for sCD_4 varies with the temperature, sCD_4 at 64 K has $V_F = 166$ neV, at 8 K $V_F = 177$ neV

[7]Also for sO_2 V_F varies from 79 neV (45 K) to 87 neV (8 K)

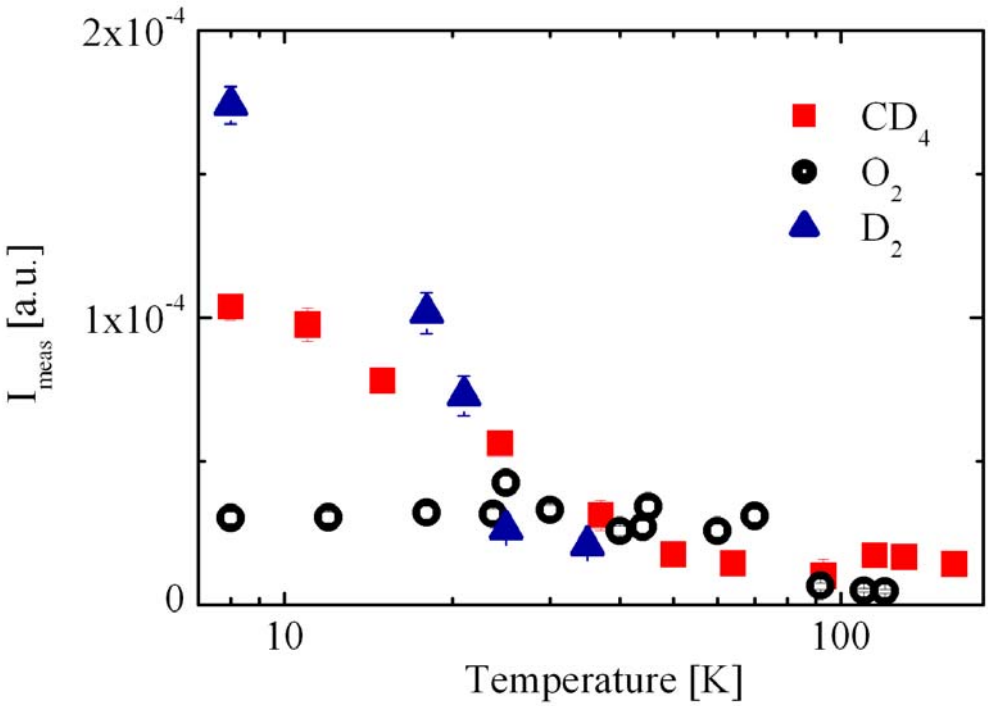

Figure 6.18: The measured UCN production rates I_{meas} for D_2, O_2 and CD_4. These rates are the detected UCN background corrected and normalized to the simultaneously detected, transmitted through the sample CN.

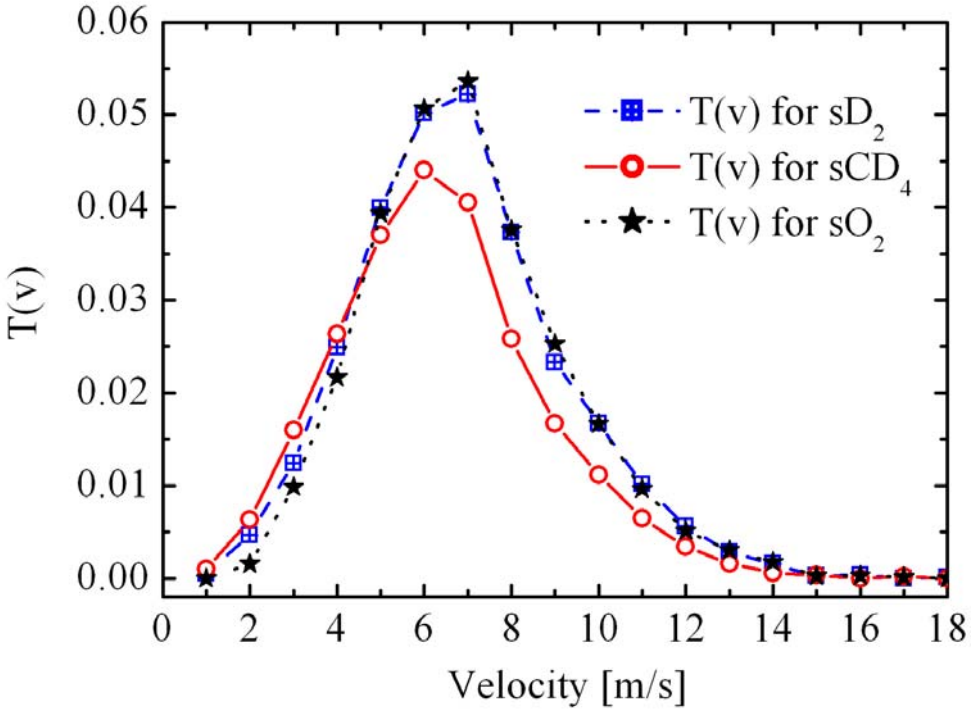

Figure 6.19: The simulated transport efficiencies for solid D_2, O_2 and CD_4. The simulation takes into account the Fermi potential of the materials.

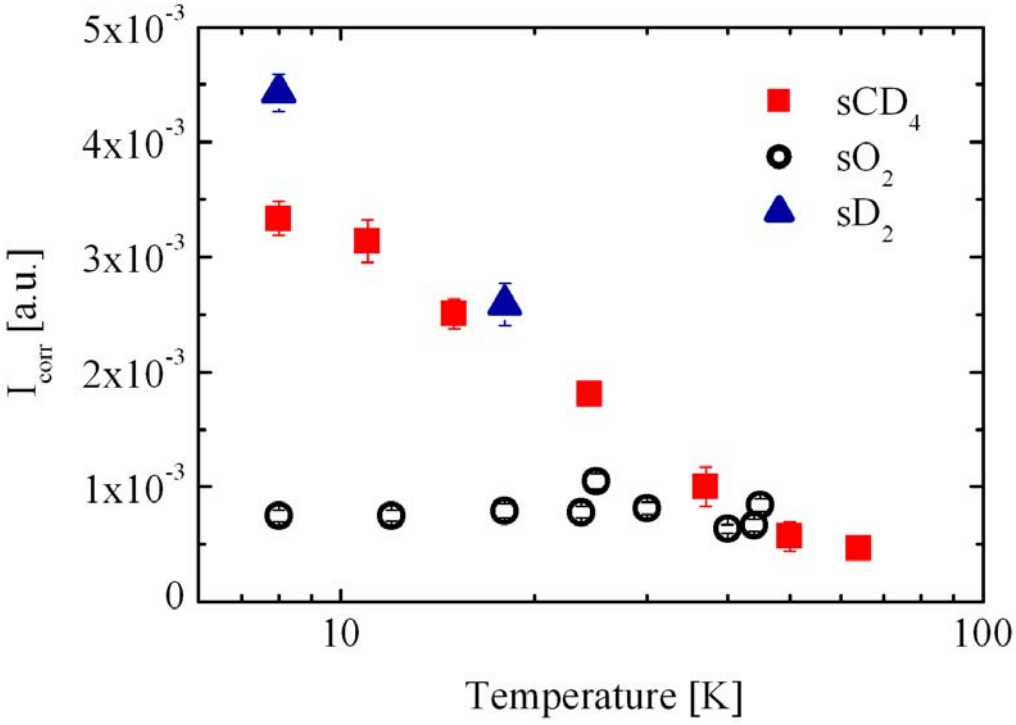

Figure 6.20: The UCN production rates I_{corr} for solid D_2, solid O_2 and solid CD_4. These rates are the corrected for the transport efficiency (see Figure 6.19) measured UCN rates I_{meas}. The assumption made here is that the UCN extraction efficiencies are the same for all three materials.

Table 6.4: UCN production rates I_{corr} for solid D_2, O_2 and CD_4, corrected for the transport efficiency.

Material	Temperature	UCN production rate I_{corr} [au]
D_2	8 K	0.0044 ± 0.0002
CD_4	8 K	0.0033 ± 0.0002
O_2	8 K	0.0007 ± 0.0001

Chapter 7

Conclusions

7.1 Overview

The main aim of the work presented in this thesis was to understand the physics of UCN production for the purpose of providing high UCN fluxes required for improving the sensitivity of fundamental physics experiments such as the search for the electric dipole moment of the neutron. In the first chapter we have given the motivation for building high intensity UCN sources, namely the search for physics beyond the Standard Model with ultracold neutrons. The short overview of the problem of matter - antimatter asymmetry and the aspects of time reversal symmetry violation in connection with the electric dipole moment of the neutron have been explained. Later we presented the principles of the new high intensity UCN source under construction at PSI and the basic model of the neutron moderation. Afterwards the details of the setup used for the UCN production experiments and the principle of the measurements were described. In the next chapter the theoretical models describing the interactions of a neutron with a medium (molecule or crystal lattice) were discussed and verified by the measured total neutron cross sections. At the end the experimental data of UCN production from a CN beam using D_2, CD_4, and O_2 targets were shown and interpreted.

Two UCN production experiments based on the same concept of measuring UCN produced from a CN beam were performed. Both experiments were carried out at the Swiss Spallation Neutron Source SINQ at PSI, using the polarized CN beamline for fundamental physics FUNSPIN.

The first experiment took 10 days of beam time and we have successfully measured the absolute UCN production cross sections in gaseous, liquid, and solid D_2 [2] and the temperature dependence of the UCN production in sD_2. Additionally the polarization of UCN produced from polarized CN in sD_2 was measured (see appendix A) .

The second experiment was conducted in autumn 2005 at the same beamline. During 5 weeks of beam time we have measured the production of UCN from the CN beam in D_2, O_2, and CD_4 as well as the CN transmission through all three materials [3]. Moreover, in order to understand underlying processes of UCN production in gaseous and solid D_2, the CN energy dependent UCN production was measured [4].

Below a short summary of the results obtained is presented.

7.2 Absolute Production Cross Sections in D_2

The results of the first UCN production experiment using D_2 as a target for a cold neutron beam have been presented. The UCN were produced, stored, and detected. The background level in the experiments was sufficiently low as to also allow detecting the neutrons without storage. UCN signal-to-background ratios of up to 40:1 were obtained with 5% statistical accuracy in measurements lasting less than 1/2 h, depending on the conditions of the target.

From the measured UCN production rates, the absolute UCN production cross sections for gaseous, liquid, and solid D_2 have been extracted. The comparison of the measured and calculated UCN production in gaseous D_2 was used to calibrate the simulated target extraction and transport efficiencies of the experimental apparatus. To calculate the UCN production in gaseous D_2, the Young and Koppel model[1] was applied. Absolute production cross sections for solid and liquid D_2 have been extracted from the data. The value for low-temperature solid D_2 agreed with the cross section calculated using the simple Debye model and the 'incoherent approximation'. The temperature dependence of the measured UCN rate can be understood in terms of the variations in balance between the actual production (including multiphonon excitation) and thermal upscattering. In previous UCN production experiments [65, 45, 66], the incoming neutron spectra were not known in detail. Consistent results were obtained by combining calculated cold neutron spectra and UCN production models along the lines of [59, 60, 117] and as discussed in chapter 5 . These results validate the UCN production cross sections. Based on this the UCN density prediction for the new high-intensity UCN source at PSI can be made (see chapter 2).

7.3 Energy Dependent UCN Production in D_2

These data were taken during the second UCN production experiment using a velocity selected cold neutron beam to investigate the influence of the incident neutron energy on UCN production.

We have shown that the YK model can be applied to describe the measured energy dependence of UCN production for gaseous D_2. Additionally, the qualitative understanding of the energy dependence which takes into account the Maxwell-Boltzmann distribution of the neutron velocity components have been presented.

The shape of the CN energy dependent UCN production for solid D_2 can be explained by the simple Debye model. In particular, the UCN production above 10 meV provides strong evidence for two- and three-phonon contributions. Qualitatively one again understands that the energy dependence follows the final state density of the phonons in the solid.

[1] The validity of this model was verified by the total neutron cross section measurements in gaseous D_2.

7.4 UCN Production in D_2, O_2, and CD_4

The measurements of the UCN production rates from a CN beam using D_2, O_2, and CD_4 targets have been done in the flow-through mode during a second experiment. The results obtained show that the UCN production rates are the highest for solid D_2 at 8 K. The UCN production rate for solid CD_4 is about 33 % lower than the one for sD_2 and for solid O_2 at 8 K the rate is 6 times smaller. The very low UCN production rate for solid O_2 might be explained by the lack of magnetic structure in the crystals grown. In this case, the only possible channel for UCN production would be via phonon excitations. Comparing the calculated UCN densities produced in sD_2 and sO_2 (see Figure 7 in [71]), one can notice that the UCN density in sO_2 without magnon excitations is about 6-7 times lower than for sD_2.

7.5 Cold Neutron Total Cross Sections

The interest in developing new high intensity UCN sources requires experimental data relevant to characterize the neutron thermalization process like total cross sections. The measured CN total cross sections for D_2, O_2, and CD_4 in various phases have been presented. The neutron total cross sections were determined from the neutron beam attenuation in the measured samples. The results have been interpreted in terms of neutron scattering theory. For all three substances we have observed coherent scattering arising from the crystal lattice structure, i.e. Bragg scattering.These data can be of great use for improving the scattering kernels for cryogenic materials of interest as cold and ultracold neutron moderators.

The comparison between the data and theory for solid D_2 indicates that the grown samples have been in an intermediate state between random and oriented polycrystal. According to the measurements, the orientation of polycrystalline structure of grown solid D_2 at 18 K gets destroyed while cooling down to 8 K, however some orientation still remains. Even the samples grown from the gaseous phase are not random polycrystals. The data also show that it is difficult to grow identical crystals, i.e. with the same Bragg scattering pattern, even under very similar conditions. The average total cross section, however, is not particularly sensitive to the crystal structure.

For solid CD_4 we have observed no change in the shape of the total cross section curves, in the Bragg region, between three solid phases at low temperatures. This is in agreement with the crystallographic data i.e. all three phases have similar lattice constants. The fact that the cross section doesn't change with lowering temperature might indicate that the sCD_4 sample obtained at 28 K was a random polycrystal. On the other hand, the comparison between the data and theoretical calculation shows a discrepancy between the expected and measured Bragg cut-off, which could suggest some very specific orientation of the crystal that is not sensitive to the temperature changes.

In contrast to solid CD_4, for solid O_2 we have observed the change in the cross section shape with the phase change. Those observations could be explained by the different crystal structures and thus different lattice parameters of α-, β-, γ-phases of solid oxygen. Above the Bragg cut-off wavelength the cross section at low temperatures tends to 0, which is in

agreement with the fact that oxygen (^{16}O) has no incoherent cross section.

Appendix A

UCN polarization

During the experiments on UCN production from polarized cold neutrons on a solid ortho-D_2 target at FUNSPIN we investigated the conservation of polarization. As a result of the first experiment [120], the polarization value of UCN is found to be consistent with full conservation of the intital polarization. However, the second experiment did not confirm those results, probably due to the spin flippers fault. Here the results from the first experiment are presented and described.

In order to measure the conservation of the polarization, we have used two radio-frequency spin flippers (SF) which are integral part of FUNSPIN. We denote the UCN count rate N_{00} in case both SF are off, N_{11} in case both are on and N_{01}, and N_{10} accordingly when one SF is on and the other one off. The wavelength averaged cold neutron polarization of the beam region used was about 95 % [78]. The initial polarization vector of the beam is vertical and was turned adiabatically into the horizontal beam axis direction. Magnetic fields along the axis guided the neutron spins until the UCN polarization was analyzed using a magnetized mirror (10 cm diameter Si wafer with 110 nm Fe sputtered onto it). An arrangement of permanent magnets and a return yoke on the back of the mirror allowed it to be fully magnetized in its central region, with some imperfections at the edges. This was checked using the polarization option of the neutron reflectometer AMOR at SINQ [121]. Figure A.1 shows the flow-through count rate of the UCN detector for different SF configurations. The data for different SF states but same spin configurations are consistent and can be added, e.g. $N_{00,11} = N_{00} + N_{11}$. We extract a temperature independent count rate asymmetry:

$$(N_{00,11} - N_{01,10})/(N_{00,11} + N_{01,10}) = 10.24 \pm 0.48\% \tag{A.1}$$

This value should be compared with the one expected for full polarization. In Figure A.2 we show the result of a simulation of the probability for UCN of a given velocity and spin state to be transported from the target to the detector. The integral asymmetry depends on the, apriori not known, velocity spectrum of the UCN escaping the D_2 target. Assuming a spectrum $\propto v^2$ (like a Maxwellian density spectrum) leads to an asymmetry of 8.7%, for $\propto v^3$ (like a Maxwellian flux spectrum) one obtains 11.0%. Both, the rather low analyzing power and the yet unknown UCN velocity distribution prohibit a strong

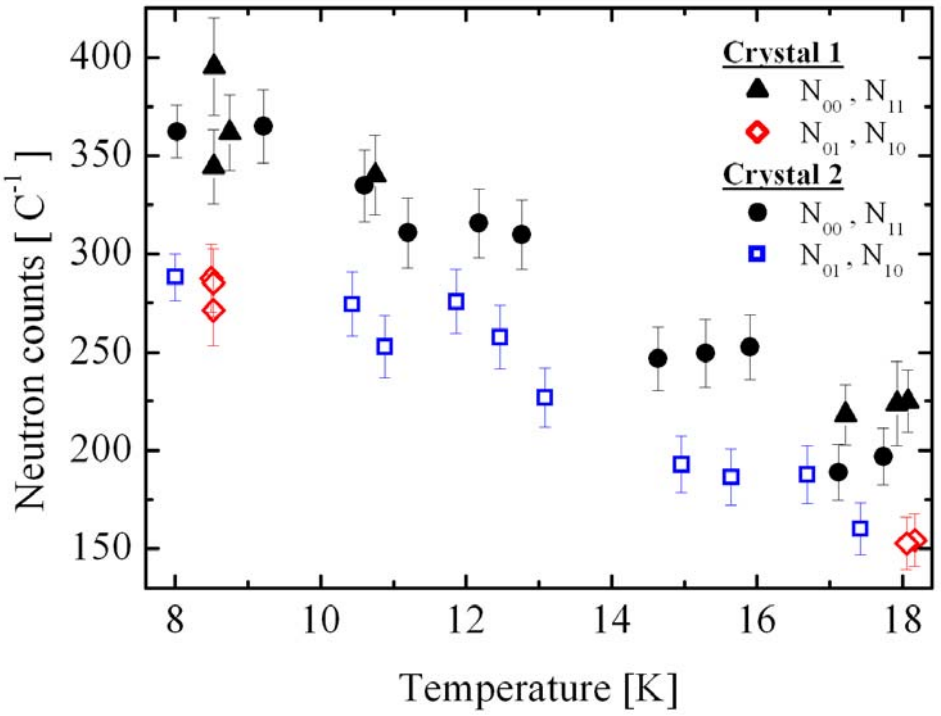

Figure A.1: The UCN count rate as a function of D_2 temperature for different configurations of the two RF spin flippers as measured for two different sD_2 crystals.

quantitative statement to be made based on these results. However, for realistic simulation of the given setup it is hardly possible to reproduce larger asymmetries. This points to very high UCN polarizations, at this point, clearly consistent with the initial cold neutron polarization and little or no depolarization.

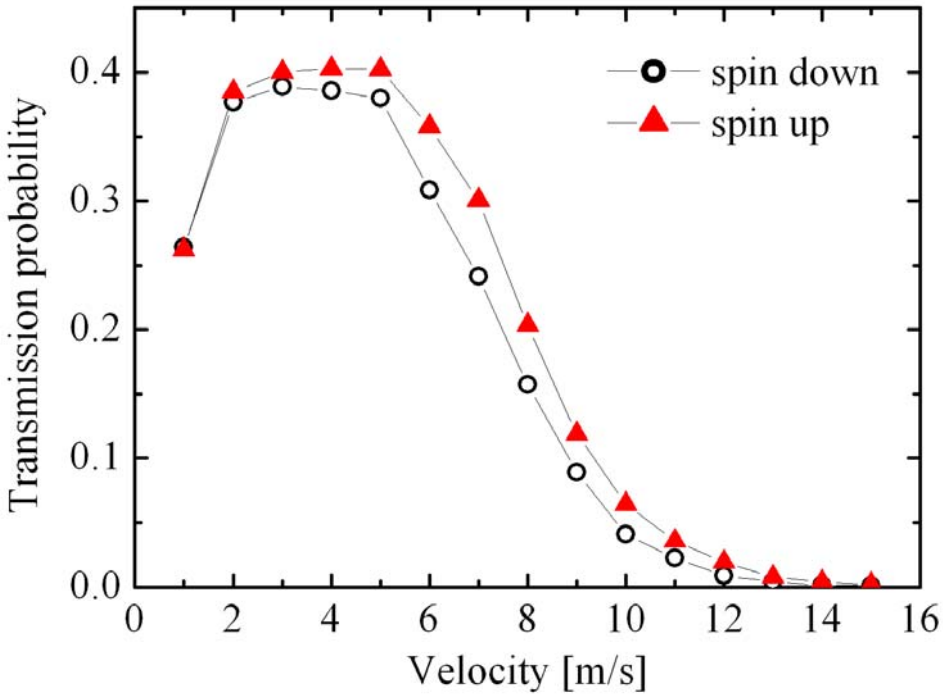

Figure A.2: The simulated UCN transmission probability as a function of velocity and spin direction.

Appendix B

Systematic Effects and Detector Calibration

The time of flight spectra were taken for the full CN beam and during the measurements with velocity selector (see 4.1.6). The sample CN spectra as a function of neutron energy are shown in Figure B.1.

B.1 Cold Neutron Flux Measurements

The integrated CN flux incident on the target cell, for the full and velocity selected CN beams, was determined by the gold foil activation method i.e. by using the reaction ^{197}Au (n,γ)^{198}Au. The gold foils, of a diameter of 20 mm, were placed on the cryostat, on the neutron beam entrance side (see Figure B.2), behind the velocity selector and irradiated for a period of 200 s. After few days, 411 keV γ-ray activity A induced by irradiation was measured on a HpGe γ detector system.

The netron flux ϕ per mA can be calculated using:

$$\phi = \frac{A}{\sigma(v)\ N_{\mathrm{Au}}\ \lambda_{\mathrm{Au}}\ \int I_p dt} \tag{B.1}$$

where $\sigma(v)$ is the cross section of ^{197}Au for CN capture, which in the cold neutrons energy range follows a $1/v$ law:

$$\sigma(v) = \frac{v_{th}\sigma_{th}}{v} \tag{B.2}$$

where v_{th} = 2200 m/s and σ_{th} = 98.65 b are, respectively, the thermal neutron velocity and absorption cross section. N_{Au} is the number of Au atoms, which is calculated from the known mass of the Au foils, and λ is the decay constant of ^{198}Au:

$$\lambda = \frac{ln\ 2}{T_{1/2}} \tag{B.3}$$

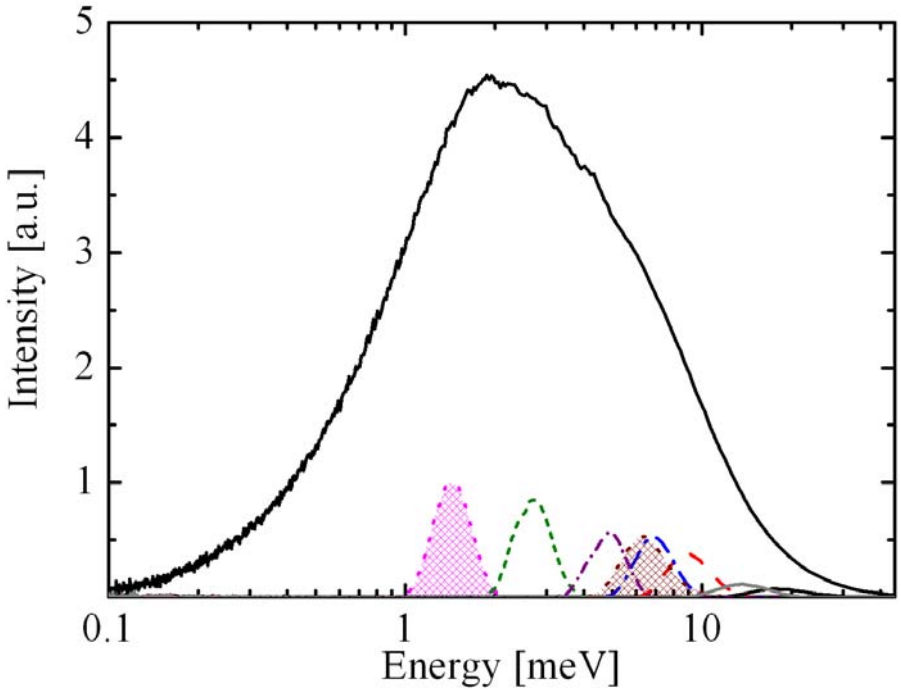

Figure B.1: Detector efficiency and proton beam charge corrected CN spectra at FUNSPIN. The full range spectrum was measured without velocity selector (VS) and show the transmission of the empty target (solid black line). The other energy distributions were obtained for various VS settings and normalized as the other spectrum. The CN flux was measured with Au foil activation and is (4.6 ± 0.5) x 10^7 $cm^{-2}mA^{-1}s^{-1}$ for the full spectrum. For the shaded spectra at 1.4 meV and 6.3 meV the measured flux is (1.7 ± 0.2) x 10^6 $cm^{-2}mA^{-1}s^{-1}$ and (4.4 ± 0.4) x 10^6 $cm^{-2}mA^{-1}s^{-1}$, respectively.

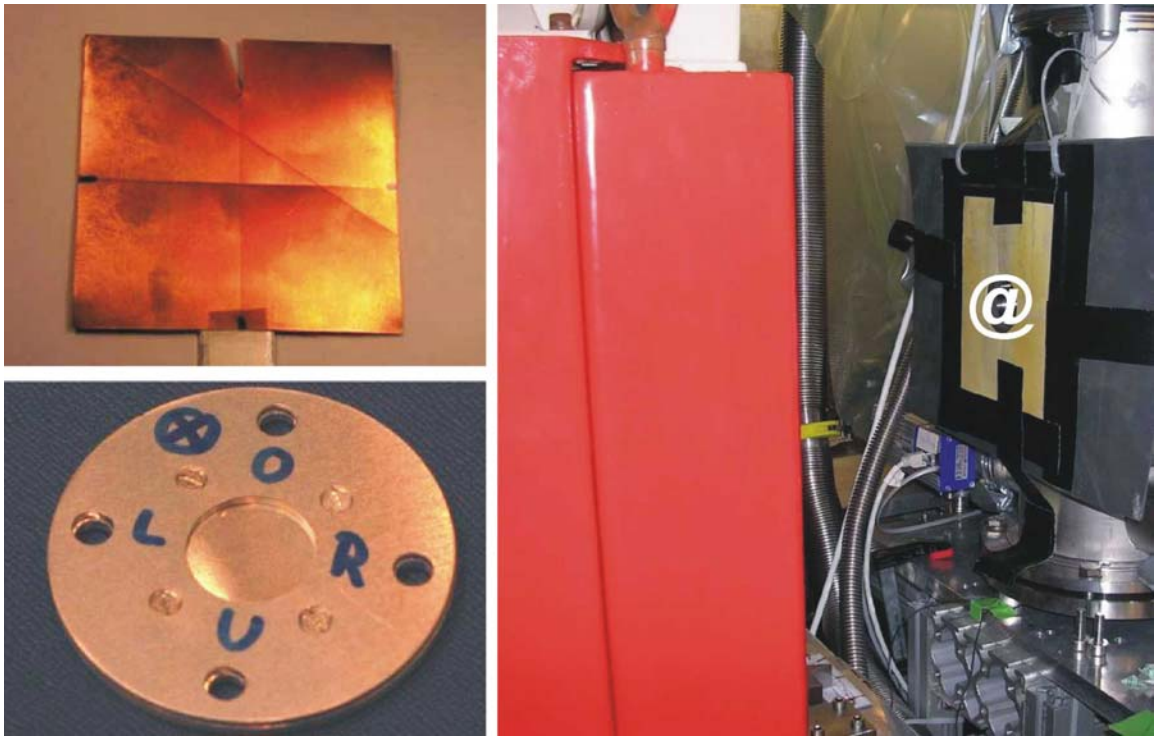

Figure B.2: Top left corner: one of the pieces of the Cu foil used for the determination of CN beam homogeneity. Thickness of the foil 0.2 mm, dimensions 61x65 mm. Bottom left corner: The Au foil holder, the blue signs indicate the orientation of the holder (L-links, R-rechts, O-oben, U-unten) and the direction of n beam). Picture on the right: @ symbol indicates the place where the Au holder and Cu foils were glued, i.e. on the beam entrance side of the cryostat after the velocity selector (red box in the left side of the picture).

where $T_{1/2} = 2.695$ d is the half life of ^{198}Au. $\int I_p dt$ is integrated proton beam current incident on the SINQ target during the time of the activation measurement. The obtained results of the CN fluxes are collected in Table B.1.

Table B.1: Results from the Au foil activation measurements. The neutron fluxes are measured in front of the target cell.

VS settings		Mean neutron energy	Neutron flux ϕ [cm^{-2} s^{-1} mA^{-1}]
tilt angle	drum speed		
-1.0	25 Hz	1.4 meV	$(1.7 \pm 0.2)\times10^6$
-1.0	35 Hz	2.9 meV	$(3.0 \pm 0.3)\times10^6$
+0.5	35 Hz	6.3 meV	$(4.4 \pm 0.4)\times10^6$
+0.5	50 Hz	13.7 meV	$(2.4 \pm 0.3)\times10^6$
+1.0	50 Hz	19.5 meV	$(1.4 \pm 0.2)\times10^6$
no selector		2.0 meV	$(4.6 \pm 0.5)\times10^7$

B.2 Count Rates in the CN Detector for an Empty Target Cell

The results from the empty cell measurements are collected in the Table B.2

B.3 Determination of Homogeneity of the Target Cell Illumination

The profiles of the CN beam at different velocity selector positions were measured with Cu foils of 61x65 mm^2 and a thickness of 0.2 mm. Natural copper consists of two isotopes ^{63}Cu (69%) and ^{65}Cu (31%). After cold neutron activation of natural copper two radioactive isotopes are produced ^{64}Cu ($t_{1/2} = 12.7$h) and ^{66}Cu ($t_{1/2} = 5.12$ min). The β activity of the long-lived isotope ^{64}Cu was measured using an imaging technique.

Table B.2: The results of the empty cell measurements. The CN neutron counts detected in the CN detector were normalised to the proton beam hitting the SINQ target (typically 1000 s with 1.2 mA onto SINQ target)

VS settings		Mean neutron energy	Neutron counts $[C^{-1}]$
tilt angle	drum speed		
-1.5	20 Hz	0.75 meV	$(4.34 \pm 0.01)\times10^4$
-1.0	25 Hz	1.4 meV	$(1.310 \pm 0.002)\times10^5$
-1.0	30 Hz	1.7 meV	$(1.776 \pm 0.003)\times10^5$
-1.0	35 Hz	2.9 meV	$(2.041 \pm 0.003)\times10^5$
-1.0	46 Hz	4.7 meV	$(2.192 \pm 0.003)\times10^5$
-0.5	50 Hz	6.9 meV	$(2.344 \pm 0.002)\times10^5$
0.0	50 Hz	9.3 meV	$(2.230 \pm 0.003)\times10^5$
no selector		2.0 meV	$(3.690 \pm 0.026)\times10^6$

The Cu foils were placed on the cryostat [1] and irradiated for 980 sec. Twelve hours after the irradiation, the samples were put on an imaging plate. The imaging plate is an image sensor which contains photo-stimulable phosphor (BaFBr:Eu) layer. The β-radiation from the decay of ^{64}Cu excite the BaFBr:Eu to a metastable state. Then the exposed imaging plate is scanned in the image scanner (see Figure B.3) using the focused red light from a He-Ne laser. The photostimulated luminescence released by laser light is collected into the photomultiplier (PMT) tube through the light collection guide. The signals from the PMT are transmitted to the computer where the image analysis is done. The raw images of the CN beam at different velocity selector settings are show in the Figure B.4 and the corresponding beam profiles (horizontal cut and the surface 2D plots) are presented in the Figures B.5 and B.6.

[1] At the same position as the gold foils.

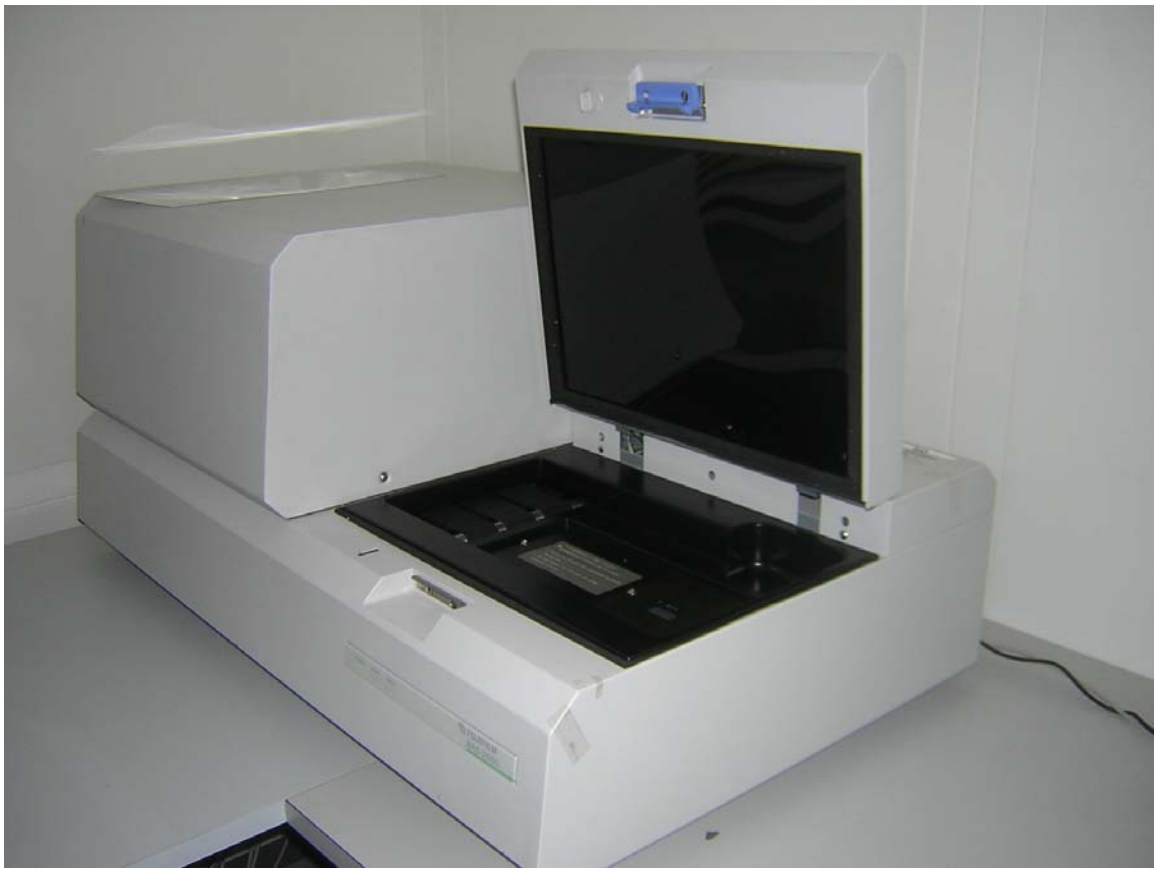

Figure B.3: The picture of the image plate scanner.

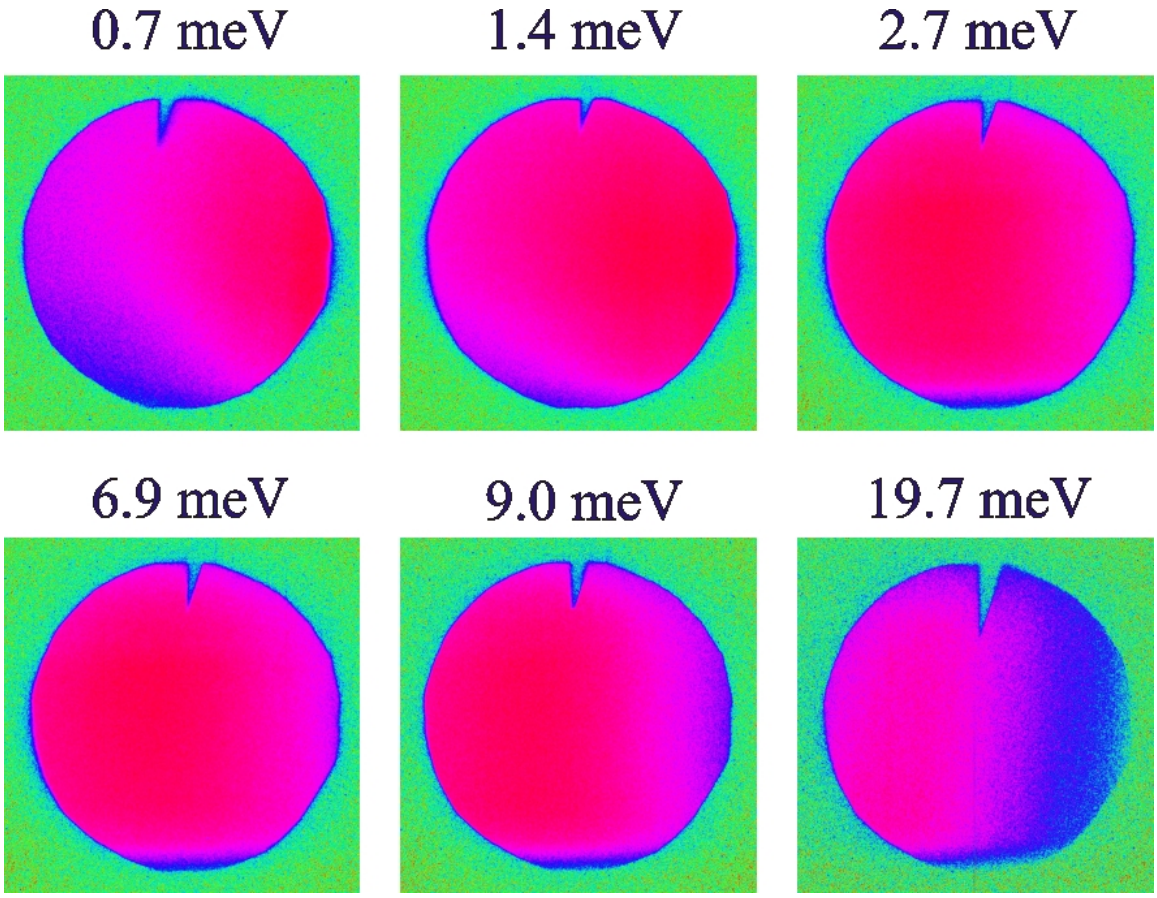

Figure B.4: The raw pictures from the imaging plate after 23 hours of exposition. The mark on each picture denotes the top of the CN beam. The values above each picture stand for the mean neutron energy.

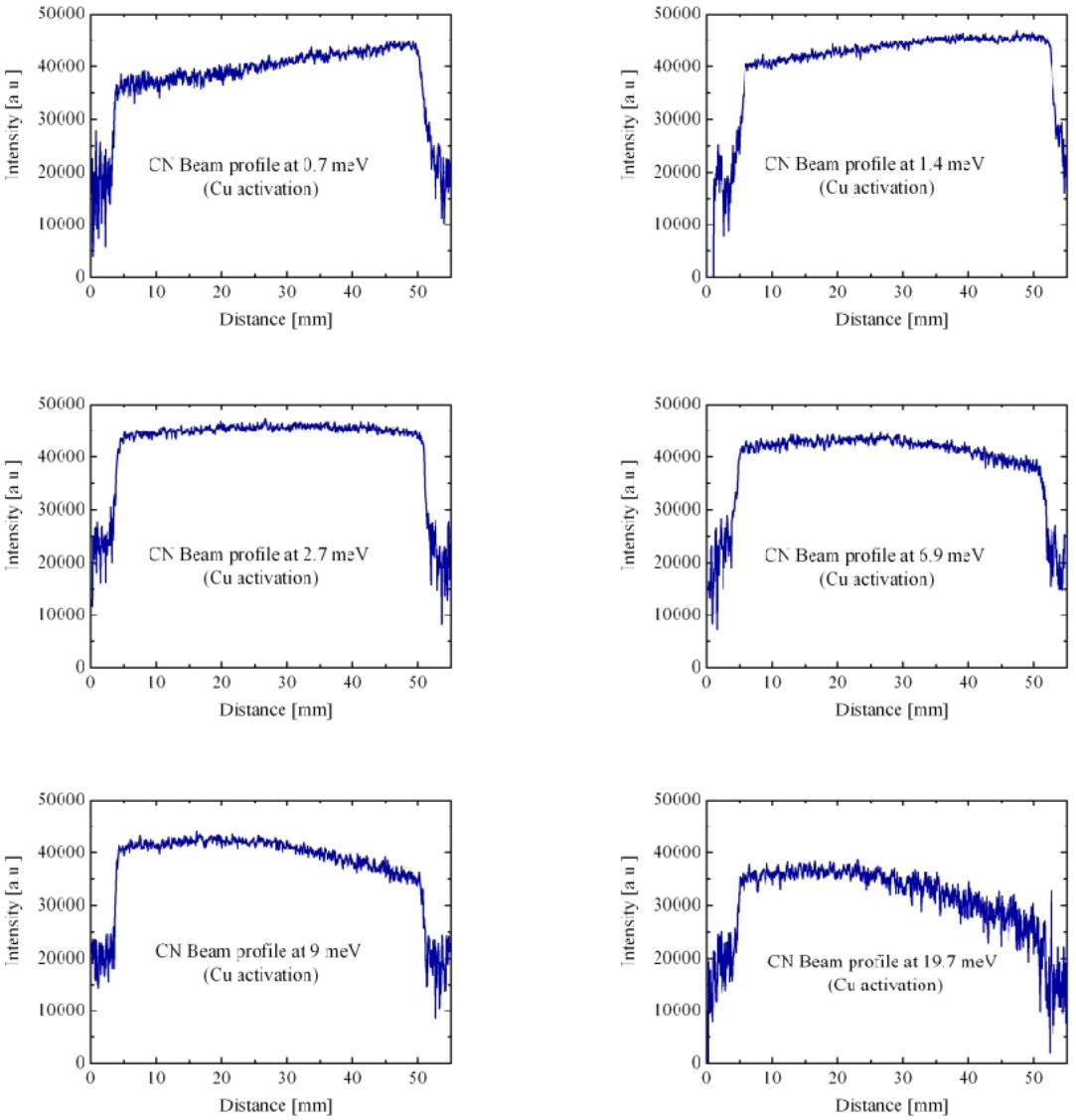

Figure B.5: The horizontal profiles of the CN beam as seen by the Cu foils.

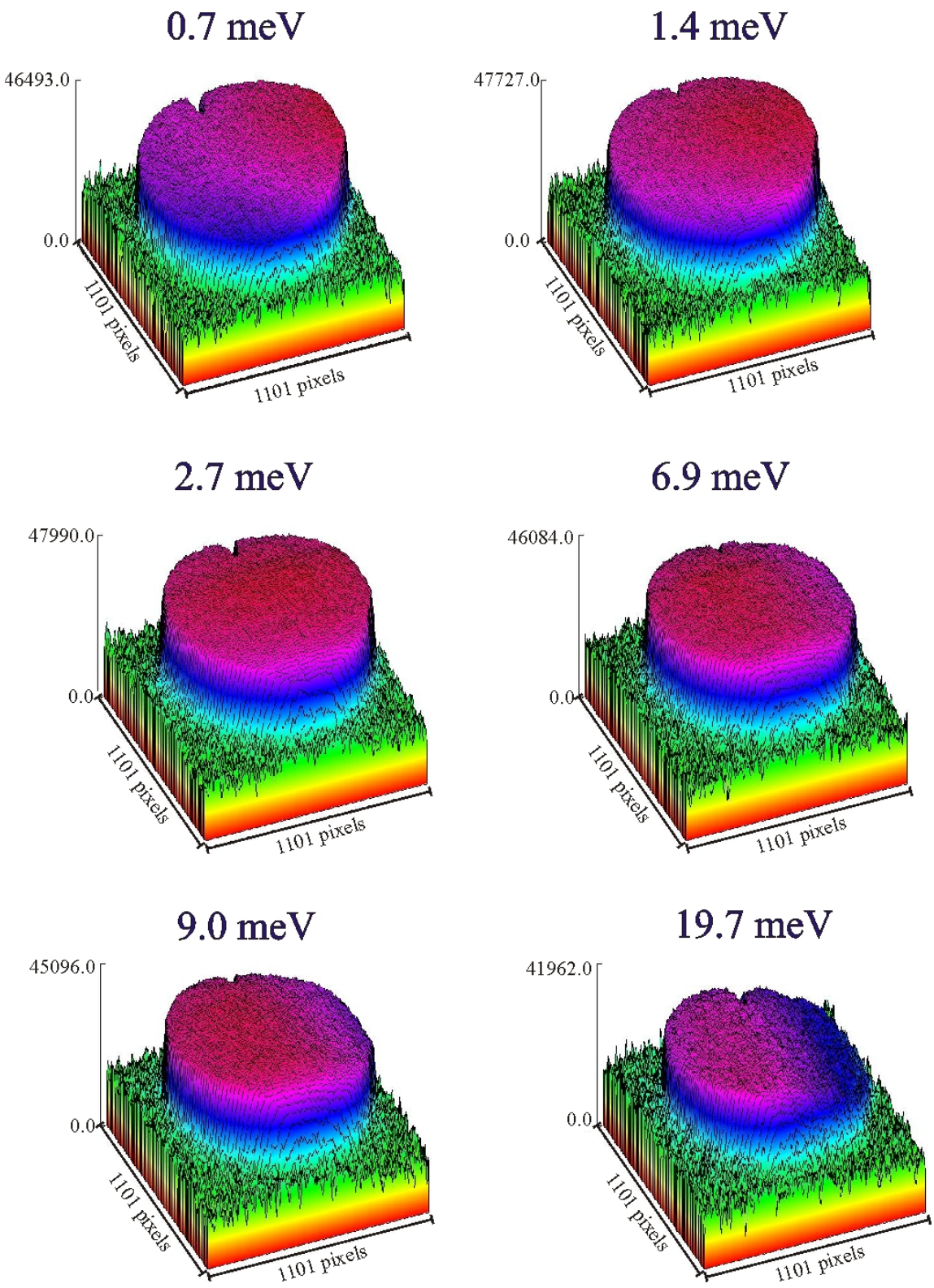

Figure B.6: The profiles of the CN beam as seen by the Cu foils (surface plot).

B.4 Detector Efficiency - Summary

The expected $1/v$ dependence for the CN detector was confirmed by comparing, for the same VS settings, gold foil activity and the empty cell count rates in the CN detector (Figure B.7). The homogeneous illumination of the target at different VS settings has been checked by performing Cu foil activation measurements.

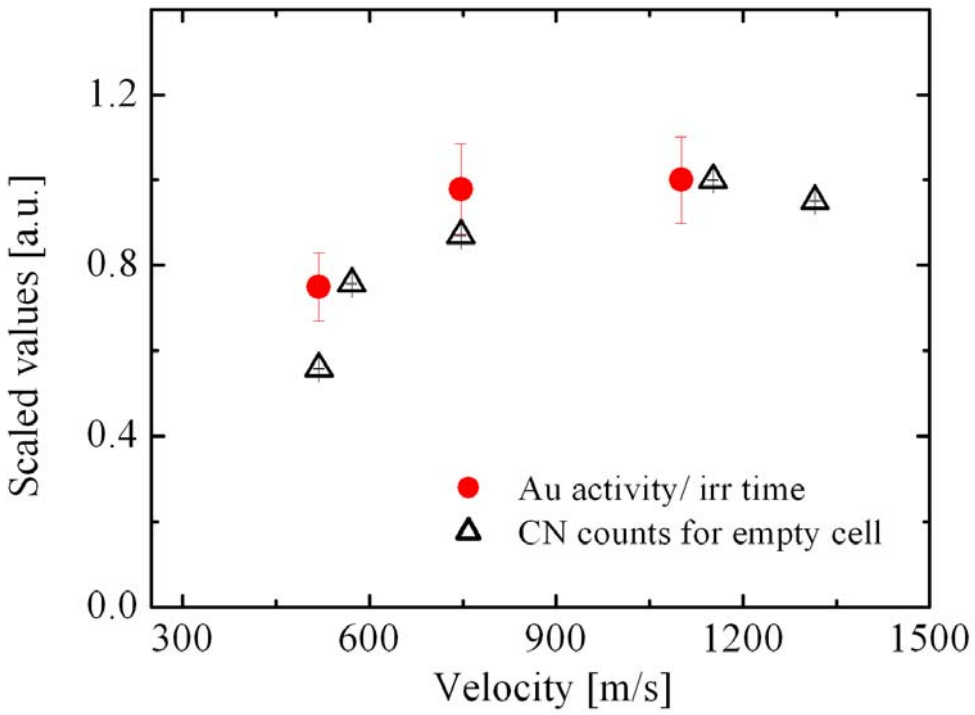

Figure B.7: Comparison between the empty cell measurements and the gold foil measurements. The scaled values versus velocity of cold neutrons. No velocity correction applied neither to the activity of the gold foil nor to the empty cell measurements. The correlation between gold foil activation and empty cell measurements is good corroborating that the empty cell measurements have the velocity dependence similar like the gold foil activity i.e. $1/v$

B.5 Systematic Effects

The main contributions to the systematic uncertainties of the experiment come from two sources:

- the bulged windows of the target cell
- instability of the beam line shutter

B.5.1 Beamline Shutter

The FUNSPIN beamline is equipped with two shutters: (i) the main beamline shutter, that separates the internal beam guide of the cold neutron source SINQ from the guide system of the FUNSPIN beam, and (ii) the failsafe shutter placed at the end of the FUNSPIN guide system. The details of the FUNSPIN beamline construction can be found in [78]. The opening and closing of the main beam shutter is controled by a stepper motor. During the experiment, we have observed that this mechanism sometimes failed, causing the shutter to stick in the wrong (open) position, thus changing the cold neutron flux by approximately 20% (see Figure B.8). The correction for this effect could be easily made by knowing the moment of entering into the FUNSPIN area.

B.5.2 Neutron Windows

In the neutron beam axis, the target cell has an entrance and an exit window 40 mm apart, each with thickness of 0.15 mm and a diameter of 40 mm. These thin reentrant windows have been machined out of rods of AlMg3, together with the flanges with which they form single pieces. During the experiments, the windows must typically withstand a pressure of 1 atm relative to the vacuum. However, most probably due to the slightly higher pressure created in the target cell during melting the solids, both the exit and the entrance neutron windows bulged, resulting in elongation of the initial neutron path in the target cell. The effect of this shape alteration is shown in Figure B.9. The estimation of the 'bulge' effect is important, especially for the determination of the CN total cross sections from the CN transmission data. This is done by measuring the depth of the deformation at different locations (in the middle and on the edges of the window). The bulge results in (1.5 $\pm$ 0.1) mm and (1.3 $\pm$ 0.1) mm elongation for the entrance window and the exit window, respectively. The elongation of the neutron path needs to be taken into account during the analysis. Since there was not a well defined moment when the windows bulged (most probably it was an continuous process, i.e. after each crystal melting some shape deformation was present) the systematics connected with the influence of the window shape on the detected CN flux is estimated to be on the level of 7%.

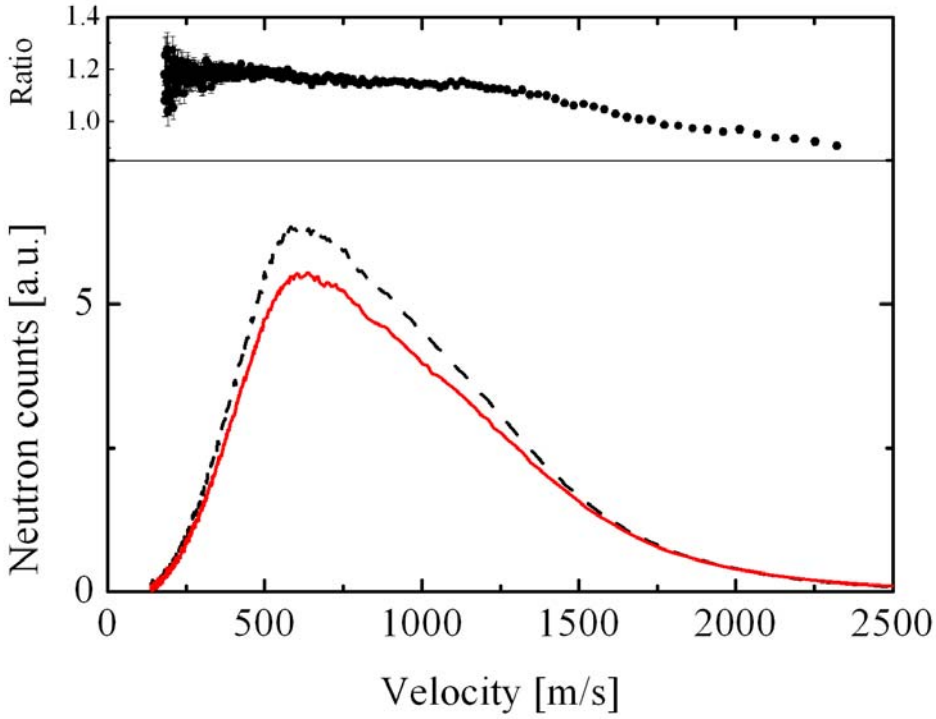

Figure B.8: The typical CN spectra (red solid line) and the CN spectra taken with the main beamline shutter in the wrong open position (black dashed line). The insert shows the ratio of the two spectra indicating that the CN velocity distribution is also slightly changed.

Figure B.9: An alteration of the shape of the neutron window by pressure. The new window is shown on the right, the deformed one on the left.

Acknowledgments

I would like to thank my thesis supervisor, Prof. Eberhard Widmann for allowing me preparing this thesis at the University of Vienna and for his assistance and support.

I would also like to thank Dr. Manfred Daum for giving me the opportunity to work in the Ultracold Neutron Group at the Paul Scherrer Institut.

I would especially like to thank Dr. Klaus Kirch for a great help during the experiments, data analysis, and for providing advice on drafts.

I would like to thank my friends from the collaboration, namely: F. Atchison, B. Blau, K. Bodek, B. van den Brandt, T. Bryś, M. Daum, P. Fierlinger, A. Frei, P. Geltenbort, P. Hautle, R. Henneck, S. Heule, A. Holley, K. Kirch, A. Knecht, J. A. Konter, M. Kuźniak, C.-Y. Liu, A. Michels, M. Meier, C. Morris, A. Pichlmaier, C. Plonka, Y. Pokotilovski, A. Saunders, Y. Shin, U. Szerrer, B. Theiler, D.Tortorella, M. Wohlmuther, A. Wokaun, A. R. Young, J. Zmeskal and G. Zsigmond, for helping with the setup construction and design, taking part in the shifts during the experiments and for all comments and suggestions.

I wish to acknowledge the support and help of K.Kohlik, W. Arrigoni, P. Schurter, M. Horisberger, K. Clausen, G. Frei, G. Kühne, E. Lehmann, T. Scherer, M. Luethy, M. Wiedemeier and A. van Loon.

I would like to thank my friends from the Stefan-Meyer-Institut: F. Boes, R. Gsell, K. Nikolics, D. Stückler for a great help with submitting the thesis.

The experimental work was performed at the FUNSPIN beamline of the Swiss Spallation Neutron Source. I am grateful to the accelerator crew and SINQ staff for providing excellent beam conditions during the experiment and to the various technical support services, whose help have made these experiments possible.

I am greatful to my family and all my friends for supporting me throughout my studies. I would especially like to thank my parents: Wieslaw and Krystyna, my grandparents: Mirosława and Stanisław and my sister Dorota for unremitting support and encouragement.

Bibliography

[1] F. Atchison *et al.*, *Measured Total Cross Section of Slow Neutrons Scattered by Solid Deuterium and Implications for Ultracold Neutron Sources*, Phys. Rev. Lett. **95**, 182502 (2005).

[2] F. Atchison *et al.*, *Production of ultracold neutrons from a cold neutron beam on a* $^2H_2$ *target* Phys. Rev. C **71**, 054601 (2005).

[3] F.Atchison *et al.*, *Investigation of solid* D_2*,* O_2 *and* CD_4 *for ultracold neutron production* to be published in NIMA.

[4] F. Atchison *et al.*, *Cold neutron energy dependent production of ultracold neutrons in solid deuterium* Phys. Rev. Lett. **99**, 262502 (2007).

[5] W. Greiner, J. Reinhardt, *Field quantization*, Spring-Verlag Berlin Heidelberg 1996.

[6] S. Weinberg, *The quantum theory of fields*, Cambridge University Press, 1995.

[7] E. Noether, *Invariante Variationsprobleme* Nach. v. d. Ges. d. Wiss. zu Gottingen 235 (1918).

[8] T. D. Lee and C. N. Yang, *Question of Parity Conservation in Weak Interactions* Phys. Rev. **104**, 254 (1956).

[9] C. S. Wu *et al.*, *Experimental Test of Parity Conservation in Beta Decay* Phys. Rev. 105, 1413 (1957).

[10] G. Lüders, *Proof of the TCP theorem*, Ann. Phys. (N. Y.) **2**, 1 (1957).

[11] W. Pauli, Nuovo Cimento **6**, 204 (1957).

[12] M. Beyer (Ed.), *CP Violation in Particle, Nuclear and Astrophysics* Springer-Verlag 2002.

[13] A. Riotto and M. Trodden, *Recent Progress in Baryogenesis*, Ann. Rev. Nucl. Part. Sci. **49**, 35 (1999).

[14] arXiv:astro-ph/0603451v2

[15] R. D. Peccei, *Matter-Antimatter Asymmetry in the Universe and an Arrow for Time*, arXiv:hep-ph 0608226v1

[16] A. D. Sakharov, Pisma Zh. Eksp. Teor. Fiz. **5**, 32 (1967).

[17] J. H. Christenson, J. W. Cronin, V. L. Fitch, R. Turlay, *Evidence for the 2π Decay of the K_2^0 Meson*, Phys. Rev. Lett. **13**, 138 (1964).

[18] BABAR Collaboration, *Observation of CP Violation in the B^0 Meson System* Phys. Rev. Lett. **87**, 091801 (2001).

[19] BELLE Collaboration, *Observation of Large CP Violation in the Neutral B Meson System* Phys. Rev. Lett. **87**, 091802 (2001).

[20] P. B. Schwinberg, R. S. Van Dyck, Jr. and H. G. Dehmelt, *Trapping and thermalization of positrons for geonium spectroscopy* Phys. Lett. A **81**, 119 (1981).

[21] G. Gabrielse *et al.*, *Precision Mass Spectroscopy of the Antiproton an Proton Using Simultaneously Trapped Particles*, Phys. Rev. Lett. **82**, 3198 (1999).

[22] R. Bluhm, V. A. Kostelecký, C. D. Lane, *CPT and Lorentz Tests with Muons*, Phys. Rev. Lett. **84**, 1098 (2000).

[23] R. Bluhm, V. A. Kostelecký, N. Russell, *CPT and Lorentz Tests in Hydrogen and Antihydrogen* Phys. Rev. Lett. **82**, 2254 (1999).

[24] E. Widmann, *Testing CPT with antiprotonic helium and antihydrogen - the ASACUSA experiment at CERN-AD*, Nucl. Phys. A **752**, 87c (2005).

[25] CPLEAR Collaboration, *First direct observation of time-reversal non-invariance in the neutral-kaon system* Phys. Lett. B **444**, 43 (1998).

[26] L. Wolfenstein, *Violation of Time Reversal Invariance in K^0 Decays*, Phys. Rev. Lett. **83**, 911 (1999).

[27] I. I. Bigi, A. I. Sanda, *On limitations of T invariance in K decays*, Phys. Lett. B **466**, 33 (1999).

[28] H.-J. Gerber, *Evidence for time-reversal violation*, Eur. Phys. J. C **35** 195 (2004).

[29] J. Ellis, *Theory of the neutron electric dipole moment*, Nucl. Instr. Meth. **A284**, 33 (1989).

[30] C. A. Baker *et al.*, *Improved Experimental Limit on the Electric Dipole Moment of the Neutron* Phys. Rev. Lett. **97**, 131801 (2006).

[31] X. G. He, B. H. J. McKellar, S. Pakvasa, *The neutron electric dipole moment* Int. J. Mod. Phys. **4**, 5011 (1990).

[32] P. G. Harris *et al.*, *New Experimental Limit on the Electric Dipole Moment of the Neutron*, Phys. Rev. Lett. **82**, 904 (1999).

[33] R. Golub, D. Richardson, S.K. Lamoreaux, *Ultra-Cold Neutrons*, Adam Hilger, Bristol, 1991.

[34] E. M. Purcell, N. F. Ramsey, *On the Possibility of Electric Dipole Moments for Elementary Particles and Nuclei*, Phys. Rev. **78**, 807 (1950).

[35] J. H. Smith, E. M. Purcell, N. F. Ramsey, *Experimental Limit to the Electric Dipole Moment of the Neutron* Phys. Rev. **108**, 120 (1957).

[36] W.-M. Yao *et al.* (Particle Data Group), J. Phy. G **33** 1 (2006).

[37] G. Ban *et al.*, *A direct experimental limit on neutron - mirror neutron oscillations* Phys. Rev. Lett. **99**, 161603 (2007).

[38] V. V. Nesvizhevsky *et al.*, Nature **415**, 297 (2002).

[39] V. V. Nesvizhevsky *et al.*, Phys. Rev. D **67**, 102002 (2003).

[40] http://whisky.ill.fr/YellowBook/

[41] A. Frei *et al.*, *First production of ultracold neutrons with a solid deuterium source at the pulsed reactor TRIGA Mainz*, Eur. Phys. J. A **34**, 119 (2007).

[42] R. Golub and J.M. Pendlenbury, *Super-thermal sources of ultra-cold neutrons*, Phys. Lett. **53A**, 133 (1975).

[43] M. Wohlmuther and G. Heidenreich, *The spallation target of the ultra-cold neutron source UCN at PSI* Nucl. Instr. Meth. **A564**, 51 (2006).

[44] D. Anicic *et al.*, *A fast kicker magnet for the PSI 600 MeV proton beam to the PSI ultracold neutron source*, Nucl. Instr. Meth. **A541**, 598 (2005).

[45] C. L. Morris *et al.*, *Measurements of Ultracold-Neutron Lifetimes in Solid Deuterium*, Phys. Rev. Lett. **89**, 272501 (2002).

[46] F.Atchison *et al.*, *Ortho-para equilibrium in a liquid D_2 neutron moderator under irradiation*, Phys. Rev. B **68**, 094114 (2003).

[47] K.Mishima *et al.*, *Time-differential observation of the ortho-para conversion of liquid D_2 under irradiation*, Phys. Rev. B **75**, 014112 (2007).

[48] G. W. Collins *et al.*, Phys. Rev. B **44**, 6598 (1991).

[49] The PSI UCN Source, contibuted paper to ICANS2007.

[50] K. H. Beckurts, K. Wirtz, *Neutron Physics*, Springer - Verlag 1964.

[51] R. Golub and J.M. Pendlebury, *The interaction of Ultra-Cold Neutrons (UCN) with liquid helium and a supherthermal UCN source* Phys. Lett. **62A**, 337 (1977).

[52] P. Ageron *et al.*, *Measurement of the ultra cold neutron production rate in an external liquid helium source* Phys. Lett. **66A**, 469 (1978).

[53] H. Yoshiki *et al.*, *Observation of Ultracold-Neutron Production by 9A Cold Neutrons in Superfluid Helium.* Phys. Rev. Lett. **68**, 1323 (1992).

[54] Y. Abe and N. Morishima, *Ultracold and cold neutron cross-sections of liquid helium at low temperatures down to 0.1 K*, Nucl. Instr. Meth. **A459**, 256 (2001).

[55] E. Korobkina *et al.*, *Production of UCN by downscattering in superfluid* He^4, Phys. Lett. **301A**, 462 (2002).

[56] W. Schott *et al.*, *UCN production in superfluid helium*, Eur. Phys. J. A 16, 599-601 (2003).

[57] O. Zimmer *et al.*, *Superfluid-Helium Converter for Accumulation and Extraction of Ultracold Neutrons*, Phys. Rev. Lett. **99**, 104801 (2007).

[58] I. S. Altarev et al., *A liquid hydrogen source for ultracold neutrons* Phys. Lett. **80A**, 413 (1980).

[59] R. Golub and K. Böning, *New Type of Low Temperature Source of Ultra-Cold Neutrons and Production of Continous Beams of UCN*, Z. Phys. **B51**, 95 (1983).

[60] Z.-Ch. Yu, S. S. Malik, R. Golub, *A thin film source of Ultra-Cold Neutrons*, Z. Phys. **B62**, 137 (1986).

[61] A. P. Serebrov *et al.*, *Is it possible to produce next generation of UCN sources with density* 10^3 - 10^4 cm^{-3} *?*, JETP Lett. **59**, 757 (1994).

[62] A. P. Serebrov *et al.*, *Experimental study of a solid deuterium source of ultracold neutrons* JETP Lett. **62**, 785 (1995).

[63] Y. Pokotilovski, *Production and storage of ultracold neutrons at pulse neutron sources with low repetition rates*, Nucl. Instr. Meth. **A356**, 412 (1995).

[64] A. P. Serebrov *et al.*, *Solid deuterium source of ultracold neutrons based on a pulsed spallation source*, JETP Lett. **66**, 802 (1997).

[65] A. P. Serebrov *et. al. Solid deuterium and UCN factory: application to the neutron electric dipole moment measurement*, Nucl. Instr. Meth. **A440**, 658 (2000).

[66] A. Saunders *et al.*, *Demonstration of a solid deuterium source of ultra-cold neutrons*, Phys. Lett. B **593**, 55 (2004).

[67] Y.Pokotilovski, *ESS Special Expert Meeting - UCN Factory Workshop*, Febr. 22-23, 2002, Wien, http://www.ati.ac.at/ neutrweb/ess/ess.html

[68] W. G. Stirling, W. Press, H. H. Stiller J.Phys.C. **10** (1977).

[69] C.-Y. Liu, *A Superthermal Ultra-Cold Neutron Source*, Dissertation, Princeton University, 2002.

[70] C.-Y. Liu, *Physics of superthermal UCN production in SD_2 and other materials*, Proceedings of the 3rd UCN Workshop, Pushkin, 2001. http://nrd.pnpi.spb.ru/SEREBROV/3rd/talks/20/chen.pdf

[71] C.-Y. Liu and A. R. Young, *Ultra-cold Neutron Production in Anti-ferromagnetic Oxygen Solid*, nucl-th/0406004.

[72] I. Heilmann, J. Kjems, *Mechanical Velocity Selector, Neutron Flux and Q-Range for the small Angle Neutron Scattering Facility at Risø* Risø- M - 2208, RisøNational Laboratory, Denmark, February 1980.

[73] K. N. Clausen, *Velocity selector for Rita* Internal report, June 1995.

[74] K. Bodek *et al.*, *An apparatus for the investigation of solid D_2 with respect to ultra-cold neutron sources*, Nucl. Instr. Meth. **A533**, 491 (2004).

[75] J. Van Krankendonk, *Solid Hydrogen*, Plenum, New York, 1983.

[76] F. Atchison *et al.*, *Measurement of the Fermi potential of diamond-like carbon and other materials* Nucl. Instr. Meth. **B260**, 647 (2007).

[77] http://kur.web.psi.ch/amor/

[78] J. Zejma *et al.*, *FUNSPIN polarized cold-neutron beam at PSI* Nucl. Instr. Meth. **A539**, 622-639 (2005).

[79] M. Kasprzak, Diploma thesis, Jagiellonian University, Krakow, 2004, nucl-ex/0407022.

[80] T. Bryś, Dissertation, ETH Zürich, 2007.

[81] A. C. Zemach, R. J. Glauber, *Dynamics of Neutron Scattering by Molecules*, Phys. Rev. **101**, 118 (1956).

[82] W. Demtröder, *Atoms, Molecules and Photons*, Springer-Verlag Berlin Heidelberg 2006.

[83] R. G. Johnson and C. D. Bowman, *Inelastic-Scattering Measurements of 1.5-15 eV Neutrons*, Phys. Rev. Lett. **49**, 797 (1982).

[84] H. Haken, H. C. Wolf, *Molecular Physics and Elements of Quantum Chemistry*, Springer-Verlag Berlin Heidelberg 2004.

[85] M. Fierz, *Uber die relativistiche Theorie krafterfreier Teilchen mit Beliebigem Spin* Helv. Phys. Acta **12**, 3 (1939).

[86] W. Pauli, *The Connection Between Spin and Statistics*, Phys. Rev. **58**, 716 (1940).

[87] J. Schwinger and E.Teller, *Scattering of Neutrons by Ortho and Parahydrogen*, Phys. Rev. **52**, 286 (1937).

[88] E. Fermi, *On the motion of neutrons in hydrogenous substances*, Riccerca Scientifica, **7**, 13 (1936). (english translation in E. Fermi, *Collected papers, Vol. I, Italy 1921-1938*, Chicago, University Press , (1962).

[89] M. Hamermesh and J. Schwinger, Phys. Rev. **55**, 671 (1939), see p. 679.

[90] M. Hamermesh and J. Schwinger, *The Scattering of Slow Neutrons by Ortho- and Paradeuterium*, Phys. Rev. **69**, 145 (1946).

[91] A. Young and J. U. Koppel, *Slow Neutron Scattering by Molecular Hydrogen and Deuterium*, Phys. Rev. **135**, A603 (1964).

[92] J. U. Koppel, J. A. Young, *Slow Neutron Spectra in Molecular Hydrogen at Low Temperatures*, Nukleonik **8**, 40 (1966).

[93] G. H. Vineyard, *Scattering of Slow Neutrons by Liquid*, Phys. Rev. **110**, 999 (1958).

[94] L. Van Hove, *Correlations in Space and Time and Born Approximation Scattering in Systems of Interacting Particles*, Phys. Rev. **95**, 249 (1954).

[95] F. Atchison *et al.*, *Measured Total Cross Section of Slow Neutrons Scattered by Gaseous and Liquid* $^2H_2$, Phys. Rev. Lett. **94**, 212502 (2005).

[96] J. Kohlbrecher and W. Wagner, J. Appl. Crystallogr. **33**, 804 (200).

[97] A. Steyerl *et al*, Phys. Lett. A **116**, 347 (1986).

[98] Ch. Kittel, *Introduction to solid state physics*, John Wiley & Sons, New York, 1963.

[99] M. Nielsen, H. Bjerrum Møller, *Lattice Dynamics of Solid Deuterium by Inelastic Neutron Scattering*, Phys. Rev. **B3**, 4383, 1971.

[100] V. G. Manzhelii, A. I. Prokhvatilov, V. G. Gavrilko, A. P. Isakina, *Structure and thermodynamic properties of cryocrystals*, Begell House Inc. Publishers, New York, 1999.

[101] F. Atchison, *Notes on UCN production* Internal UCN Report, 2005.

[102] M. Zoppi *et al*, *Neutron-diffraction determination of the microscopic structure of liquid deuterium*, Phys. Rev. E **48**, 1000 (1993).

[103] J. R. Granada, V. H. Gillette, *A new thermal neutron scattering kernel for liquid hydrogen*, Physica B **348**, 6 (2004).

[104] F. Atchison *et al.*, *Investigation of* CD_4 *with Raman spectroscopy and UCN* PSI Annual Report 2004.

[105] E. Gregoryanz, M. J. Clouter, Phys. Rev. B **58**, 11933 (1998).

[106] S. W. Lovesey, *Theory of neutron scattering from condensed matter*, Clarendon press, Oxford, 1984, Vol I.

[107] G. Sarma, *Scattering of slow neutrons by liquid hydrogen*, in *Inelastic Scattering of Neutrons in Solids and Liquids*, IAEA, Vienna, 397 (1961).

[108] M.Nielsen, *Phonons in Solid Hydrogen and Deuterium Studied by Inelastic Coherent Neutron Scattering*, Phys. Rev. **B7**, 1626, 1973.

[109] I.F. Silvera, *Solid molecular hydrogens in the condensed phase*, Rev. Mod. Phys. **52**, No. 2, Part I, 393-452 (1980).

[110] C.-Y. Liu, A.R. Young, S.K. Lamoreaux, *UCN upscattering rates in a molecular deuterium crystal*, Phys. Rev. **B62**, R3581 (2000).

[111] W. D. Seiffert, PhD thesis, Technischen Hochschule München, 1970.

[112] F. Atchison *et al.*, *The simulation of ultracold neutron experiments using GEANT4*, Nucl. Instr. Meth. **A552**, 513 (2005).

[113] K. G. McLennan and E. MacA. Gray, Meas. Sci. Technol. **15**, 211 (2004).

[114] L. S. Walters *et al.*, *MCNPX User's Manual Version 2.4.0*, LA-CP-02-408, 2002.

[115] W. Bernnat, J. Keinert and M. Mattes in *Proceedings of the 6th International Workshop on Advanced Cold Moderators*, Forschungszentrum Jülich Matter and Materials 20, edited by H. Conrad and Jülich 2004, p.9.

[116] P.C. Souers, *Hydrogen Properties for Fusion Energy*, University of California, Berkeley, 1986.

[117] V. F. Turchin, *Slow neutrons*, Israel Program for Scientific Translation, 1965.

[118] International Workshop on Particle Physics with Slow Neutrons, Institut Laue Langevin, Grenoble, France, 2008.

[119] E. Gutsmiedl *et al.*, *Understanding UCN production in solid D2. The generalized density of state measured in inelastic neutron scattering.* talk at the International Workshop on Particle Physics with Slow Neutrons, Grenoble, France, 2008.

[120] F. Atchison *et al.*, *Polarized UCN produced from polarized cold neutrons on solid* D_2 PSI Annual Report 2004.

[121] T. Bryś *et al.*, *Neutron reflectivity measurements on DLC foils at AMOR* PSI Annual Report 2004.